

Alma Mater Studiorum – Università di Bologna

DOTTORATO DI RICERCA IN

CHIMICA

Ciclo XXX

Settore Concorsuale: 03/B1

Settore Scientifico Disciplinare: CHIM/03

CRYSTAL ENGINEERING OF MOLECULAR MATERIALS: DESIGN,
SYNTHESIS AND SOLID-STATE INVESTIGATION OF PHOTOREACTIVE
AND THERMO/PHOTOCHROMIC SOLIDS.

Presentata da: Floriana Spinelli

Coordinatore Dottorato

Prof. Aldo Roda

Supervisore

Prof.ssa Fabrizia Grepioni

Co-supervisore

Dott.ssa Barbara Ventura

Esame finale anno 2018

INDEX

ABSTRACTS	pag. I
INTRODUCTION	pag. 1
CHAPTER I: PHOTOREACTIONS IN THE SOLID STATE	
I.1 Introduction	pag. 5
I.1.1 [2+2] PHOTOREACTIONS	pag. 7
I.1.2 Results and discussion	pag. 8
I.1.2.1 Structures of the salts	pag. 8
I.1.2.2 Evaluation of the possible photoreactivity by geometrical parameters	pag. 12
I.1.2.3 UV irradiation	pag. 13
I.1.2.4 Single crystal to single crystal photoreactions	pag. 14
I.1.2.5 Powder X-ray diffraction	pag. 20
I.1.3 Conclusions	pag. 24
I.1.4 Experimental section	pag. 24
I.2.1 [4+4] PHOTOREACTIONS	pag. 28
I.2.2 Results and discussion	pag. 29
I.2.2.1 Crystal structures	pag. 29
I.2.2.2 UV irradiation	pag. 31
I.2.2.3 Raman spectroscopy	pag. 37
I.2.3 Conclusions	pag. 41
I.2.4 Experimental section	pag. 42
I.3 References	pag. 44
CHAPTER II: THERMO- AND PHOTOCHROMISM IN ORGANIC CRYSTALS	
II.1 Introduction	pag. 48
II.2 Investigation of co-crystallisation effects on thermo- and photochromism in the solid state	pag. 50
II.3 Results and discussion	pag. 52
II.3.1 Crystal structures	pag. 53
II.3.2 Solid state NMR spectroscopy	pag. 59
II.3.3 Thermochromic behaviour	pag. 62

II.3.4	Photochromic behaviour	pag. 67
II.3.5	FT-IR spectroscopy	pag. 70
II.4	Conclusions	pag. 71
II.5	Experimental section	pag. 72
II.6	References	pag. 76
	Appendix A	pag. 81
	Appendix B	pag. 96

ABSTRACTS

This project was focused on the design, by means of crystal engineering, of organic molecular solids and on their interactions with light.

My research project can be divided into two main themes:

- i) [2+2] and [4+4] photoreactions in the solid state;
- ii) Thermo- and photochromic phenomena in salicylidene aniline crystals.

A knowledge of how molecules are located in the crystal packing is essential to understand the structure-properties relationships. My investigation was focused on how is possible to tune some properties in crystalline materials by making changes in the crystal packing. I then looked at the relationship between the crystal packing and the effect of the stimulation by light. In both points (i) and (ii) a suitable alignment of molecules in the crystal packing was required. In order to favour photoreactions in the solid-state, it was essential for adjacent double bonds to be parallel and with a distance of maximum 4.2 Å. In order for thermo- and photochromism in crystals of salicylidene anilines to occur, the main conditions required were “close” and “open” packings, respectively.

Crystal packing modifications have been achieved by the use of co-crystallization, salts formation and formation of coordination compounds, both in solution and via mechanochemical methods. Different crystallization methods were used, e.g. liquid diffusion, solvent evaporation, vapour diffusion, crystallization from melt, crystal grow from gel. In some cases, no single crystals have been obtained, thus some compounds have been structurally characterized using powder diffraction data.

The solid-state characterization of all the compounds was performed by means of the following techniques: Single Crystal X-Ray Diffraction (SCXRD); Powder X-Ray Diffraction (PXRD); Thermogravimetric Analysis (TGA) and Differential Scanning Calorimetry (DSC); Infrared (FT-IR and ATR-FTIR) spectroscopy; Solid state absorption and emission spectroscopy (at ISOF-CNR); Scanning Electron Microscopy (SEM) and Raman spectroscopy (in collaboration with UniBO), and NMR spectroscopy (in collaboration with UniTO).

Il seguente progetto è incentrato sulla progettazione di solidi molecolari organici mediante l'utilizzo dell'ingegneria cristallina.

Il mio progetto di ricerca è diviso in due temi principali:

- i) Fotoreazioni [2+2] e [4+4] allo stato solido;
- ii) Fenomeni termocromici e fotocromici in cristalli di 2-[(E)-(fenilimmino)metil]fenolo.

La conoscenza di come le molecole sono localizzate nell'impaccamento cristallino è essenziale per comprendere la relazione tra la loro struttura e le proprietà. Il mio lavoro è stato focalizzato su come modificare alcune proprietà dei materiali cristallini apportando variazioni nell'impaccamento del cristallo.

Ho investigato sulla relazione tra impaccamento cristallino e l'effetto della stimolazione mediante la luce. In entrambi i punti (i) e (ii), è richiesto un adeguato allineamento delle molecole nella loro struttura cristallina. Per favorire le fotoreazioni allo stato solido, è necessario che i doppi legami adiacenti siano paralleli e con una distanza massima di 4,2 Å. Invece, per l'ottenimento di cristalli termocromici e fotocromici, le condizioni principali richieste sono impaccamenti cristallini "chiusi" e "aperti", rispettivamente.

Le modifiche dell'impaccamento cristallino sono state effettuate mediante co-cristallizzazione, formazione di sali e formazione di composti di coordinazione, sia in soluzione che per via meccanochimica.

Sono stati utilizzati diversi metodi di cristallizzazione: diffusione di liquida, evaporazione di solvente, diffusione di vapore, cristallizzazione da fusione, crescita cristallina da gel. In alcuni casi non sono stati ottenuti cristalli e i composti sono stati caratterizzati strutturalmente mediante diffrazione da polveri.

Per la caratterizzazione dei composti allo stato solido, sono state utilizzate le seguenti tecniche: Diffrazione RX da Cristallo Singolo (SCXRD), Diffrazione RX da polveri (PXRD); Analisi Termogravimetrica (TGA) e Calorimetria Differenziale a Scansione (DSC); spettroscopia Infrarossa (FT-IR e ATR-FTIR); spettroscopia di assorbimento ed emissione allo stato solido (presso ISOF-CNR); microscopia elettronica a scansione (SEM) e spettroscopia Raman (in collaborazione con UniBO) e spettroscopia NMR (in collaborazione con UniBO e UniTO).

INTRODUCTION

*“Scientists have always dreamt of being able to obtain materials with desired properties starting from a knowledge of the properties of the molecular/ionic components of choice and of their spatial distribution and intermolecular interactions in the solid. Crystal engineering is essentially making crystals with a purpose”.*¹

Crystal engineering - the design, construction and exploitation of functional, molecular crystalline materials - has become the new frontier of solid state chemistry. Crystal engineering makes use of self-recognition and self-assembly processes in order to generate crystalline materials, with properties resulting from the convolution of the molecular building block properties with intermolecular bonding and crystal periodicity.² Born in the field of organic solid state chemistry, crystal engineering arose to the level of world-wide-spread field of research in the late eighties, following the success of supramolecular chemistry.³ During the same years coordination chemistry also experienced a similar evolution, and the focus of research shifted from the synthesis and characterisation of “zero dimensional” molecular complexes to that of three-dimensional networks, with properties depending on the nature of the ligands and on the coordination geometry, electronic, spin and charge state of the metal centres.⁴ The confluence of these two fields of research - periodical coordination chemistry via coordination bonds and supramolecular self-assembly via directional intermolecular interactions- generated a new interdisciplinary area of chemistry, where traditional barriers between organic, organometallic, and inorganic chemistry were no longer meaningful. As pointed out by Desiraju, crystal engineering brought about a novel multidisciplinary view of crystal chemistry.⁵

Hydrogen and halogen bonding, electrostatic interactions, ligand-metal coordination bonds - exploited in crystal engineering exercises - are amply discussed in this thesis. Making crystals by “using” these interactions to construct crystal structures with desired structure-function relationships is the ultimate goal of crystal engineering.

Hydrogen bonding, aromatic interactions, dipole-dipole interactions, halogen bonding, Coulombic interactions between ions and interactions with delocalised electron systems have all been employed and analysed, and their effects evaluated. A special attention has been dedicated in this thesis to the use of these interactions in the preparation of co-crystals.

Co-crystals are undoubtedly at the forefront of crystal engineering research, and represent an important advancement on the path towards design of materials. The interest in co-crystals stems from their potential uses in the food and pharma areas, and in general in those fields related to the synthesis and processing of molecular materials (therefore also pigments, energetic materials, agrochemicals, organic semiconductors). Indeed, co-crystals may open new ways to design or to alter the properties of solid active pharmaceutical ingredients, including thermal stability, shelf life, solubility, dissolution rate, compressibility, *etc.* In general terms, co-crystals show differences in physico-chemical properties with respect to the parent single molecule crystal that are usually larger than those between polymorphs and often also than those between the pure crystalline solid and its solvates. It is by a judicious choice of synthons, functional groups, polarity, *etc.* that the construction of novel aggregates can be attempted.

Co-crystals are formed by two or more components that possess a chemical identity on their own and that form stable aggregates at room temperature. A critical aspect for a successful co-crystallisation strategy is the choice of a suitable co-former; the molecule of interest and the selected co-former interact *via* non covalent bonds. The most effective interactions are usually the hydrogen bond (HB)⁶ and the halogen bond (XB).⁷

The topic of co-crystals has been recently addressed by a number of authors. A book by Wouters and Quéré is dedicated to pharmaceutical co-crystals,⁸ and updates have recently been published.⁹ Furthermore, the occurrence of polymorphism for multicomponent systems, including co-crystals, has been reviewed recently.¹⁰

Co-crystallization has recently been used also in materials science for the enhancement of optical properties, luminescence, conduction, and so on.¹¹ Co-crystals are usually characterised by different crystal structures compared to the pure components, and as a result often exhibit widely different physical properties. The use of co-crystals as a means to modify optical properties such as fluorescence¹² and phosphorescence¹³ of luminescent molecules is a strategy already showing very promising results.¹⁴

References:

1. D. Braga, F. Grepioni, L. Maini, S. d'Agostino, *IUCrJ*, **2017**, 4, 369–379.
2. (a) G. R. Desiraju, *Crystal Engineering: The Design of Organic Solids*, Elsevier, Amsterdam, **1989**. This book remains, to date, the only single author book

- on the subject; (b) D. Braga, F. Grepioni and A. G. Orpen, *Crystal Engineering: from Molecules and Crystals to Materials*, Kluwer Academic Publishers, Dordrecht, **1999**.
- (a) J. M. Lehn, *Angew. Chem., Int. Ed. Engl.*, **1990**, 29, 1304; (b) *Supramolecular Chemistry: Concepts and Perspectives*, ed. J. M. Lehn, VCH, Weinheim, **1995**.
 - (a) P. J. Stang, B. Olenyuk, *Acc. Chem. Res.*, **1997**, 30, 502–518; (b) B. F. Hoskins, R. Robson., *J. Am. Chem. Soc.*, **1990**, 112, 1546–1554; (c) B. Moulton, M. J. Zaworotko, *Chem. Rev.*, **2001**, 101, 1629–1658; (d) M. Fujita, *Chem. Soc. Rev.*, 1998, 27, 417–425; (e) Owen R. Evans, Wenbin Lin, *Acc. Chem. Res.*, **2002**, 35, 511–522; (f) M. Oh, Gene B. Carpenter, D. A. Sweigart, *Acc. Chem. Res.*, **2004**, 37, 1–11; (g) L. Carlucci, G. Ciani, D. M. Proserpio, *CrystEngComm*, **2003**, 5, 269–279; (h) C. Janiak, *Dalton Trans.*, **2003**, 2781–2804; (i) R. Robson, *J. Chem. Soc., Dalton Trans.*, **2000**, 3735–3744; (l) G. S. Papaefstathiou, L. R. MacGillivray, *Coord. Chem. Rev.*, **2003**, 246, 169.
 - G. R. Desiraju, *Angew. Chem., Int. Ed.*, **2007**, 46, 8342–8356.
 - (a) D. Braga, F. Grepioni, *Acc. Chem. Res.*, **2000**, 33, 601–608; (b) M. S. Yuan, D.-E. Wang, P. Xue, W. Wang, J. C. Wang, Q. Tu, Z. Liu, Y. Liu, Y. Zhang and J. Wang, *Chem. Mater.*, **2014**, 26, 2467–2477.
 - (a) P. Metrangolo, J. S. Murray, T. Pilati, P. Politzer, G. Resnati, G. Terraneo, *Cryst. Growth Des.*, **2011**, 11, 4238–4246; (b) A. Priimagi, G. Cavallo, P. Metrangolo, G. Resnati, *Acc Chem Res.*, **2013**, 46, 2686–2695.
 - Pharmaceutical Salts and Co-Crystals*, ed. J. Wouters and L. Quéré, RSC Drug Discovery Series, **2012**.
 - (a) D. Braga, L. Maini, F. Grepioni, *Chem. Soc. Rev.*, **2013**, 42, 7638–7648; (b) S. A. Ross, D. A. Lamprou, D. Douroumis, *Chem. Commun.*, **2016**, 52, 8772–8786; (c) G. Bolla, A. Nangia, *Chem. Commun.*, **2016**, 52, 8342–8360.
 - A. Cruz-Cabeza, S. Reutzel-Edens, J. Bernstein, *Chem. Soc. Rev.*, **2015**, 44, 8619–8635.
 - O. S. Bushuyev, T. Frišćić, C. J. Barrett, *Cryst. Growth Des.*, **2016**, 16, 541–545.
 - (a) Q. Feng, M. L. Wang, B. L. Dong, J. He, C. X. Xu, *Cryst. Growth Des.*, **2013**, 13, 4418–4427.
 - B. Ventura, A. Bertocco, D. Braga, L. Catalano, S. d’Agostino, F. Grepioni, P. Taddei, *J. Phys. Chem. C*, **2014**, 118, 18646–18658.

14. (a) F. Grepioni, S. d'Agostino, D. Braga, A. Bertocco, L. Catalano, B. Ventura, J. *Mater. Chem.*, **2015**, 3, 9425–9434; (b) S. d'Agostino, F. Grepioni, D. Braga, B. Ventura, *Cryst. Growth Des.*, **2015**, 15, 2039–2045; (c) A. Carletta, F. Spinelli, S. d'Agostino, B. Ventura, M. R. Chierotti, R. Gobetto, J. Wouters, F. Grepioni, *Chem.–Eur. J.*, **2017**, 23, 5317–5329.

CHAPTER I: PHOTOREACTIONS IN THE SOLID STATE

I.1 Introduction

A photoreaction is defined as a chemical reaction that takes place under the effect of irradiation and can be performed either in solution or in the solid state. A solid-state photoreaction is a reaction that proceeds in the absence of solvent and is, in many cases, more efficient and faster than solution reactions, because of the high concentration accessible in the solid state.¹ Selectivity in the solid state is simple to control since molecules in crystals are constrained in a fairly rigid environment and regularly ordered.² Solid-state reactivity is of great interest, as a “green” (i.e. solvent-free) approach to the synthesis of new materials.³ In order to obtain solid-state photoreactions, the main issue is the correct alignment of molecules in the crystal packing (see Figure I.1). From this point of view, crystal engineering is a powerful tool to design crystals with predefined properties.⁴

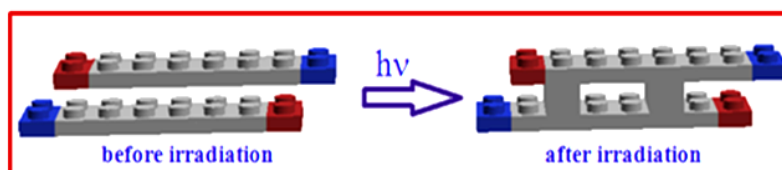


Figure I.1. Scheme of a [2+2] photoreaction involving properly aligned double bonds in the solid state.

Solid-state photoreactivity was extensively investigated by Schmidt and co-workers, who developed the well-known topochemical postulate, which states that, in order for a cycloaddition reaction to occur, the maximum distance between the reacting monomers should be 4.2 Å, and the double bonds should be aligned in a parallel fashion.⁵ Initially, Schmidt studied the [2+2] photoreactivity of cinnamic acid, then he extended the study to the [4+4] photoreactions. He affirmed that *the cinnamic acid photoreactivity is crystal-structure dependent* and in order to obtain the desired photoreactions in the solid state, *crystals should be engineered with appropriate contacts* in such a way as to possess suitable intermolecular alignment and distances.⁶

Following Schmidt's studies, others investigated on the solid state photoreactions, exploring different ways to align molecules in their crystals, i.e. the use of i) ionic

interactions by salt formation,⁷ ii) molecular templates,⁸ and iii) coordination to metal ions.⁹

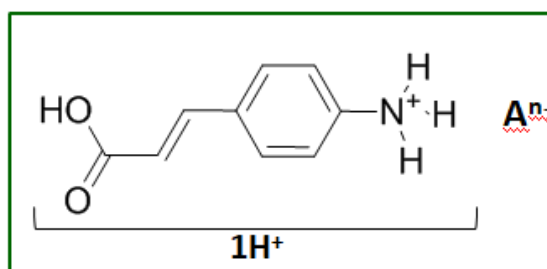
Currently, we have a good knowledge of how to lock molecules in place by means of crystal engineering; however, our ability to predict the final outcome of the photoreaction, i.e., what happens to the solid after irradiation, is still limited, and it is difficult to know in advance whether (i) the reaction proceeds by single crystal to single crystal transformation, ii) disintegration of the crystal occurs because of the stress generated within the crystal by atom movements during the photoreaction process, or iii) the crystal becomes amorphous, though maintaining the overall morphology. If the molecules involved in the photoreaction are small, the crystal is able to support the changes at the molecular level, and the effect of the stress generated in response to the reaction is limited to slight cracks and fractures emerging on the crystal surface. However, if the photoproduct is large, as it happens in some [4+4] photoreactions, the crystal cannot dissipate the large stress produced, and it often breaks apart.

The conditions for both [2+2]¹⁰ and [4+4] solid state photoreactivity are analogous; the main requisite to be considered is the Schmidt's postulate. Some similarities and differences between these two different classes of reactions have been reported in the literature. Turowska-Tyrk and Trzop published a paper in which they reported that in all cases: "i) Molecules, involved in the photoreaction, have no fixed position in the crystal, but rather they move with the progress of the reaction; ii) the distance between the reacting atoms decreased as the reaction progressed." In addition, the following differences were observed: "i) It is not always possible to study the completeness of the [4+4] photoreactions, because of the crystal disintegration which has been explained by means of the shape of the reactant and the product molecules and their preferred packing; ii) in the case of [4+4] photoreactions, the distance between the reacting atoms changes more slowly with the progress of the reaction than in the case of [2+2] photodimerisations".¹¹

In this chapter a study conducted on the two different classes of photoreaction, i.e. [2+2] and [4+4] cycloadditions, is reported. We investigated on derivative salts of amino-cinnamic acid and on an anthracene derivative. Modifications of the crystal packing of the parent molecules was achieved with the use of salts in the first case - [2+2] photoreactions - and of complexes formation for the [4+4] photoreactions. We were able to follow a single crystal to single crystal transformation in the case of the [2+2] photoreactions, while the [4+4] photoreactions always resulted in the "disintegration" of the crystal specimens.

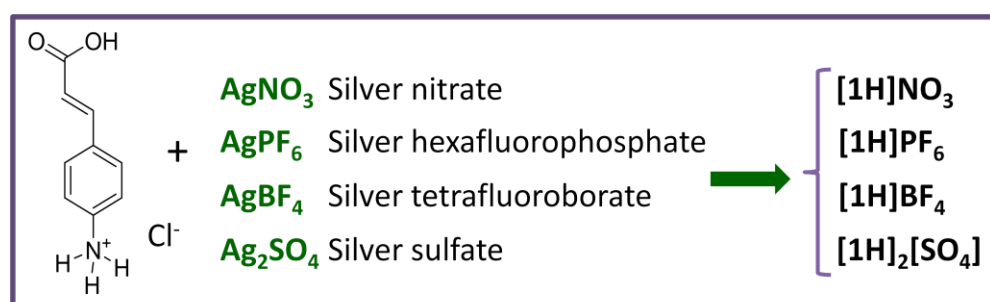
I.1.1 [2+2] PHOTOREACTIONS

This work was published in 2015 in Chemical Communication^{10,12}. The study was based on the solid state photoreactivity in a series of molecular salts of a cinnamic acid derivative. The salts have the general formula: $[\mathbf{1H}]_n\mathbf{A} \cdot x\mathbf{H}_2\mathbf{O}$, where $\mathbf{1}$ = 4-amino-cinnamic acid, \mathbf{A}^{n-} = inorganic anion, i.e. NO_3^- , BF_4^- , PF_6^- and SO_4^{2-} ; $x = 1$ in the case of SO_4^{2-} and 0 for the other anions (see Scheme I.1.1).



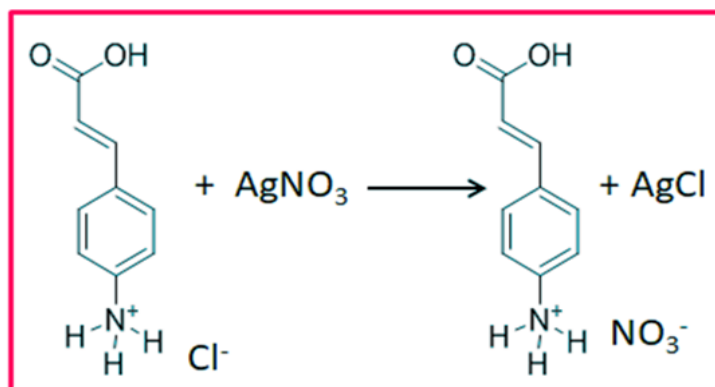
Scheme I.1.1. General scheme of the cation unit $[\mathbf{1H}]^+$ and the anion \mathbf{A}^{n-} of the investigated salts.

The goal was to obtain different arrangements of the cation unit $[\mathbf{1H}]^+$ in the crystal structure, by varying the size, the shape and the charge of the inorganic anions, in order to study the different behaviour of these compounds upon irradiation. The synthesis of the molecular salts was realized using an anion exchange reaction between the chloride salt of 4-amino-cinnamic acid and the appropriate silver salt (see Scheme I.1.2).



Scheme I.1.2. Anion exchange reactions performed between the chloride salt of 4-aminocinnamic acid and the silver salts.

The reaction between the chloride salt of 4-aminocinnamic acid and silver nitrate is shown in Scheme I.1.3 to give an example; the others were performed in the same way.



Scheme I.3. Scheme of the reaction between the chloride salt of 4-aminocinnamic acid and silver nitrate.

All compounds were structurally characterised by means of single crystal X-ray diffraction, with the exception of [1H]NO₃, for which the structure was solved from powder X-ray diffraction data.

Photoreactions for such class of compounds have been performed using a LED ($\lambda = 365$ nm) and have been monitored by means of polarized light microscopy and single crystal X-ray diffraction. Following the structural response to UV irradiation, via single crystal XRD at various irradiation intervals, it has been possible to conduct a detailed kinetic study directly in the single crystal (SC) medium. Scanning Electron Microscopy (SEM) was an advantageous tool which allowed the observation of morphological changes on the surface of the crystals during the photoreaction process.

I.1.2 Results and discussion

Salts have been prepared by anion exchange reactions as reported in the experimental section. Crystals suitable for the X-ray single crystal diffraction analysis were obtained by slow evaporation from water and ethanol, with the exception of [1H]NO₃, whose structure was solved from powder diffraction data. In the case of the sulphate [1H]₂SO₄·H₂O and the tetrafluoroborate [1H]BF₄ salts, we observed the formation of two polymorphic forms, form I and form II.

II.1.2.1 Structures of the salts

[1H]Cl crystallises in the P2₁/c monoclinic space group; the asymmetric unit is constituted by one [1H]⁺ and one Cl⁻ ion. In its crystal structure it is possible to identify a 2D network,

formed by the cationic unit $[\mathbf{1H}]^+$ and the anion Cl^- , held together by hydrogen bonds (see Figure I.1.1).

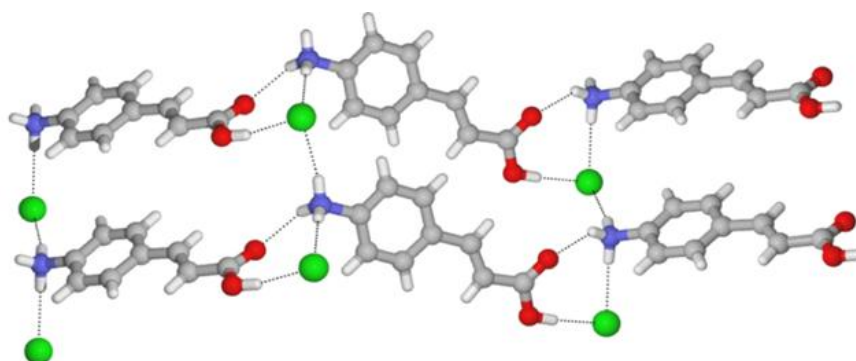


Figure I.1.1. Hydrogen bonds in $[\mathbf{1H}]\text{Cl}$, $[N(H)_{\text{NH}_3^+} \cdots \text{Cl}^- = 3.140(4) - 3.194(4) \text{ \AA}$, $\text{O(H)}_{\text{OH}} \cdots \text{Cl}^- = 3.056(3) \text{ \AA}$, and $N(H)_{\text{NH}_3^+} \cdots \text{O}=\text{C}_{\text{COOH}} = 2.801(4) \text{ \AA}$].

$[\mathbf{1H}]\text{NO}_3$ crystallises in the monoclinic space group $\text{P}2_1/\text{c}$. In the asymmetric unit one $[\mathbf{1H}]^+$ cation and one NO_3^- anion are observed. Its structure features a 3D network of hydrogen bonds among the ionic species $[\mathbf{1H}]^+$ and NO_3^- (see Figure I.1.2).

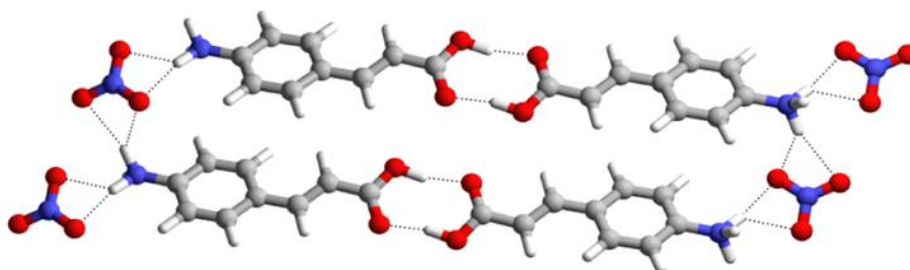


Figure I.1.2. Hydrogen bonds in $[\mathbf{1H}]\text{NO}_3$, $[N(H)_{\text{NH}_3^+} \cdots \text{O}_{\text{NO}_3^-} = 2.793(2) - 2.932(3) \text{ \AA}$, $\text{C(H)}_{\text{COOH}} \cdots \text{O}=\text{C}_{\text{COOH}} = 2.677(2) \text{ \AA}$].

In the case of the sulphate salt, $[\mathbf{1H}]_2\text{SO}_4 \cdot \text{H}_2\text{O}$, two polymorphic forms have been obtained: $[\mathbf{1H}]_2\text{SO}_4 \cdot \text{H}_2\text{O}$ (I) and $[\mathbf{1H}]_2\text{SO}_4 \cdot \text{H}_2\text{O}$ (II) respectively (see Figures I.1.3 and I.1.4).

$[\mathbf{1H}]_2\text{SO}_4 \cdot \text{H}_2\text{O}$ (I) crystallises in the space group $\text{P}2_1/\text{c}$ as well, with two $[\mathbf{1H}]^+$, one SO_4^{2-} ions and one water molecule in the asymmetric unit. In its crystal structure is possible to identify the presence of a complex 3D network of hydrogen bonds between the ionic species $[\mathbf{1H}]^+$, SO_4^{2-} and the water molecule (see Figure I.1.3).

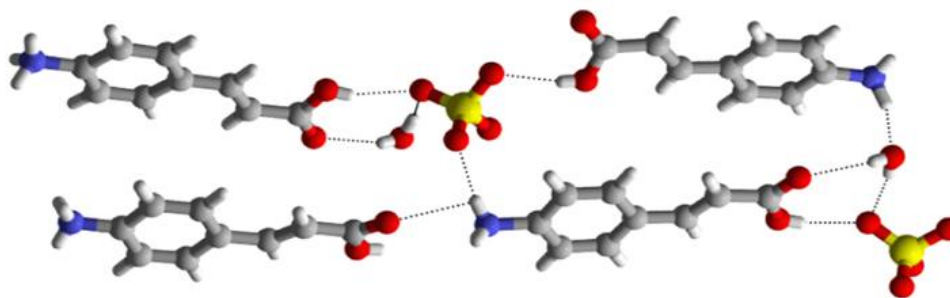


Figure I.1.3. Hydrogen bonds in $[\mathbf{1H}]_2[\text{SO}_4]\cdot\text{H}_2\text{O}$ (I), $[N(H)_{\text{NH}_3^+}\cdots O_{\text{SO}_4^{2-}} = 2.695(6) - 2.805(6) \text{ \AA}$,
 $O(H)_{\text{COOH}}\cdots O_{\text{SO}_4^{2-}} = 2.674(5) - 2.778(7) \text{ \AA}$, $O(H)_{\text{w}}\cdots O_{\text{SO}_4^{2-}} = 2.881(6) \text{ \AA}$,
 $O(H)_{\text{w}}\cdots O=\text{C}_{\text{COOH}} = 2.840(7) \text{ \AA}$, $N(H)_{\text{NH}_3^+}\cdots O_{\text{w}} = 2.724(7) \text{ \AA}$, $N(H)_{\text{NH}_3^+}\cdots O=\text{C}_{\text{COOH}} = 2.859(5) \text{ \AA}$].

$[\mathbf{1H}]_2\text{SO}_4\cdot\text{H}_2\text{O}$ (II) crystallises instead in the triclinic space group P-1. The asymmetric unit is formed by two $[\mathbf{1H}]^+$ cationic units, one SO_4^{2-} anion and one water molecule. A complex 3D network of hydrogen bonds can be identified among the components (see Figure I.1.4).

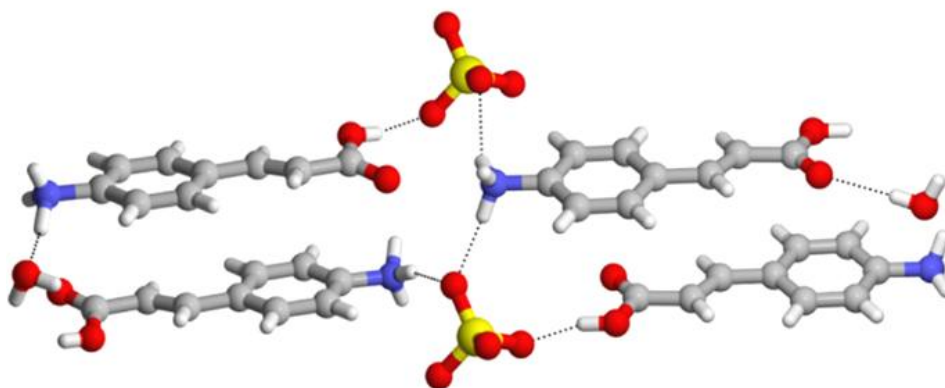


Figure I.1.4. Hydrogen bonds in $[\mathbf{1H}]_2[\text{SO}_4]\cdot\text{H}_2\text{O}$ (II), $[N(H)_{\text{NH}_3^+}\cdots O_{\text{SO}_4^{2-}} = 2.695(6) - 3.053(5) \text{ \AA}$,
 $O(H)_{\text{COOH}}\cdots O_{\text{SO}_4^{2-}} = 2.612(3) - 2.778(7) \text{ \AA}$, $O_{\text{w}}\cdots \text{SO}_4^{2-} = 2.781(7) - 2.881(6) \text{ \AA}$, $O_{\text{w}}\cdots O=\text{C}_{\text{COOH}} =$
 $2.840(7) - 2.900(4) \text{ \AA}$, $N(H)_{\text{NH}_3^+}\cdots O_{\text{w}} = 2.724(7) - 2.797(5) \text{ \AA}$,
 $N(H)_{\text{NH}_3^+}\cdots O=\text{C}_{\text{COOH}} = 2.850(4) - 2.859(5) \text{ \AA}$].

Similarly to $[\mathbf{1H}]_2\text{SO}_4\cdot\text{H}_2\text{O}$, two polymorphic forms of $[\mathbf{1H}]\text{BF}_4$ have been obtained: $[\mathbf{1H}]\text{BF}_4$ (I) and $[\mathbf{1H}]\text{BF}_4$ (II) (see Figures I.1.5 and I.1.6 respectively).

Compound $[\mathbf{1H}]\text{BF}_4$ (I) crystallises in the monoclinic space group I2/a. In the asymmetric unit one $[\mathbf{1H}]^+$ cation and one BF_4^- anion are present, and its structure features a 3D network of hydrogen bonds between $[\mathbf{1H}]^+$ and BF_4^- (see Figure I.1.5).

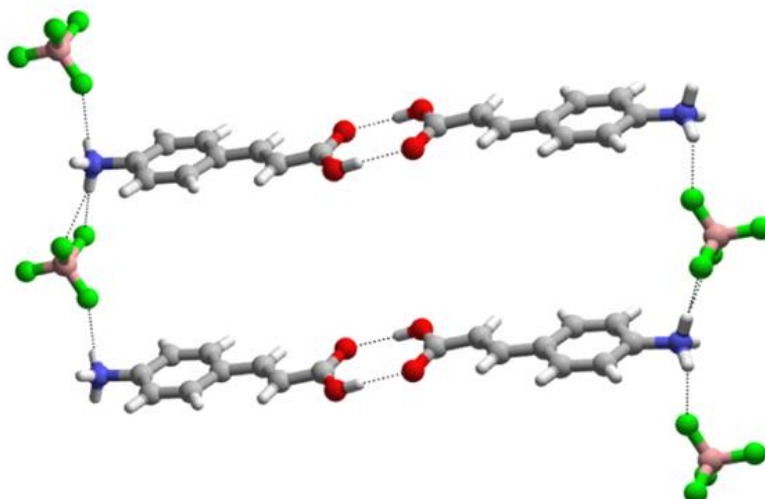


Figure I.1.5. Hydrogen bonds in [1H]BF₄ (I), [$N(H)_{NH_3^+} \cdots F_{BF_4^-} = 2.732(4) - 3.038(4) \text{ \AA}$,
 $O(H)_{COOH} \cdots O=C_{COOH} = 2.625(4) \text{ \AA}$].

Compound [1H]BF₄ (II) crystallises in the triclinic space group P-1, with one [1H]⁺ cation and one BF₄⁻ anion in the asymmetric unit. Its structure exhibits a 3D network of hydrogen bonds between the ions [1H]⁺ and BF₄⁻ (see Figure I.1.6).

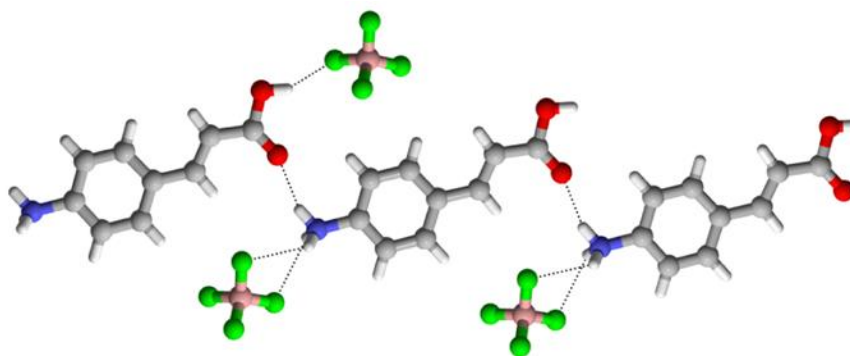


Figure I.1.6. Hydrogen bonds in [1H]BF₄ (II), [$N(H)_{NH_3^+} \cdots F_{BF_4^-} = 2.987(6) \text{ \AA}$,
 $N(H)_{NH_3^+} \cdots O=C_{COOH} = 2.829(5) \text{ \AA}$, $O(H)_{COOH} \cdots F_{BF_4^-} = 2.789(7) \text{ \AA}$].

Compound [1H]PF₆ crystallises in the space group P-1 with one [1H]⁺ cation and one PF₆⁻ anion in the asymmetric unit. Also in this case, a 3D network of hydrogen bonds between the ionic species [1H]⁺ and BF₄⁻ is observed (see Figure I.1.7).

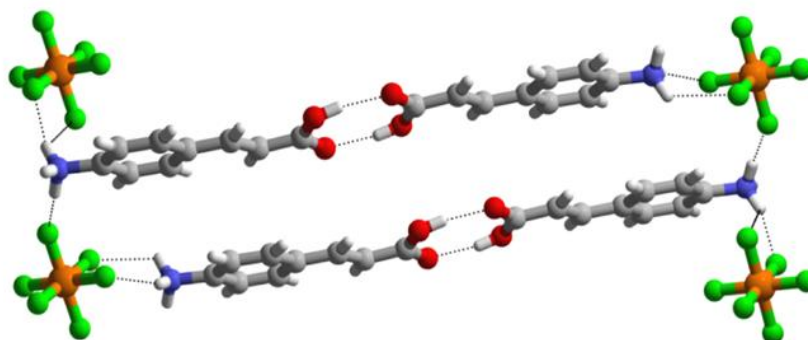
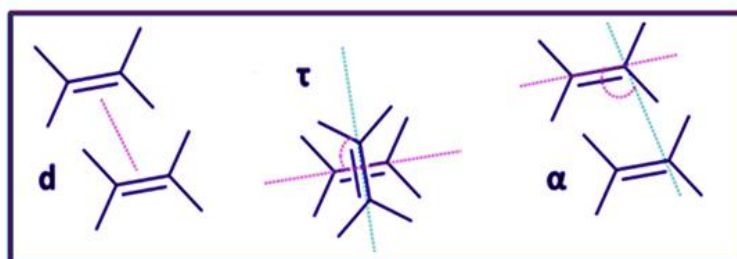


Figure I.1.7. Hydrogen bonds in $[1H]PF_6$, $[N(H)_{NH_3^+} \cdots F_{PF_6}^-] = 2.717(4) \text{ \AA}$,
 $O(H)_{COOH} \cdots O=C_{COOH} = 2.634(5) \text{ \AA}$.

II.1.2.2 Evaluation of the possible photoreactivity by geometrical parameters

A structural analysis of the geometrical parameters regarding the mutual orientation of neighboring molecules in the crystal has been performed. The geometrical parameters are named: d (distance between carbon atoms of C=C bonds in adjacent molecules, upper limit is 4.2 \AA), τ (torsion angle C=C \cdots C=C formed by the contiguous molecules), α (shift of one C=C bond along the second C=C)¹³ (see Scheme I.1.4).



Scheme I.1.4. Geometrical parameters used to evaluate photoreactivity of crystalline compounds.

In the case of the salts studied, for the evaluation of the geometrical parameters cited above were considered the neighbouring $[1H]^+$ cationic units in which are located the double bonds. Their values extracted from the crystal structures for all compounds are reported in Table I.1.1 where the arrangements for two cationic units $[1H]^+$ are reported as following: α = head-to-tail; β = head-to-head; - = no arrangement.

Table I.1.1. Types of arrangements observed in the salts studied and their relevant geometrical parameters used for the photoreactivity evaluation in the solid state.

	type	d (Å)	τ (°)	α (°)
[1H]Cl	α^a	3.657(5)	0	86.8(2)
[1H]NO ₃	α^a	4.128(2)	0	86.8(5)
[1H] ₂ [SO ₄]·H ₂ O (I)	α	4.769(5)	75.17(1)	57.73(8)
	β	4.423(1)	110.26(6)	83.89(7)
[1H] ₂ [SO ₄]·H ₂ O (II)	$\alpha 1^a$	3.524(5)	0	80.2(2)
	$\alpha 2$	4.726(6)	0	56.7(2)
[1H]BF ₄ (I)	-	-	-	-
[1H]BF ₄ (II)	$\alpha 1^a$	3.681(7)	0	74.4(3)
	$\alpha 2^a$	3.746(3)	0	88.67(2)
[1H]PF ₆	β	5.565(1)	0	56.72(3)

^a = double bonds related by an inversion center.

According to the geometrical parameters, the compounds [1H]Cl, [1H]NO₃, [1H]₂[SO₄]·H₂O (II) ($\alpha 1$), [1H]BF₄ (II) should be good candidates for photoreactivity (highlighted in Table I.1.1).

II.1.2.3 UV irradiation

The reactivity was firstly tested on a single crystal and then on polycrystalline material for each compound, with the exception of [1H]NO₃ which was available only as a polycrystalline powder. Millimeter-size single crystals used for structure determination were irradiated *ex-situ* at $\lambda = 365$ nm (for 12 h); the sample was placed at a distance of 1 cm from the lamp. Consequently, X-ray data collections were performed on the irradiated crystals in order to know if the cyclisation reaction was successful.

The reaction proceeded only in the case of [1H]Cl and [1H]₂SO₄·H₂O (II). For these two crystals, a slight reduction in the quality of the diffraction data was observed, but crystallinity was not compromised, as is shown in Figure I.1.8.

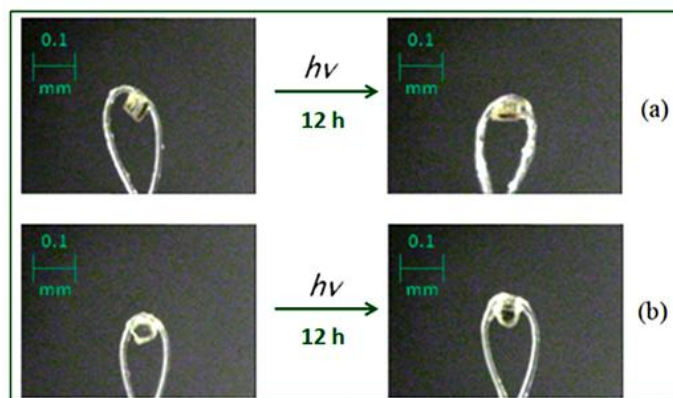


Figure I.1.8. Pictures of single crystals before and after irradiation for: [1H]Cl (a) and [1H]₂[SO₄]·H₂O (II) (b).

In the case of [1H]NO₃ and [1H]BF₄ (II), even if they have shown suitable values of the geometrical parameter "d", crystals were photostable. This can serve as a confirmation that the 4.2 Å empirical rule, although a necessary condition, is not sufficient to guarantee the outcome of the cycloaddition reaction.

I.1.2.4 Single crystal to single crystal photoreactions

Figure I.1.8 (top) shows how the single-crystal to single-crystal (SCSC) reaction, in the case of [1H]Cl and [1H]₂[SO₄]·H₂O (II), proceeds without loss of crystallinity. In both cases, an increase in the cell volume at the beginning of transformation, and a decrease when the reaction is completed can be observed.¹¹

In the single crystal of [1H]Cl the photoreaction proceeds quantitatively (Figure I.1.9).

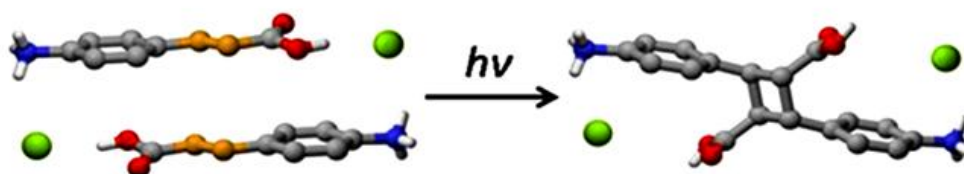


Figure I.1.9. Scheme of the [2+2] photoreaction in [1H]Cl.

Some variations in the unit cell parameters and a significant contraction of the cell volume (−5.2 %) are associate with the reaction (see Table I.1.2). The percentage shown in Table I.1.2 is related to the monomer of [1H]Cl.

Table I.1.2. Crystal data and details of measurements in crystalline [1H]Cl, for each stage of the photodimerisation.

	[1H]Cl	[1H]Cl 86%	[1H]Cl 80%	[1H]Cl 74%	[1H]Cl 68%	[1H]Cl 51%	[1H]Cl 41%	[1H]Cl 37%	[1H]Cl 25%	[1H]Cl 0%
a (Å)	5.5837(7)	5.6063(2)	5.6180(3)	5.6294(5)	5.6409(5)	5.6523(7)	5.6523(7)	5.6907(5)	5.7167(6)	5.7431(17)
b (Å)	8.5339(10)	8.5811(7)	8.5855(7)	8.5824(8)	8.5631(8)	8.5616(14)	8.5616(14)	8.4732(18)	8.417(2)	8.221(3)
c (Å)	19.865(2)	19.4662(17)	19.373(2)	19.252(3)	19.131(3)	19.105(5)	19.105(5)	18.860(3)	18.889(3)	19.012(6)
β (deg)	92.074(11)	91.595(7)	91.521(7)	91.427(9)	91.475(10)	91.471(17)	91.471(17)	91.741(9)	91.904(10)	92.47(3)
V (Å ³)	946.0(2)	936.12(12)	934.08(15)	929.83(19)	923.78(19)	924.3(3)	913.1(2)	909.0(2)	908.4(3)	896.8(5)

The hydrogen bond distances are shown in Figure I.1.10.

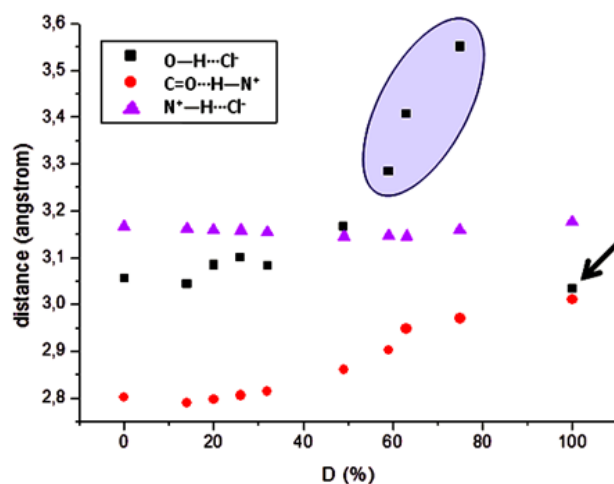


Figure I.1.10. Variation of hydrogen bonding distances during the course of the photoreaction in crystalline [1H]Cl. D (%) is the percentage of the dimer of [1H]Cl formed during the reaction. The violet area highlights the loss of hydrogen bonding interaction observed during the course of the reaction.

Instead, a less pronounced variation in the unit cell parameters and also in the cell volume (−1.6 %) was observed in the case of [1H]₂SO₄·H₂O (II) (see Table I.1.3). These minor changes can be ascribed to the fact that only the α 1 dimer is photoreactive (see Figure I.1.11). The percentage shown in Table I.1.3 is related to the monomer of [1H]₂SO₄·H₂O (II).

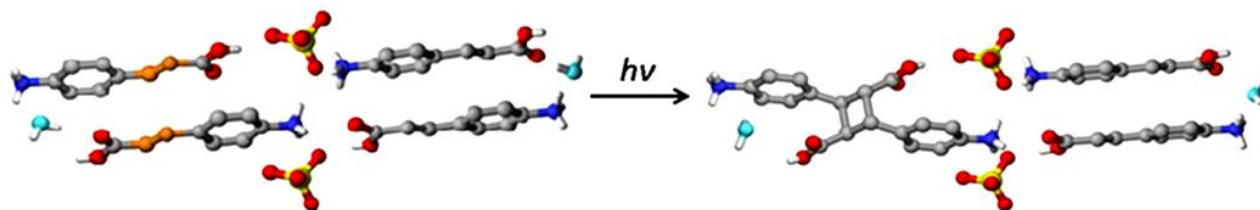


Figure I.1.11. Scheme of the [2+2] photoreaction in $[\mathbf{1H}]_2[\text{SO}_4]\cdot\text{H}_2\text{O}$ (II).

Table I.1.3. Crystal data and details of measurements for crystalline $[\mathbf{1H}]_2\text{SO}_4\cdot\text{H}_2\text{O}$ (II) and for each stage of its photodimerisation.

	$[\mathbf{1H}]_2\text{SO}_4\cdot\text{H}_2\text{O}$ (II)	$[\mathbf{1H}]_2\text{SO}_4\cdot\text{H}_2\text{O}$ (II) 88%	$[\mathbf{1H}]_2\text{SO}_4\cdot\text{H}_2\text{O}$ (II) 70%	$[\mathbf{1H}]_2\text{SO}_4\cdot\text{H}_2\text{O}$ (II) 58%	$[\mathbf{1H}]_2\text{SO}_4\cdot\text{H}_2\text{O}$ (II) 27%	$[\mathbf{1H}]_2\text{SO}_4\cdot\text{H}_2\text{O}$ (II) 20%	$[\mathbf{1H}]_2\text{SO}_4\cdot\text{H}_2\text{O}$ (II) 0%
a (Å)	7.3374(8)	7.3066(9)	7.2590(10)	7.2497(10)	7.1238(19)	7.0960(5)	7.0956(7)
b (Å)	10.5566(12)	10.5681(17)	10.5719(15)	10.6164(17)	10.631(2)	10.6518(9)	10.6597(13)
c (Å)	13.8798(15)	13.8909(16)	13.8895(18)	13.902(2)	13.925(3)	13.9338(12)	13.9430(15)
α (deg)	103.793(10)	104.253(12)	104.423(12)	104.762(14)	106.010(17)	106.307(8)	106.348(10)
β (deg)	99.924(9)	99.577(10)	98.792(11)	98.258(13)	95.898(18)	95.377(7)	95.271(9)
γ (deg)	102.838(10)	102.609(12)	102.601(12)	102.574(13)	102.081(19)	101.948(7)	101.923(10)
V (Å ³)	988.76(19)	986.7(2)	982.9(2)	987.2(3)	976.7(4)	975.91(14)	977.41(19)

Hydrogen bonds distances remain almost unaltered as well as the case of the chloride salt (see Figure I.1.12 for the reactive arrangement (α_1) and Figure I.1.13 for the arrangement α_2).

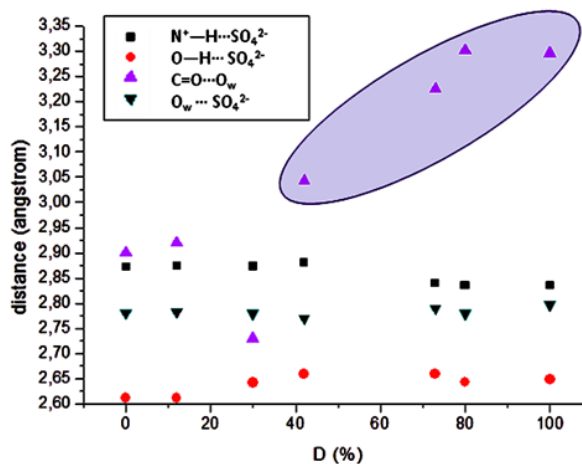


Figure I.1.12. Variation of hydrogen bonding distances during the course of the photoreaction in $[\mathbf{1H}]_2\text{SO}_4\cdot\text{H}_2\text{O}$ (II) for the reactive arrangement (α_1). D (%) is the percentage of the dimer of $[\mathbf{1H}]_2\text{SO}_4\cdot\text{H}_2\text{O}$ (II) formed during the reaction. The violet area highlights the loss of hydrogen bonding interaction observed during the course of the reaction.

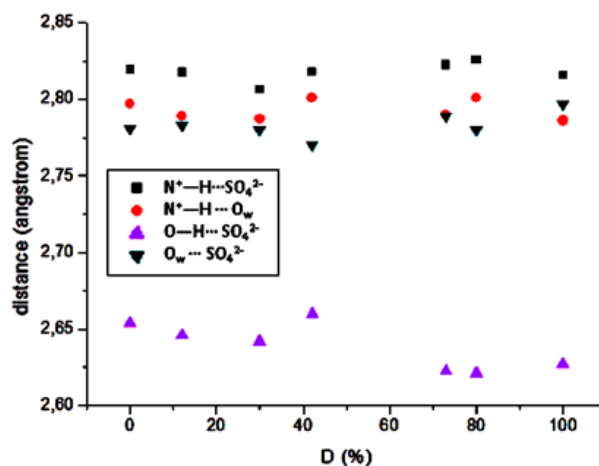


Figure I.1.13. Variation of hydrogen bonding distances during the course of the photoreaction $[\text{1H}]_2\text{SO}_4\cdot\text{H}_2\text{O}$ (II) for the no-reactive arrangement (α_2).

Figures I.1.14 and I.1.15 show plots of the variation of cell parameters with the cell volume, for $[\text{1H}]\text{Cl}$ and $[\text{1H}]_2[\text{SO}_4]\cdot\text{H}_2\text{O}$ (II) respectively, upon UV irradiation, over a similar time interval.

Changes in the unit cell volumes, determined by single crystal X-ray diffraction, before and after irradiation, are reported: for the starting and reacted crystals, respectively $945.962(1) \text{ \AA}^3$ and $896.799(5) \text{ \AA}^3$ for $[\text{1H}]\text{Cl}$, and $988.758(2) \text{ \AA}^3$ and $977.415(1) \text{ \AA}^3$ for $[\text{1H}]_2\text{SO}_4\cdot\text{H}_2\text{O}$ (II).

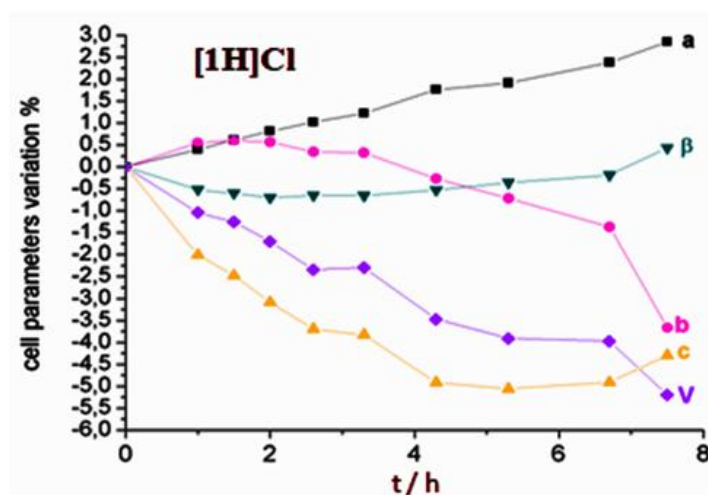


Figure I.1.14. Plots of the variation of the cell parameters over the course of UV irradiation for $[\text{1H}]\text{Cl}$ (time expressed in hours, t/h).

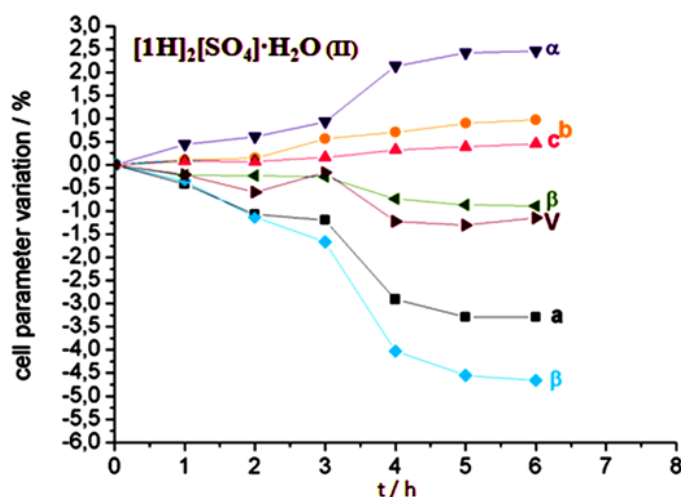


Figure I.1.15. Plots of the variation of the cell parameters over the course of UV irradiation for $[1H]_2[SO_4] \cdot H_2O$ (II) (time expressed in hours, t/h).

Polarized light microscopy

Figure I.1.16 shows the morphological changes on the surface of a crystal of $[1H]Cl$, before and after the UV irradiation. Starting from the reactant (monomers), it is possible to obtain the product (dimer), in the same crystal, by irradiation; this is why it is called a single crystal to single crystal transformation (SCSC).

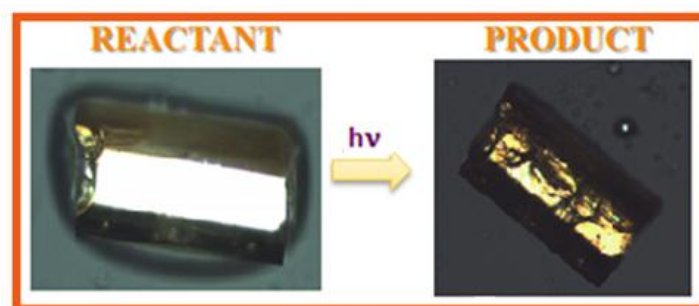


Figure I.1.16. Pictures of the SCSC photoreaction for $[1H]Cl$ crystal.

Before the irradiation the crystal surface is smooth, while after the UV treatment several cracks appear on its surface. This is due to the small movements of the atoms during the photoreaction, which promote the formation of cracks in the crystal.

Figures I.1.17 and I.1.18 show several pictures taken with a cross-polarized light microscope during the irradiation process, at intervals of 2 hours, on two selected crystals of $[1H]Cl$ and $[1H]_2[SO_4] \cdot H_2O$ (II), respectively. The number of cracks on the surface of the crystals increased as the irradiation progressed.

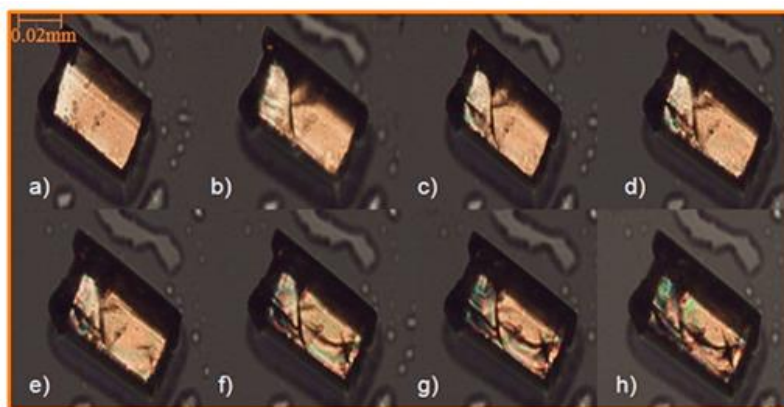


Figure I.1.17. Optical microscopy pictures of the SCSC transformation in $[1H]Cl$.

A larger volume contraction, i.e. greater stress within the crystal, was observed in the case of $[1H]Cl$, compared to $[1H]_2[SO_4] \cdot H_2O$ (II). This observation may justify the extent of the damage to the chloride single crystal surface, when compared to the analogous sulphate crystal, after only a few hours of exposure to UV radiation (see Figures I.1.17 and I.1.18).

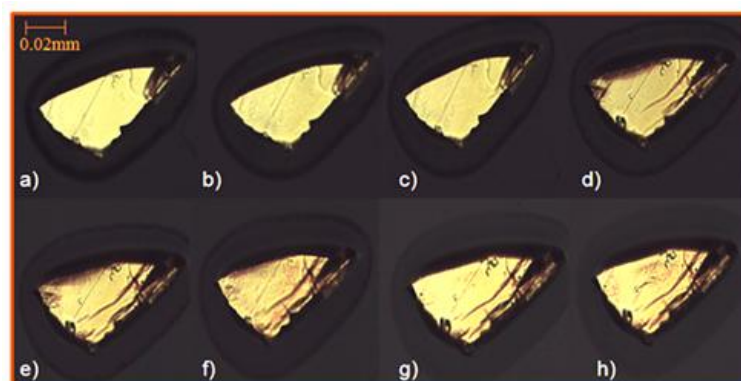


Figure I.1.18. Optical microscopy pictures of the SCSC transformation in $[1H]_2[SO_4] \cdot H_2O$ (II).

Scanning Electron Microscopy

SEM was used to confirm the differences in the behaviour of the two crystals during the irradiation process, which were first observed with the polarized light microscope. Figures I.1.19 and I.1.20 show the micrographs of single crystals of $[1H]Cl$ and $[1H]_2SO_4 \cdot H_2O$ (II) taken before and after overnight irradiation.

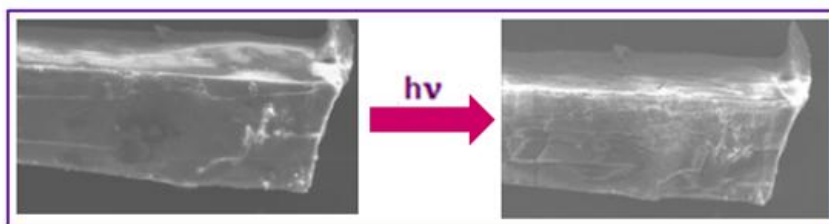


Figure I.1.19. Pictures of the single crystal of $[1H]Cl$ before and after irradiation (zoom: $10\ \mu m$).

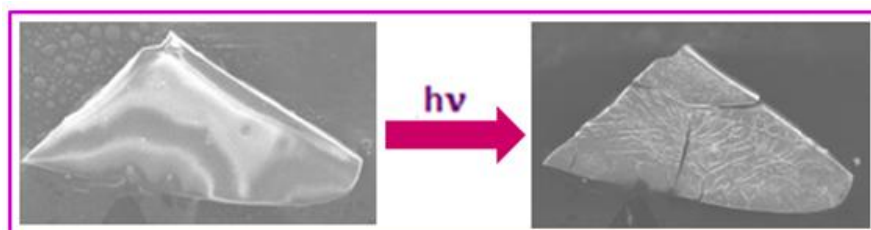


Figure I.1.20. Pictures of the single crystal of $[1H]_2[SO_4]\cdot H_2O$ (II) before and after irradiation (zoom: $50\ \mu m$).

Although both crystals retain their overall integrity, it is clearly seen in Figure I.1.21 that the crystal surface of $[1H]Cl$ appears more cracked, compared with the one of $[1H]_2SO_4\cdot H_2O$ (II), as a result of the UV irradiation and structural change.

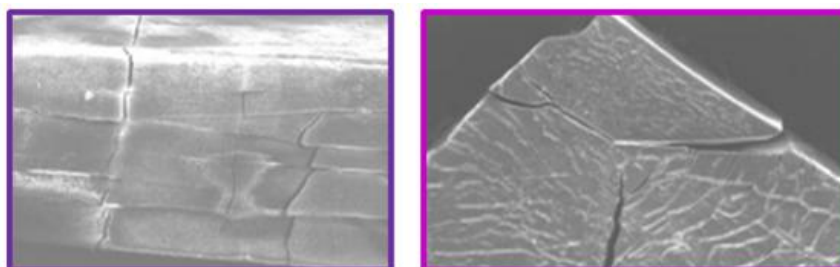


Figure I.1.21. An enlargement of the pictures of crystals $[1H]Cl$ (left) and $[1H]_2[SO_4]\cdot H_2O$ (II) (right), after the irradiation process (zoom: $5\ \mu m$ and $20\ \mu m$, respectively).

I.1.2.5 Powder X-ray diffraction

A comparison of chemical and structural identity between bulk materials and single crystals was verified, when possible, by comparing simulated and experimental powder diffraction patterns (see Figures A.2 - A.6 in Appendix A).

Irradiation experiments were also conducted on polycrystalline materials, with the exception of $[1H]_2SO_4\cdot H_2O$ (II), which was obtained as a mixture of two polymorphic forms, form I and II, of which the form I was photostable. Thus, it was not possible to

select only the crystals of $[\mathbf{1H}]_2\text{SO}_4\cdot\text{H}_2\text{O}$ (II) for the irradiation of powder. Attempts were made to separate the two polymorphic forms, e.g. crystallisation by seed, but without success.

Figure I.1.22 shows a comparison of the calculated and experimental patterns for $[\mathbf{1H}]\text{Cl}$ at different intervals of irradiation, i.e., before irradiation (starting materials), after 4 hours (60% conversion) and after 12 hours (100% conversion).

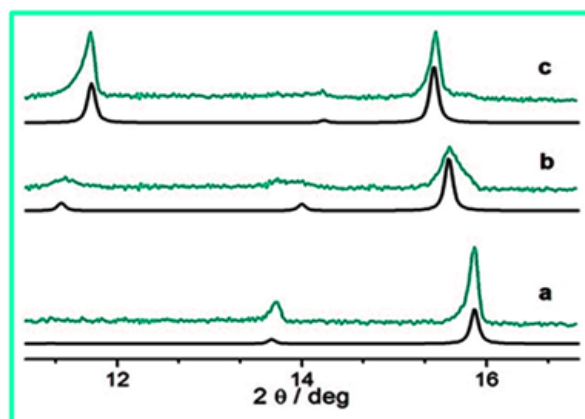


Figure I.1.22. XRPD comparison between calculated (black line) and experimental (green line) for $[\mathbf{1H}]\text{Cl}$ recorded during the UV irradiation: a) before the irradiation; b) after 4 hours and c) after 12 hours of irradiation.

Figure I.1.22b shows a peak broadening after 4h of irradiation, which could be caused by the presence of solid solutions at different stages of reactivity. This effect could be due to two phenomena: i) the inhomogeneous permeation of the UV radiation into the material; ii) the different particle size distribution in the polycrystalline sample.

Attenuated total reflectance (ATR) Fourier transform infrared (FT-IR) spectroscopy

Polycrystalline materials were also subjected to Attenuated Total Reflectance Fourier Transform IR (ATR-FTIR) measurements before and after the UV irradiation. Even in this case, the sulphate salt was not tested because of the impossibility of separating the two polymorphic forms.

Good results have been obtained for the compound $[\mathbf{1H}]\text{Cl}$, the other two were photostable (see Figure I.1.23). The spectra show the shift of the characteristic band of the conjugated C=O stretching, from 1690 cm^{-1} to 1710 cm^{-1} , due to the deconjugation of the carbonyl group. A disappearance of the olefinic C=C stretching (1639 cm^{-1}) has also been observed

after the [2+2] photodimerisation (see Figure I.1.24). These changes are in agreement with what observed by Chu and co-workers for similar systems.¹⁴

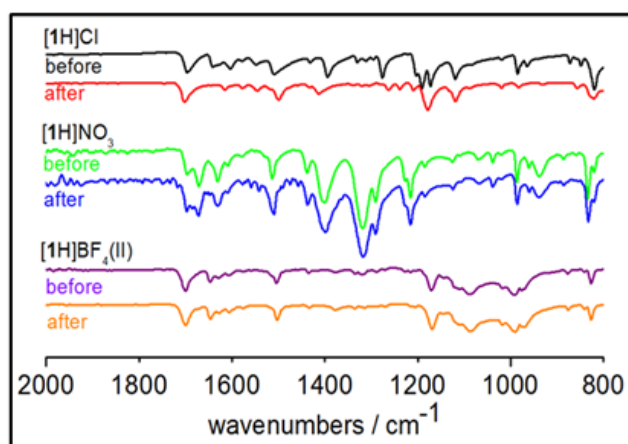


Figure I.1.23. ATR-FTIR spectra of compounds [1H]Cl, [1H]NO₃ and [1H]BF₄ (II) recorded before and after overnight irradiation ($\lambda = 365$ nm).

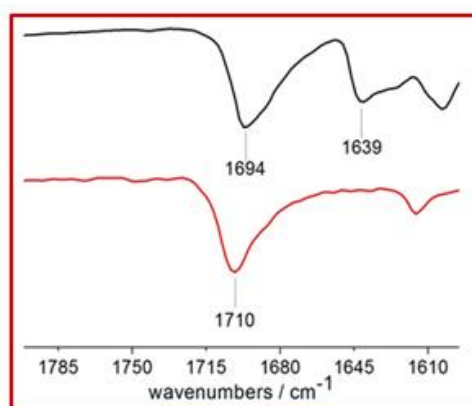


Figure I.1.24. An enlarged portion of the ATR-FTIR spectra for [1H]Cl, run before and after the UV irradiation.

NMR spectroscopy

A polycrystalline sample of [1H]Cl was also investigated by NMR spectroscopy.

Spectra of polycrystalline samples were collected before and after the overnight irradiation ($\lambda = 365$ nm). The completion of the photodimerisation for [1H]Cl was confirmed by the disappearing of peaks at 7.5 and 6.4 ppm, characteristic to the olefins, and the appearance of cyclobutane protons at 4.3 and 3.8 ppm. Data are reported as follows: chemical shift, multiplicity (d = doublet, dd = double doublet), coupling constants (Hz), and number of protons (nH) (see Figure I.1.25).

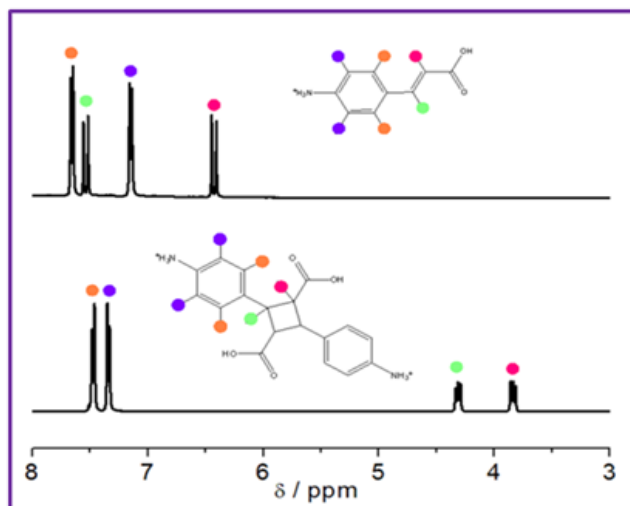


Figure I.1.25. ^1H NMR spectra of $[\mathbf{1H}]\text{Cl}$ run before (top) and after (bottom) overnight irradiation. Before irradiation: $[\mathbf{1H}]\text{Cl}$ (DMSO- d_6 , 400 Hz): 7.66 (d, $J = 8.2$ Hz, 2H), 7.54 (d, $J = 16$ Hz, 2H), 7.15 (d, $J = 8.2$ Hz, 1H), 6.43 (d, $J = 16$ Hz, 1H). After irradiation: $[\mathbf{1}_2\text{H}_2]\text{Cl}_2$ (DMSO- d_6 , 400 Hz): 7.47 (d, $J = 8.2$ Hz, 4H), 7.34 (d, $J = 8.2$, 4H), 4.31 (dd, $J = 10$ Hz / 7.5 Hz, 2H), 3.84 (dd, $J = 10$ Hz / 7.5 Hz, 2H).

In the case of $[\mathbf{1H}]\text{Cl}$, the regular shape of single crystals has allowed the face indexing. Figure I.1.26 shows that the reactive double bonds are arranged perpendicularly to the crystallographic direction $[010]$ and the side groups are situated in the bc -plane. When the cyclobutane ring is formed, the side groups bend outward; therefore a significant variation of the cell constants is observed along the axis b and c (-3.67 % and -4.29 %, respectively), which are located orthogonally to the crystallographic direction of growth $[100]$. The side groups are responsible for the strain and stress, generated within the crystal, during the irradiation process.

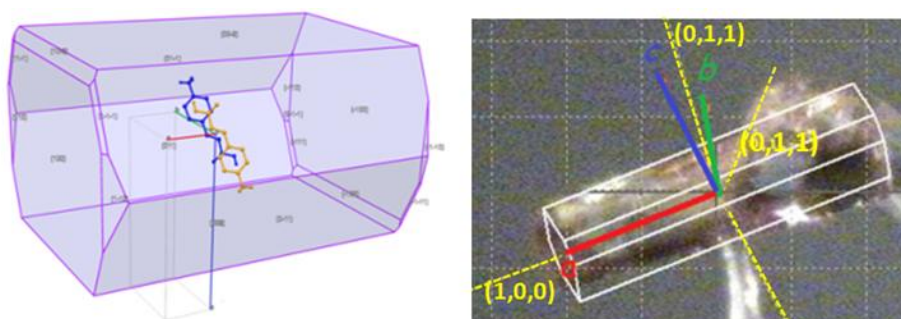


Figure I.1.26. External morphology of the single crystals of $[\mathbf{1H}]\text{Cl}$: simulated BDFH on the basis of single crystal structure (left) and experimentally determined after face indexing. In blue and orange are evidenced the reactive $[\mathbf{1H}]^+$ cationic units.

II.1.3 Conclusions

In this work we have synthesised and structurally characterised seven molecular salts with general formula $[\mathbf{1H}]_n\text{A}\cdot x\text{H}_2\text{O}$, where $\mathbf{1}$ = 4-amino-cinnamic acid, A^{n-} = inorganic anion, i.e. NO_3^- , BF_4^- , PF_6^- and SO_4^{2-} ; $x = 1$ in the case of SO_4^{2-} and 0 for the other anions.

We observed that the solid state photoreaction, by means of UV light, has taken place in the cases of the chloride and the sulphate (polymorph II) salts while the other salts were photostable. Photoreactions for $[\mathbf{1H}]\text{Cl}$ and $[\mathbf{1H}]_2\text{SO}_4\cdot\text{H}_2\text{O}$ (II) were followed by single crystal X-ray diffraction (ex situ irradiation), which revealed a zero-order kinetic behaviour. The process of irradiation was also monitored by cross-polarized optical microscopy and SEM, which have shown that upon irradiation the crystal of $[\mathbf{1H}]\text{Cl}$ seems more stressed than those of $[\mathbf{1H}]_2\text{SO}_4\cdot\text{H}_2\text{O}$ (II). An interesting result was found in the case of the $[\mathbf{1H}]_2\text{SO}_4\cdot\text{H}_2\text{O}$ (II) in which only one arrangement of the cation units $[\mathbf{1H}]^+$ in the crystal packing was reactive.

XRPD measurements, run during in situ irradiation of polycrystalline sample of $[\mathbf{1H}]\text{Cl}$, indicate that the photoreaction proceeds via formation of a solid state solution between reactant and product. This was confirmed by comparison of the experimental and calculated (from the crystal structures solved at different irradiation intervals) patterns.

We have also investigated polycrystalline samples of $[\mathbf{1H}]\text{Cl}$ via FT-IR and NMR spectroscopy.

II.1.4 Experimental section

All reactants were purchased from Sigma-Aldrich and used without further purification.

Syntheses have been conducted by reaction between 4-amino-cinnamic acid ($\mathbf{1}$) and HCl to obtain the chloride salt $[\mathbf{1H}]\text{Cl}$. It was followed by an anion exchange reaction with the appropriate silver salt used as halide abstraction reagent.

$[\mathbf{1H}]\text{Cl}$: 200 mg (1.23 mmol) of 4-amino-cinnamic acid ($\mathbf{1}$) were dissolved in aqueous HCl (pH 2). After filtration of the aqueous solution, colorless crystals of $[\mathbf{1H}]\text{Cl}$, suitable for X-ray crystal diffraction, were obtained after 7 days.

$[\mathbf{1H}]\text{NO}_3$: 120 mg (0.72 mmol) of AgNO_3 were dissolved in 10 mL of EtOH and to the resulting solution 140 mg (0.72 mmol) of $[\mathbf{1H}]\text{Cl}$ were added and kept under stirring, in the dark, for 5 hours. The precipitated AgCl was filtered off. A white powder of $[\mathbf{1H}]\text{NO}_3$ was obtained, after 3 days, from slow evaporation of solvent.

$[\mathbf{1H}]_2\text{SO}_4\cdot\text{H}_2\text{O}$: 200 mg (0.64 mmol) of Ag_2SO_4 were dissolved in 10 mL of water, to this 130 mg (0.64 mmol) of $[\mathbf{1H}]\text{Cl}$ were added and stirred in the dark for 5 hours. The

precipitated AgCl was filtered off. Slow evaporation of the solution after 1 week afforded crystals suitable for X-ray diffraction in two polymorphic forms: $[\mathbf{1H}]_2\text{SO}_4 \cdot \text{H}_2\text{O}$ (I) and $[\mathbf{1H}]_2\text{SO}_4 \cdot \text{H}_2\text{O}$ (II). A pure polycrystalline phase of polymorph (I) was obtained by seeding in water, while it was not possible to obtain a pure phase for $[\mathbf{1H}]_2\text{SO}_4 \cdot \text{H}_2\text{O}$ (II), which was invariably contaminated by Form I.

$[\mathbf{1H}]\text{BF}_4$: 100 mg (0.51 mmol) of AgBF_4 were dissolved in 10 mL of water and 100 mg (0.5 mmol) of $[\mathbf{1H}]\text{Cl}$ were added and kept under stirring in the dark for 5h. The precipitated AgCl was filtered off. Slow evaporation of the solution, after 3 days, afforded crystals suitable for X-ray diffraction of both $[\mathbf{1H}]\text{BF}_4$ (I) and $[\mathbf{1H}]\text{BF}_4$ (II) forms. Pure polycrystalline phases of both polymorphs were obtained by seeding solutions of EtOH or water.

$[\mathbf{1H}]\text{PF}_6$: 100 mg (0.4 mmol) of AgPF_6 were dissolved in 8 mL of water and 80 mg (0.4 mmol) of $[\mathbf{1H}]\text{Cl}$ were added and kept under stirring in the dark for 5h. The precipitated AgCl was filtered off. Yellow crystals of $[\mathbf{1H}]\text{PF}_6$ suitable for X-ray diffraction were obtained from slow evaporation of the solvent, after 1 week.

Characterisation

Single crystal X-ray diffraction: Single-crystal data for all compounds (except $[\mathbf{1H}]\text{NO}_3$) were collected at RT on an Oxford X'Calibur S CCD diffractometer equipped with a graphite monochromator (Mo- K_α radiation, $\lambda = 0.71073 \text{ \AA}$). Data collection and refinement details are reported in Appendix A (see Tables A.1 - A.3). All non-hydrogen atoms were refined anisotropically, while the C atoms of the disappearing double bond and appearing cyclobutane in partially reacted crystals were treated as disordered over two positions and refined isotropically; H_{CH} atoms for all compounds were added in calculated positions and refined riding on their respective carbon atoms; H_{OH} and H_{NH} atoms were either directly located or, when not possible, added in calculated positions. SHELX97¹⁵ was used for structure solution and refinement on F^2 . The program Mercury¹⁶ was used to calculate intermolecular interactions. CYLview¹⁷ and Mercury¹⁶ were used for molecular graphics.

Structure determination and refinement from powder data: Powder diffraction data for $[\mathbf{1H}]\text{NO}_3$ were collected in the 2θ range $5\text{--}60^\circ$ (step size, 0.003° ; time/step, 99s; 0.02 rad s⁻¹; $V \times A$ 40×40) on a Panalytical X'Pert PRO automated diffractometer operated in transmission mode (capillary spinner) and equipped with a Pixel detector. Powder diffraction data were analysed with the software EXPO 2010,¹⁸ which is designed to analyse monochromatic and non-monochromatic data. Peaks were automatically chosen in the 2θ range $4\text{--}40^\circ$, and a monoclinic cell was found (see Table A.1), using the algorithm

N-TREOR,¹⁹ with a volume of 1000.70 Å³. The structure was then solved by simulated annealing using a molecular model built with the Avogadro software,²⁰ and refined by Rietveld method using the software TOPAS 4.1.²¹ A shifted Chebyshev function with 7 parameters and a Pseudo-Voigt function (TCHZ type) were used to fit background and peak shape, respectively. A spherical harmonics model was used to describe the preferred orientation. A rigid body was applied on the two fragments. Bond distances and torsion angles were refined in a limited range around an equilibrium value. An overall thermal parameter for the C, N, O atoms was adopted. Refinement converged with $\chi^2 = 1.5$, $R_{wp} = 5.1\%$, $R_{exp} = 3.4\%$. Figure A.1 in Appendix A, shows experimental, calculated and difference patterns for [1H]NO₃.

Powder X-ray diffraction (PXRD): Diffraction patterns in the 2θ range 5 - 40° (step size 0.02°; time/step 20 s; 0.04 rad soller) were collected, using a glass sample holder, on a PANalytical X'Pert PRO automated diffractometer equipped with an X'Celerator detector and in Bragg-Brentano geometry, using Cu K α radiation without a monochromator. The tube voltage and amperage were set to 40 kV and 40 mA, respectively. The program Mercury¹⁶ was used for simulation of X-ray powder patterns on the basis of single crystal data. Chemical and structural identity between bulk materials and single crystals was always verified, when possible, by comparing experimental and simulated powder diffraction patterns.

Irradiation: Single crystal samples were irradiated, using a UV-LED (Led EnginLZ1-10UV00-0000, $\lambda = 365$ nm), on a slide placed at a distance of 1 cm from the lamp. Powder samples were instead placed onto a flat spinner sample holder and irradiated using two Led EnginLZ1-10UV00-0000 ($\lambda = 365$ nm) placed at a distance of 2 cm from the sample. X-ray powder diffraction patterns were recorded every 4 minutes until the reaction was complete, (the difference in the distance of the lamp has been chosen in order to better penetrate the crystal, otherwise, the reaction would take place only on the surface of the crystal).

SEM: Morphological investigations of crystals were performed using a Philips XL-20 scanning electron microscope operating at 15 kV. The samples were observed as-prepared and not sputter coated before examination since it is possible to damage the crystals during this process. Sample preparation is as follows: single crystals were selected using the protective perfluoropolyether oil. The oil was first used to handle and select the best, successively crystals were washed up with ethyl acetate in order to remove the oil. For this

reason, in some areas of SEM micrographs, it is possible to see on the crystal surface the presence of tiny residues of perfluoropolyether, especially for $[\mathbf{1H}]_2\text{SO}_4 \cdot \text{H}_2\text{O}$ (II).

ATR-FTIR: ATR-FTIR (Attenuated Total Reflectance Fourier Transform IR) spectra were obtained using a Bruker Alpha FT-IR spectrometer and they were run on polycrystalline samples of $[\mathbf{1H}]\text{Cl}$, $[\mathbf{1H}]\text{NO}_3$ and $[\mathbf{1H}]\text{BF}_4$ (II) before and after overnight irradiation at $\lambda = 365$ nm.

NMR spectroscopy: ^1H -NMR spectra were recorded at the University of Turin on a Varian INOVA 400 (400 MHz) spectrometer. Dimethylsulfoxide- d_6 (DMSO- d_6) was used as solvent and chemical shifts are reported in ppm, using tetramethylsilane as the internal reference standard.

I.2.1 [4+4] PHOTOREACTIONS

The goal of this work²² was to investigate the [4+4] photoreactivity of the anthracene derivative 9-(methylaminomethyl)anthracene (MAMA, see Figure I.2.1).

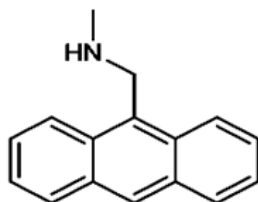
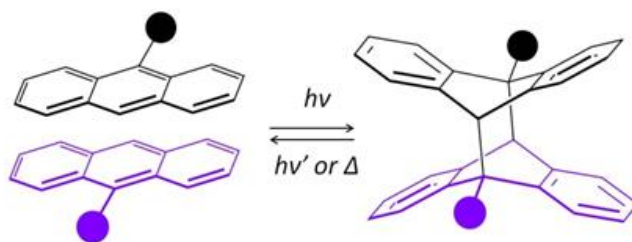


Figure I.2.1. Molecular structure of MAMA.

Photoreactivity has been tested in solution, in the gel medium and in the solid state.

Upon irradiation of an ethanol solution of MAMA, the formation of crystals of photoproduct was observed while the irradiation of a polycrystalline sample of MAMA was performed without success. The unfavourable orientations of the anthracene moieties in the crystal packing of MAMA could be responsible for the photostable behaviour of MAMA in the solid state. Thus, in order to achieve the [4+4] photoreaction (see Scheme I.2.2) of MAMA in the solid state, three complexes were synthesised - between MAMA and three silver salts (i.e. AgX, where X⁻ = PF₆⁻, BF₄⁻ or NO₃⁻) - by taking advantage of the coordination capability of the amino group in the molecule of MAMA.



Scheme I.2.2. Illustrative photochemical dimerisation of 9-substituted anthracenes.

Thus, we have also extended the study to the complexes [Ag(MAMA)₂][PF₆] and [Ag(MAMA)₂][BF₄] and to the coordination polymer [Ag(MAMA)₂][Ag(NO₃)₂]; in all solids the anthracene moieties were correctly aligned in the crystal packing to favour the photoreaction. All compounds were irradiated with UV light and were structurally characterised by means of single crystal and powder X-ray diffraction and by Raman spectroscopy.

II.2.2 Results and discussion

We focused primarily on the structural characterisation of MAMA, since no crystal structure was available in the Cambridge Structural Database (CSD). In order to study the photoreactivity of MAMA, a knowledge of how molecules are organized in the crystal packing is essential; thus many efforts were made to obtain suitable crystals for single crystal X-ray diffraction. To this purpose, different crystallisation methods have been used: i) crystallisation from several solvents (i.e. ethanol, methanol, propanol, dichloromethane, chloroform, toluene, ii) different crystallisation techniques, i.e. solvent evaporation, liquid and vapour diffusion, iii) crystal growth from gels using low-molecular-weight gelators (LMWG) (see Figure A.7 in Appendix A).²³

Unfortunately, all the attempts to obtain adequate single crystals, for structural characterisation, were unsuccessful. However, it was subsequently possible to solve the structure of MAMA from powder X-ray diffraction data, since recrystallisation from melt afforded a polycrystalline powder of suitable quality (see Figure A.8).

I.2.2.1 Crystal structures

Crystal data and crystallographic details for all compounds are reported in Table A.4 in Appendix A.

MAMA

MAMA crystallises in the triclinic P-1 space group. Figure I.2.2 shows the structure of MAMA as solved from powder diffraction data. The asymmetric unit contains two molecules of MAMA and the disubstituted amino groups of the MAMA form long hydrogen bonding interactions in pairs [$N_{NR_2H} \cdots N_{NR_2H} = 3.321(1) \text{ \AA}$]. In the crystal packing of MAMA the relative arrangement of the aromatic rings with displaced double bonds and herring-bone motif hinders the [4+4] photodimerisation reaction.

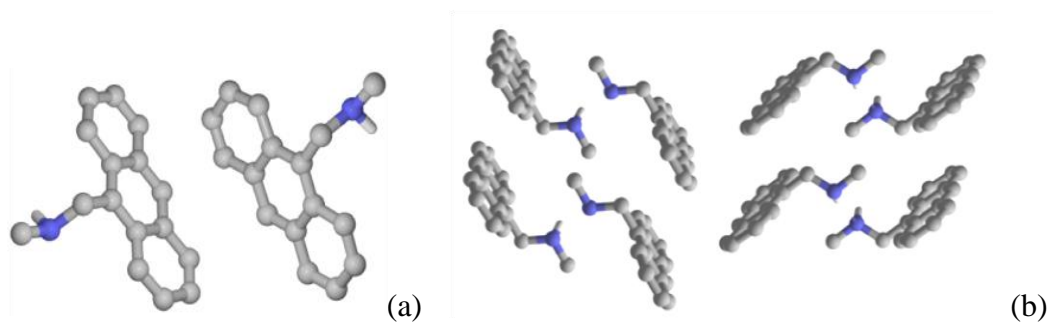


Figure I.2.2. Molecular pairs in crystalline MAMA (a) are arranged in a herringbone pattern (b).

H_{CH} are omitted for clarity.

Coordination compounds

Solid state photodimerisation of MAMA is dependent on the correct alignment of molecules in the crystal packing. In order to observe photodimerisation of MAMA in the solid state, we have used three silver salts in combination with MAMA, to arrange the possible reactive molecules in the crystal packing by using an intermolecular design strategy.

From the reactions between the ligand MAMA and the metal salts, conducted in solution, three complexes have been obtained: $[\text{Ag}(\text{MAMA})_2][\text{PF}_6]$, $[\text{Ag}(\text{MAMA})_2][\text{BF}_4]$ and $[\text{Ag}(\text{MAMA})_2][\text{Ag}(\text{NO}_3)_2]$. The complexes were obtained regardless of the starting stoichiometric ratio used for the reagents (2:1 or 1:1). A mechanochemical approach has also been used, but no profitable results have been obtained. (see Figures I.2.3 and I.2.4, the atoms of silver in the following figures are reported in a large size for clarity).

Complexes $[\text{Ag}(\text{MAMA})_2][\text{PF}_6]$ and $[\text{Ag}(\text{MAMA})_2][\text{BF}_4]$ are isostructural and isomorphous. They both crystallise into the monoclinic $C2/c$ space group and have similar unit cell constants (Table A.4), while the case of $[\text{Ag}(\text{MAMA})_2][\text{Ag}(\text{NO}_3)_2]$ is different from the other two. It also crystallises into the monoclinic space group $C2/c$, however it has shown different arrangements in the crystal packing.

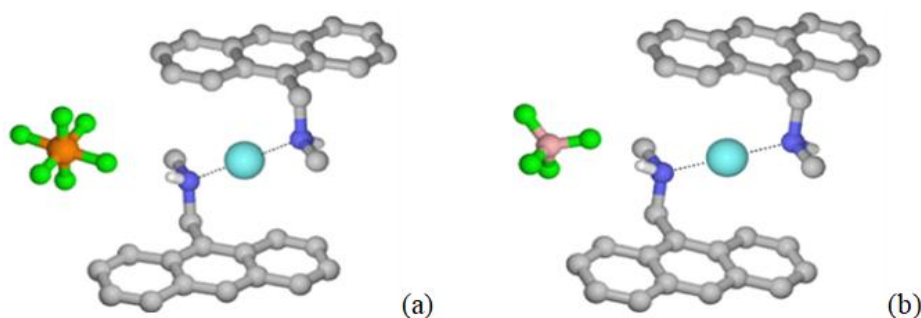


Figure II.2.3. $[\text{Ag}(\text{MAMA})_2]^+$ cation unit and the first coordination sphere around the Ag^+ ion (cyan), in the complexes of (a) $[\text{Ag}(\text{MAMA})_2][\text{PF}_6]$ and (b) $[\text{Ag}(\text{MAMA})_2][\text{BF}_4]$. H_{CH} omitted for clarity.

In both the hexafluorophosphate and tetrafluoroborate salts the $[\text{Ag}(\text{MAMA})_2]^+$ complex is a 0D structure, consisting of two MAMA molecules coordinated to silver(I) in a linear fashion [$\text{N}\cdots\text{Ag}^+$ 2.165(1) and 2.177(1) Å for $[\text{Ag}(\text{MAMA})_2][\text{PF}_6]$ and $[\text{Ag}(\text{MAMA})_2][\text{BF}_4]$, respectively]; $\text{N}-\text{Ag}-\text{N} = 180^\circ$, with the silver cation on a crystallographic centre of inversion] (see Figure II.2.3). In crystalline $[\text{Ag}(\text{MAMA})_2][\text{Ag}(\text{NO}_3)_2]$, while the cation remains the same [$\text{N}\cdots\text{Ag}^+ = 2.178(1)$ Å], the

counterion is now a second silver(I) complex, formed by the coordination of two nitrate anions to silver(I) via two oxygen atoms per NO_3^- unit [$\text{O}\cdots\text{Ag}^+ = 2.447(1) \text{ \AA}$, see Figure II.2.4]. The silver ion belonging to the anionic complex also participates in $\text{Ag}^+\cdots\pi$ interactions [$\eta^1 = 2.712(1) \text{ \AA}$] with the aromatic rings on neighboring cations²⁴, thus resulting in the formation of a 1D coordination polymer (see Figure II.2.4) extending along the c -axis direction.

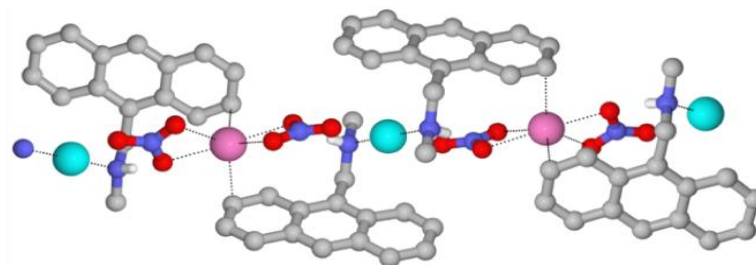
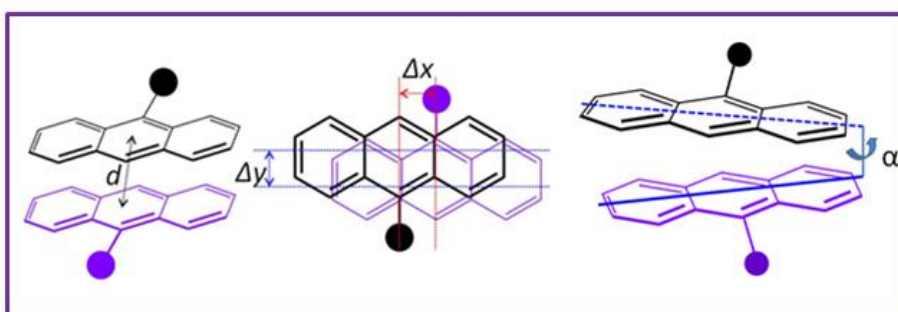


Figure I.2.4. $[\text{Ag}(\text{MAMA})_2]^+$ cationic unit of the first coordination around the Ag^+ ion (cyan) and the second Ag^+ ion (pink), present in the $[\text{Ag}(\text{MAMA})_2][\text{Ag}(\text{NO}_3)_2]$ coordination polymer. H_{CH} omitted for clarity.

I.2.2.2 UV irradiation

In the Scheme I.2.3, the general criteria used for the evaluation of the solid state photodimerisation of molecules are reported. The geometric parameters to be considered are the following: i) d = centroids separation between adjacent molecules (upper limit = 4.2 \AA); ii) α = twisting angle between long molecular axis; iii) Δy and Δx = transversal and longitudinal offset. In Table I.2.1, the measured values of the geometrical parameters for each of the compounds studied in this work are reported.



Scheme I.2.3. Geometrical parameters used to evaluate the potential solid state photoreactivity of MAMA complexes of silver (I).

Table I.2.1. Geometrical parameters used for the evaluation of the solid state photoreactivity.

	d (Å)	α (°)	Δy (Å)	Δx (Å)
MAMA	5.481(9)	0	3.406(9)	2.262(2)
[Ag(MAMA)₂]PF₆	3.701(1)	0	1.083(3)	0.954(1)
[Ag(MAMA)₂]BF₄	3.691(1)	0	1.332(4)	0.211(1)
[Ag(MAMA)₂][Ag(NO₃)₂]	3.819(9)	0	0.801(1)	1.563(2)

Since no suitable single crystals of pure MAMA were obtained, it was irradiated in ethanol solution and as polycrystalline powder.

Irradiation of complexes under UV light was first performed on the single crystal samples used for structure determination, and then on the polycrystalline compounds. Single crystal X-ray data collections after irradiation were impossible to perform due to the disintegration of the crystals under irradiation, while the photoreactivity on polycrystalline samples was tested by means of XRPD and Raman spectroscopy.

MAMA

MAMA was irradiated both in solution and in the solid state with UV light at $\lambda = 365\text{nm}$. From the irradiation of the ethanol solution of MAMA, a crystalline product, in the form of the dimer have been obtained and structurally characterised by means of X-ray diffraction (DMAMA, see Figure I.2.5).

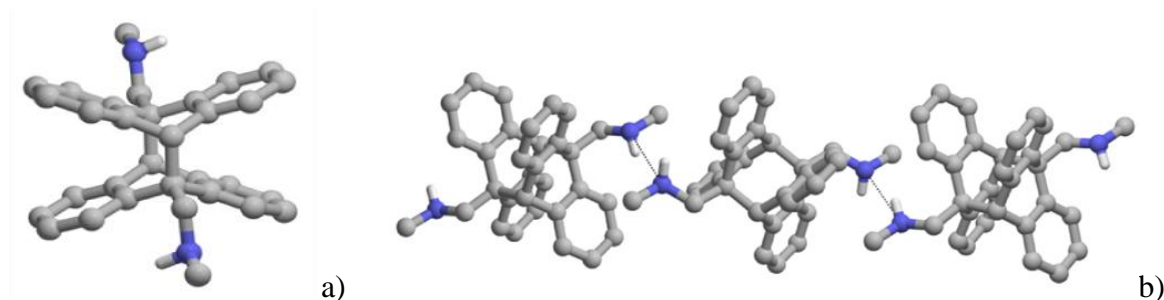


Figure I.2.5. (a) Crystal structure of the photoproduct of the reaction conducted in solution (DMAMA) and b) hydrogen bonding network. H_{CH} are omitted for clarity.

The irradiation of MAMA was also performed on polycrystalline powder, but no photoreaction was observed because of the unfavourable orientation of the molecules within its crystal packing (see Figure I.2.2). In the crystal structure of MAMA, the closest anthracene monomers observed, with a parallel alignment of the π -systems, are quite distant and the herring-bone motif does not favour the photodimerisation. (see Table I.2.1).

Comparing the structure of the dimer (Figure I.2.5) and that of MAMA (Figure I.2.2), we can observe the same pairing of molecules, but the N(H)⋯N separation is much larger in the crystal structure of MAMA [$N\cdots N = 3.321(1) \text{ \AA}$].

Figure I.2.6 shows the powder patterns of the polycrystalline compound of MAMA, recorded before and after the UV irradiation, which remain unvaried. The absence of changes in the diffraction pattern after the irradiation confirms that the compound is photostable.

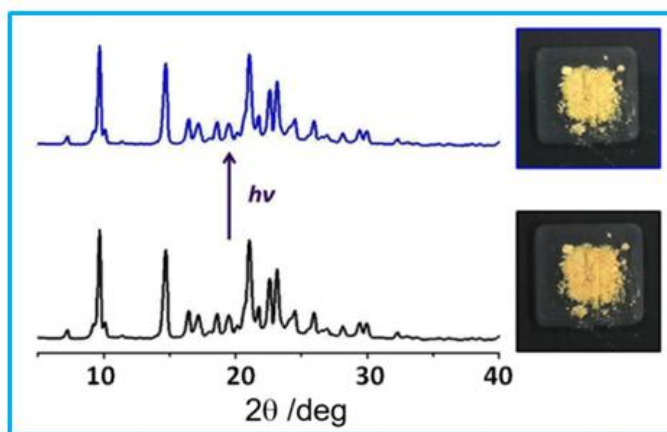


Fig. I.2.6. Powder X-ray diffraction patterns recorded before and after UV irradiation at $\lambda = 365\text{nm}$ for polycrystalline samples of pure MAMA.

With the intention to obtain crystals of the dimer of MAMA we have also tried to irradiate MAMA in a medium essentially half-way between solution and the solid state: a gel. We used a bis-urea derivative low molecular weight gelator (LMWG), as medium for the photoreaction of MAMA.

The reason we have chosen to use the gel medium is that it was really useful for the photoreaction of anthracene: the anthracene molecules were incorporated into the gel medium and then the gel was irradiated with UV light. Anthracene was dissolved in toluene, in a little vial with also 1 wt% of the bis(urea) gelator (see Figure I.2.7). The suspension was heated by means of a heat gun and subsequently, a transparent gel was formed upon cooling and it was irradiated overnight with UV light. After irradiation, crystals of the photodimer (dianthracene) have been obtained in the gel and in order to recover the crystals from the gel, an ethanol solution of tetrabutylammonium acetate was used because of its capacity of gel disruption.^{23b} (see Figure I.2.7). Crystals were recovered by filtration and analysed by means of single crystal X-ray diffraction.

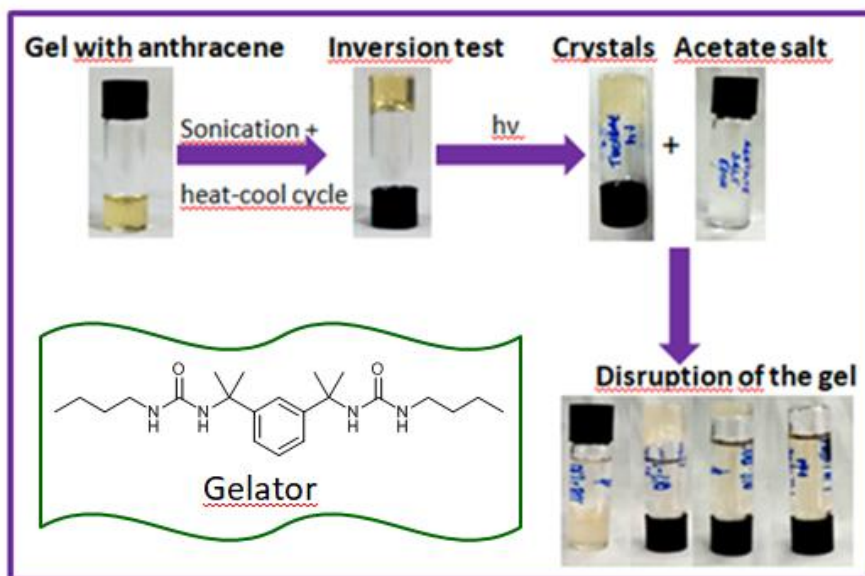


Figure I.2.7. Irradiation of anthracene in gel medium and disruption using an ethanol solution of tetrabutylammonium acetate salt.

Concurrently, we have irradiated a toluene solution of anthracene and by comparison of the crystals obtained from the gel and from the solution, we have observed some differences in term of size and morphology. We observed that crystals of the dimer grown in the gel medium were much larger than those grown in solution. (see Figure I.2.8 and I.2.9).



Figure I.2.8. Comparison of crystals of the dimer of anthracene obtained after irradiation in solution (left) and in the gel medium (right).

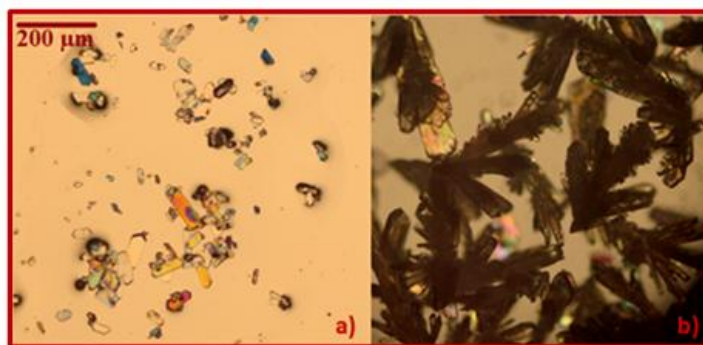


Figure I.2.9. Pictures taken by optical microscope of crystals of dianthracene obtained after irradiation in solution (left) and in the gel medium (right).

However, repeating the same procedure in the case of MAMA, no crystals of the dimer were obtained in the gel.

Coordination compounds

The behaviour of the complexes under irradiation process was similar in each of the three compounds. Figure I.2.10 shows the behaviour of $[\text{Ag}(\text{MAMA})_2][\text{PF}_6]$ under irradiation. In response to the significant pressure, arising from molecular movements during the photoreaction, a crystal disintegration occurred.²⁵

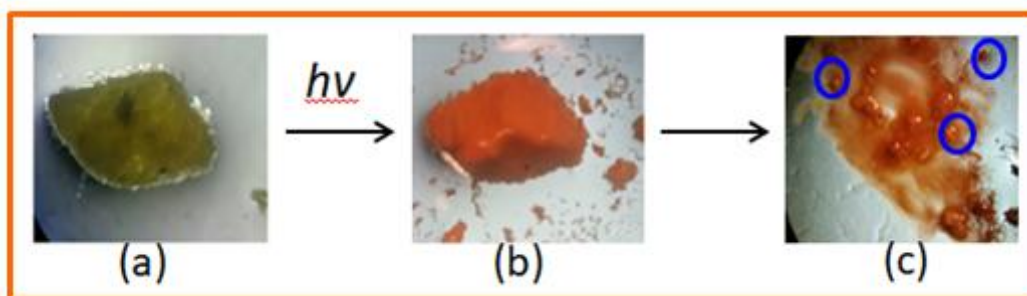


Figure. I.2.10. a) Single crystal of $[\text{Ag}(\text{MAMA})_2][\text{PF}_6]$ used for crystal structure determination and pictures taken, before (a), during (b) and after irradiation (c), by optical microscope. With blue circles are indicated the residual light yellow crystalline fragments identified as starting materials by means of SCXRD.

By irradiation of the polycrystalline material of $[\text{Ag}(\text{MAMA})_2][\text{PF}_6]$, subtle changes were detected (see Figure I.2.11, while for the other two complexes the comparison between the powder patterns, run before and after irradiation, is shown in Figures A.10 and A.11), as is usually expected for those reactions that occur topotactically and imply conservation of symmetry²⁶ and consequently an unmarked alteration of the powder pattern. It can be

ascribed to an inhomogeneous permeation of UV light into the sample which could have caused the incompleteness of the reaction in all of three coordination compounds.

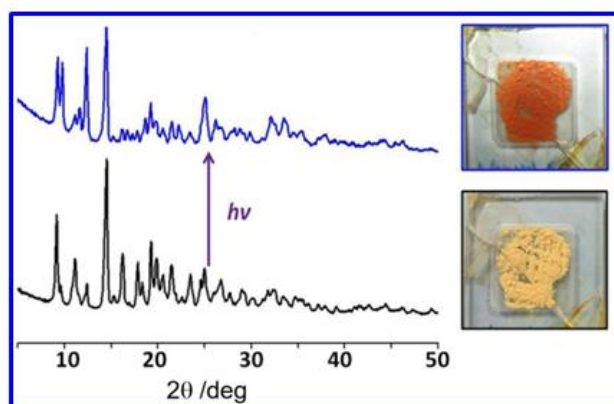


Figure I.2.11. PXRD patterns recorded before and after UV irradiation at $\lambda = 365$ nm for the polycrystalline sample of $[\text{Ag}(\text{MAMA})_2][\text{PF}_6]$.

Studies are in progress to understand the colour change of the compounds (both crystal and powder) during the irradiation process, which might be an indication of a photochromic behaviour²⁷.

It is difficult to evaluate, from the powder patterns, the progression of the reaction occurring in the solid state for the three complexes of MAMA, since no consistent variations in the diffractograms appeared after the irradiation under UV light (see Figures A.10 and A.11).

Isolation of DMAMA

The confirm of the obtained photoreaction was achieved isolating the MAMA in the $[\text{Ag}(\text{MAMA})_2][\text{PF}_6]$ irradiated powder. $[\text{Ag}(\text{MAMA})_2][\text{PF}_6]$ was used because it was the most promising case of the photoreaction studied. The dimer was chemically isolated by treating the irradiated solid of $[\text{Ag}(\text{MAMA})_2][\text{PF}_6]$ with a diluted $\text{HBr}_{(\text{aq})}$ solution in order to remove via filtration the metal ion as AgBr . Crystallisation of the solution via evaporation yielded a few pale yellow single crystals, which were identified, via single crystal X-ray diffraction, as the bromide salt of the photoproduct $[\text{DMAMAH}_2]\text{Br}_2$, see Figure I.2.12.

The crystal structure of $[\text{DMAMAH}_2]\text{Br}_2$ consists in a 2D network of cations and anions held together by charge assisted hydrogen bonds between $[\text{DMAMAH}]^{2+}$ and Br^- $[\text{NH}_2^+ \cdots \text{Br}^- = 3.239(6) - 3.330(6) \text{ \AA}]$.

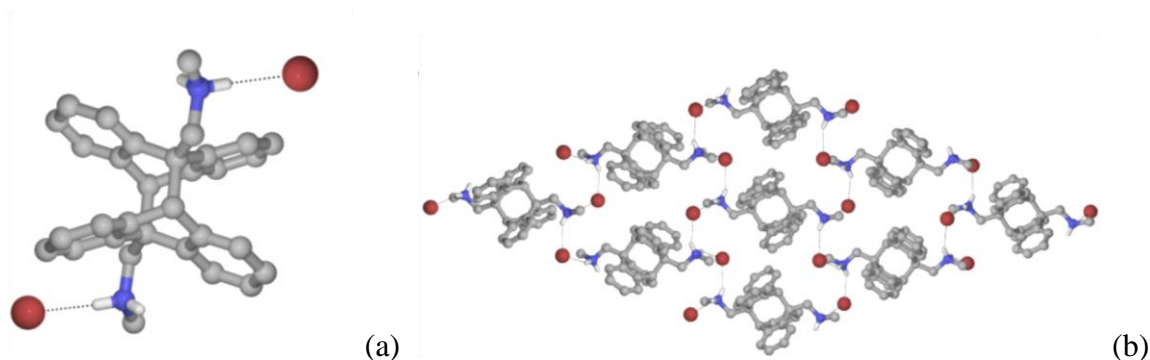


Figure I.2.12. (a) Molecular structure of $[\text{DMAMAH}_2]\text{Br}_2$; (b) 2D hydrogen bonding network formed by $[\text{DMAMAH}_2]^{2+}$ cations and Br^- anions. H_{CH} omitted for clarity.

In order to confirm the photoconversion of the complexes and the solid-state photostability of MAMA, samples have been subjected to RAMAN spectroscopy measurements.

I.2.2.3 Raman spectroscopy

The Raman spectra of MAMA and DMAMA are shown in Figure I.2.13; their main vibrational bands and assignments are reported in Table A.5. Anthracene²⁸ and its 9-substituted derivatives²⁹ have been used as model samples for MAMA since their Raman spectra have been reported here for the first time and no assignments have been reported in the literature for these compounds. In the case of dianthracene³⁰ instead, the photodimers of anthracene derivatives,³¹ 9,10-dihydroanthracene and derivatives³² and as well as *ortho*-xylene³³ have been used as model compounds for DMAMA.

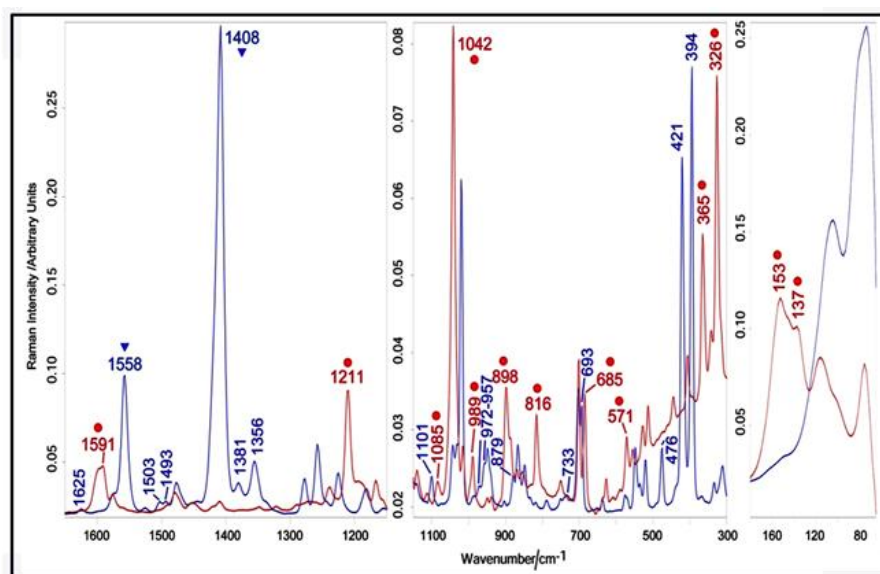


Figure I.2.13. Raman spectra of MAMA (blue) and DMAMA (red). The main bands characteristic of the dimer are indicated with a dot; the strongest bands that disappear or weakening in the dimer are indicated with a triangle.

Many spectral features are characteristic of the dimer; the main of them are indicated with a dot; their wavenumber positions are in agreement with those reported by Ebisuzaki *et al.* for dianthracene,^{29a} (see Table A.5). The main marker bands of the dimerisation process have been identified at 1597-1591, 1085, 1042, 989, 898, 816, 685, 571, 365, 326, 153, 137 cm^{-1} . Passing from MAMA to DMAMA, some bands disappeared or significantly weakened; the strongest were those at 1558 and 1408 cm^{-1} , assignable to aromatic CC ring stretching modes^{28a,f}. The weakening of the band at 1400 cm^{-1} has been used to follow the photodimerisation process of anthracene derivatives³⁴. Several bands precisely assignable to 9-substituted and alkyl-substituted anthracenes (i.e. those at 1625, 1558, 1503 - 1493, 1408, 1381, 1356, 1101, 972 - 957, 879, 733, 693, 476, 421, 394 cm^{-1})^{28e,f 29a,b,c,d 30b} or fused benzene rings (i.e. those at 1408 and 394 cm^{-1})^{29d} were not detected in the Raman spectrum of DMAMA, as predictable (see Table A.5). Regarding the CH out of plane bending region, the component at 879 cm^{-1} , due to the CH group around perpendicular to the longer axis of the molecule (i.e. at the 10 position^{30b}), was no longer observed in the spectrum of DMAMA, since the C-H bond at the 10 position was no more aromatic in this molecule; on the other hand, the 750 cm^{-1} component, due to the CH groups approximately parallel to the longer axis of the molecule^{30b}, did not disappear in the spectrum of DMAMA and became more prominent due to the contribution of the CH out of plane bending of *ortho*-disubstituted benzenes.^{30b}

Figure I.2.14 shows that the dimerisation in the polycrystalline MAMA was not observed, the above identified marker bands of dimerisation were not detected. Only minor changes were observed upon irradiation, ascribable to little molecular rearrangements. No photodegradation of the sample occurred and no production of anthraquinone species was observed; actually, their main marker band at about 1660 cm^{-1} (C=O stretching)^{29d,30c,33} was not detected.

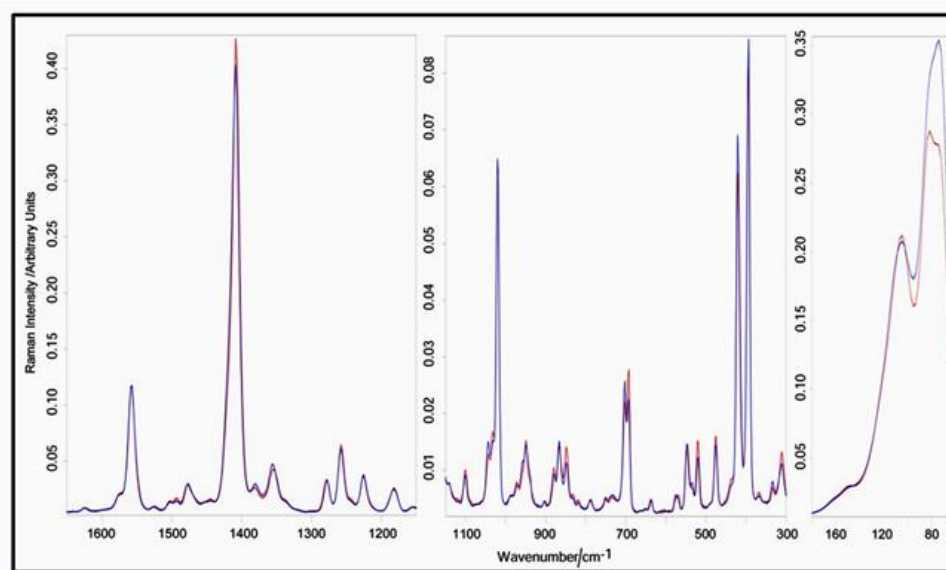


Figure I.2.14. Raman spectra of MAMA before (blue) and after irradiation (red).

In all spectra of the complexes, changes in wavenumber positions and relative intensities of numerous bands assignable to the aromatic system (see Table A.5 for assignments) were observed in the CC stretching ($1630 - 1400 \text{ cm}^{-1}$ range), CH in plane bending ($1400-1000 \text{ cm}^{-1}$ range), CH out of plane ($1000 - 700 \text{ cm}^{-1}$ range) and ring bending and torsion modes (below 700 cm^{-1}). Figures I.2.15 - 17 show the Raman spectra of the $[\text{Ag}(\text{MAMA})_2][\text{BF}_4]$, $[\text{Ag}(\text{MAMA})_2][\text{PF}_6]$ and $[\text{Ag}(\text{MAMA})_2][\text{Ag}(\text{NO}_3)_2]$ complexes, respectively, before and after irradiation: the spectra of the irradiated samples showed the bands of the unirradiated ones together with the marker bands of dimerisation, with decreasing relative intensity going from $[\text{Ag}(\text{MAMA})_2][\text{PF}_6]$ to $[\text{Ag}(\text{MAMA})_2][\text{BF}_4]$ and $[\text{Ag}(\text{MAMA})_2][\text{Ag}(\text{NO}_3)_2]$. In the spectra of all the irradiated complexes, the aromatic CC stretching band at about 1410 cm^{-1} appeared decreased in intensity with respect to the corresponding spectra recorded before irradiation.

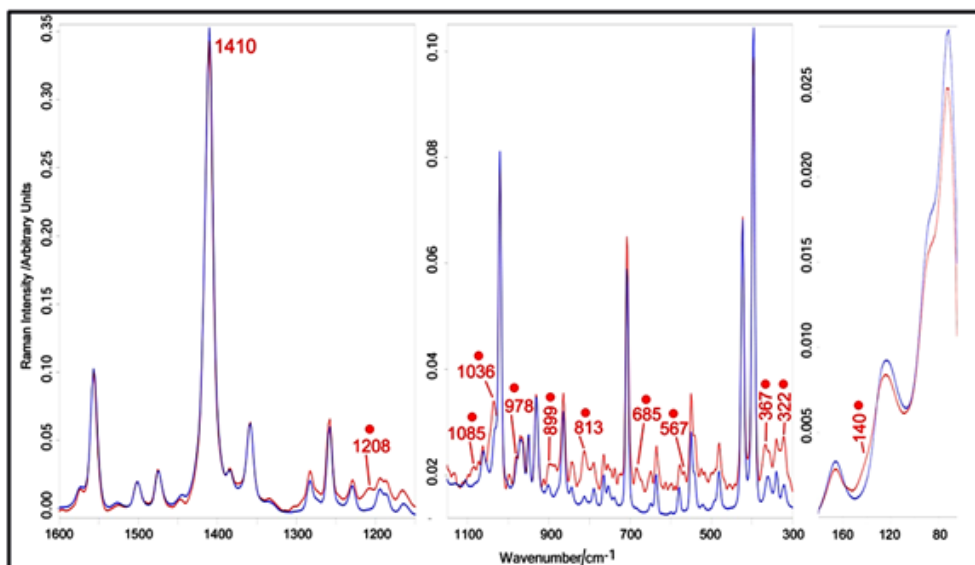


Figure I.2.15. Raman spectra of [Ag(MAMA)₂][BF₄] before (blue) and after irradiation (red). The marker bands of the occurred dimerisation are indicated with a dot.

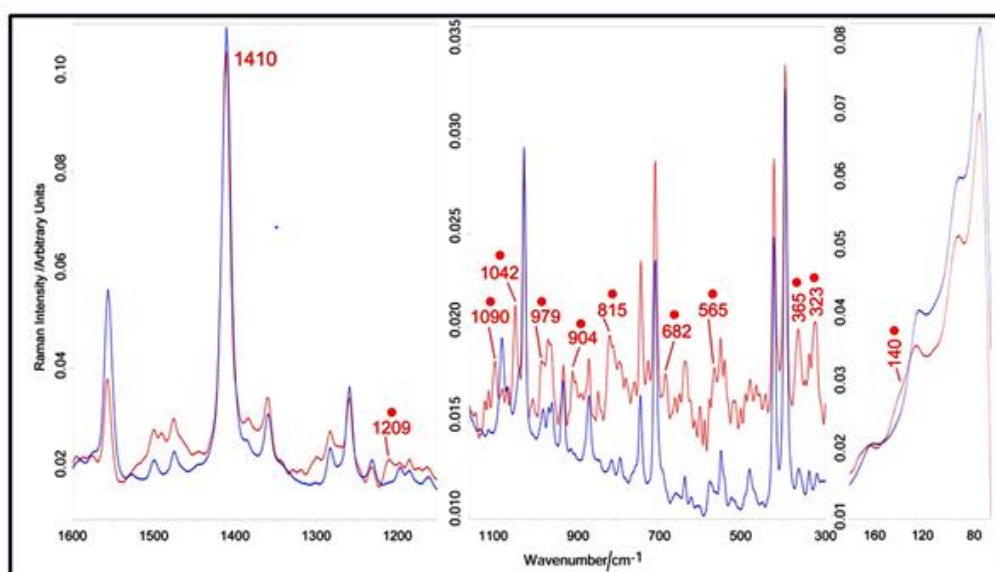


Figure I.2.16. Raman spectra of [Ag(MAMA)₂][PF₆] before (blue) and after irradiation (red). The marker bands of the occurred dimerisation are indicated with a dot.

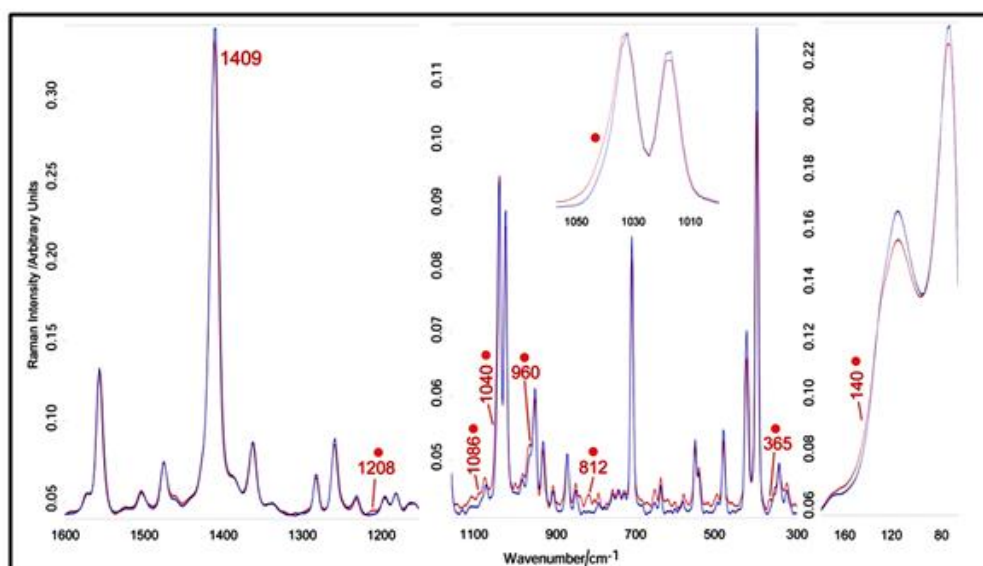


Figure I.2.17. Raman spectra of $[\text{Ag}(\text{MAMA})_2][\text{Ag}(\text{NO}_3)_2]$ before (blue) and after irradiation (red). The marker bands of the occurred dimerisation are indicated with a dot.

I.2.3 Conclusions

We have investigated the [4+4] photoreactivity of: i) MAMA, both in solution and in the solid state and ii) three of its silver complexes. Upon irradiation of an ethanol solution of MAMA, the growth of crystals suitable for X-ray diffraction structure determination was observed. Crystals corresponded to the head-to-tail photodimer of MAMA (DMAMA). However, no photoreaction was detected on a polycrystalline sample of MAMA. The solid-state photostability was rationalized on the basis of the crystal structure, solved from X-ray powder data, which highlights a herringbone packing of MAMA within the crystal. The solid state photostability of MAMA was also confirmed by PXRD and Raman spectroscopy measurements.

The three complexes of MAMA have been prepared from reaction between MAMA and three silver salts, i.e. AgPF_6 , AgBF_4 , and AgNO_3 . Two novel complexes $[\text{Ag}(\text{MAMA})_2][\text{PF}_6]$, $[\text{Ag}(\text{MAMA})_2][\text{BF}_4]$ and the 1D coordination polymer $[\text{Ag}(\text{MAMA})_2][\text{Ag}(\text{NO}_3)_2]$ have been obtained and characterised by means of X-ray diffraction techniques. In all three complexes, the structural determination from SCXRD has shown a proper double bonds alignment of the anthracene-based ligands suitable for a solid-state [4+4] photoreaction. The three complexes have been tested, firstly, on single crystal samples which evidenced complete degradation into polycrystalline powders under irradiation and then on polycrystalline samples. The disintegration phenomenon can be described as a response to the tremendous pressure, arising from the movements generated

within the crystals during the photoreaction. The behaviour of the UV irradiation on polycrystalline samples was investigated by means of PXRD and Raman spectroscopy. Raman spectroscopy was very useful as complementary technique to investigate on the solid state photoreactivity, which were not clearly defined by means of XRPD.

Finally, we have had a structural crystallographic evidence of the formation of the [4+4] photoproduct in the irradiated $[\text{Ag}(\text{MAMA})_2][\text{PF}_6]$ sample. $[\text{Ag}(\text{MAMA})_2][\text{PF}_6]$ was the best candidate in terms of photoreaction. It was treated with a diluted solution of HBr and as a result few crystals of the photoproduct were formed, structurally characterised and identified as $[\text{DMAMA}(\text{H}_2)]\text{Br}_2$.

I.2.4 Experimental section

All reactants were purchased from Sigma-Aldrich and used as received. Reagent grade solvents and bidistilled water were used.

Synthesis of trans-Bis-9-methylamminomethyl-9,10-dihydro-9,10-anthracenediyl (DMAMA):

A saturated solution of MAMA was obtained by dissolution of 100 mg of MAMA in 8 mL of ethanol. The undissolved powder was filtered from the solution, with a 2 μm pore size filter; and the solution was irradiated, at $\lambda = 365 \text{ nm}$, in a quartz cuvette for 24 hours. Yellow crystals appeared after the irradiation process and were recovered by filtration on a paper filter, affording ca. 40 mg of a compound which was identified as trans-bis-9-methylamminomethyl-9,10-dihydro-9,10-anthracenediyl (DMAMA).

Synthesis of complexes $[\text{Ag}(\text{MAMA})_2][\text{PF}_6]$, $[\text{Ag}(\text{MAMA})_2][\text{BF}_4]$ and $[\text{Ag}(\text{MAMA})_2][\text{Ag}(\text{NO}_3)_2]$:

100 mg (0.47 mmol) of ligand MAMA were dissolved in 10 mL of ethanol. An equivalent amount of the respective silver salt (AgX , where $\text{X}^- = \text{PF}_6^-$, BF_4^- or NO_3^-) was dissolved in EtOH (4 mL) and the solution obtained was added to the first one under stirring. A yellow solid precipitated was obtained in all cases after 15 minutes and the suspensions were kept under stirring for 24 h. The polycrystalline powders obtained, were collected by vacuum filtration and washed with EtOH. Single crystals suitable for X-ray diffraction analysis were grown by triple layer liquid diffusion: a solution of MAMA in ethanol was placed at the bottom of an NMR test tube, and on this were deposited a second layer of pure ethanol, followed by an ethanol solution of the silver salt. The identity of the obtained polycrystalline materials and single crystals was verified by comparing experimental and simulated powder diffraction patterns (see Figure A.9).

Structural characterisation

Single crystal X-ray diffraction: Single-crystal data for all complexes were collected at RT on an Oxford X'Calibur S CCD diffractometer equipped with a graphite monochromator (Mo-K α radiation, $\lambda = 0.71073\text{\AA}$). Though, single crystals of the trans-Bis-9-methylamminomethyl-9,10-dihydro-9,10-anthracenediyl (DMAMA) were collected on a Bruker D8Venture diffractometer (PHOTON-100 CMOS_detector, I μ S-microsource, focusing mirrors, Mo-K α , $\lambda = 0.71073\text{\AA}$) and processed using Bruker APEX-II software. Data collection and refinement details are listed in Table A.4. H_{CH} atoms for all complexes were added in calculated positions and refined riding on their respective carbon atoms; H_{NH} atoms were either directly located or, when not possible, added in calculated positions. Non-hydrogen atoms were refined anisotropically. SHELX97¹⁵ was used for structure solution and refinement on F². The program Mercury¹⁶ was used to calculate intermolecular interactions. CYLview¹⁷ and Mercury¹⁶ were used for molecular graphics.

Structure solution and refinement from powder data: MAMA was structurally characterised by means of powder diffraction solution after a recrystallisation from melt. Powder diffraction data were collected in the 2 θ range 3 - 70° (step size, 0.013°; time/step, 172s; 0.02 rad s⁻¹; V x A 40 x 40) on a Panalytical X'Pert PRO automated diffractometer operated in transmission mode (capillary spinner) and equipped with a Pixel detector. Three patterns were recorded and summed in order to enhance the signal to noise ratio. Powder diffraction data were analysed with the software EXPO2014,³⁶ which is designed to analyse both monochromatic and non-monochromatic data. Peaks were automatically chosen in the 2 θ range 5–50°, and a triclinic cell was found (Table A.4), using the algorithm N-TREOR¹⁹. The structure was solved using a simulated and annealing method and refined as a rigid body by Rietveld method with the software TOPAS 4.1.²¹ A spherical harmonics model was used to describe the preferred orientation. A rigid body was applied on the two fragments. An overall thermal parameter for the C, N, O atoms was adopted.

Powder diffraction measurements: For phase identification purposes X-ray powder diffractograms in the 2 θ range 5-80° (step size, 0.02°; time/step, 20 s; 0.04 rad s⁻¹; 40mA x 40kV) were collected on a Panalytical X'Pert PRO automated diffractometer equipped with an X'Celerator detector and in Bragg-Brentano geometry, using Cu K α radiation without a monochromator. The program Mercury¹⁶ was used for simulation of X-ray powder patterns on the basis of single crystal data. Chemical and structural identity

between bulk materials and single crystals was always verified by comparing experimental and simulated powder diffraction patterns (see Figure A.9).

Irradiation: In all cases, irradiation was performed using a UV-LED (*Led Engin LZI-10UV00-0000*) at $\lambda = 365$ nm. A saturated ethanol solution of 9-(methylaminomethyl)anthracene (MAMA) was placed in a quartz cuvette and irradiated using two UV-LED placed at a distance of 2 cm from the cuvette. Single crystal samples of the complexes were instead irradiated using the UV-LED placed at a distance of 1 cm. Powder samples were placed onto a flat sample holder and irradiated using the LED placed at a distance of 2 cm.

Raman spectroscopy: Raman spectra were recorded on a Bruker MultiRam FT-Raman spectrometer equipped with a cooled Ge-diode detector. The excitation source was an Nd³⁺-YAG laser ($\lambda = 1064$ nm) in the backscattering (180°) configuration. The focused laser beam diameter was about 100 μm and the spectral resolution 4 cm^{-1} . Laser power at the sample was about 30 mW for unirradiated samples and irradiated MAMA and 1 mW for the irradiated complexes due to the high fluorescence background. The spectra of the latter samples were baseline corrected. Under these conditions, no photodegradation of the samples was detected.

I.3 References

1. (a) G. R. Desiraju, *Organic solid state chemistry*, Amsterdam; New York : Elsevier, **1987**; (b) M. D. Cohen, G. M. Schmidt, *J. Chem. Soc.*, **1964**, 1996; (c) G. Kaupp, in *Making Crystals by Design*, D. Braga, F. Grepioni, WILEY-VCH, Weinheim, **2006**, 87–148; (d) K. Biradha, R. Santra, *Chem. Soc. Rev.*, **2013**, 42, 950-967.
2. F. Toda, *Organic Solis State Reactions*, **2005**, Springer-Verlag Berlin Heidelberg.
3. D. Braga, F. Grepioni, *Making Crystal by Design: Methods, Techniques and Applications*, Wiley-VCH, Weinheim, **2007**.
4. L. Addadi,; M. Lahav, *J. Am. Chem. Soc.*, **1978**, 100, 2838-2844.
5. G. M. J. Schmidt, *J. Chem. Soc.*, **1964**, 2014-2021.
6. G. M. J. Schmidt, *Pure Appl. Chem.*, **1971**, 27, 647-678.
7. (a) Heiko Ihmels, Dirk Leusser, Matthias Pfeiffer and Dietmar Stalke, *Tetrahedron*, **2000**, 56, 6867-6875; (b) M. Horiguchi, Y. Ito, *J. Org. Chem.*, **2006**, 71, 3608-3611.
8. (a) L. R. MacGillivray, J. L. Reid, J. A. Ripmeester, *J. Am. Chem. Soc.*, **2000**, 122, 7817-7818; (b) M. Sinnwell, L. R. MacGillivray, *Angew. Chem. Int. Ed.*, **2016**, 55,

- 3477-3480. (c) D. P. Ericson, Z. P. Zurfluh-Cunningham, R.H. Groeneman, E. Elacqua, E.W. Reinheimer, B. C. Noll, L. R. MacGillivray, *Cryst. Growth Des.*, **2015**, 15, 5744-5748.
9. E. C. Constable, G. Zhang, C. E. Housecroft, J. A. Zampese, *Dalton Trans.*, **2011**, 40, 12146-12152.
10. S. d'Agostino, F. Spinelli, E. Boanini, D. Braga, F. Grepioni, *Chem. Comm.*, **2016**, 52, 1899-1902.
11. I. Turowska-Tyrk, E. Trzop, *Acta Cryst.*, **2003**, B59, 779-786.
12. The work was done in collaboration with Prof. Elisa Boanini, from the University of Bologna, for the Scanning Electron Microscope measurements.
13. S. Y. Yang, P. Naumov, S.Fukuzumi, *J. Am. Che. Soc.*, **2009**, 131, 7247-7249.
14. (a) Z. Wang, K. Randazzo, X. Hou, J. Simpson, J. Struppe, A. Ugrinov, B. Kastern, E. Wysocki, Q. R. Chu, *Macromolecules*, **2015**, 48, 2894-2900; (b) Z. Wang, B. Kastern, K. Randazzo, A. Ugrinov, J. Butz, D. W. Seals, M. P. Sibi, Q. R. Chu, *Green Chem.*, **2015**, 17, 4720-4724.
15. Sheldrick, G. M. SHELX97, Program for Crystal Structure Determination; University of Göttingen: Göttingen, Germany, **1997**.
16. C. F. Macrae, I. J. Bruno, J. A. Chisholm, P. R. Edgington, P. McCabe, E. Pidcock, L. Rodriguez-Monge, R. Taylor, J. van de Streek, P. A. Wood, *J. Appl. Crystallogr.*, **2008**, 41, 466-470.
17. C. Y. Legault, CYLview, Université de Sherbrooke, **2009**.
18. A. Altomare, M. Camalli, C. Cuocci and R. Rizzi, *J. Appl. Crystallogr.*, **2009**, 42, 1197-1202.
19. A. Altomare, C. Giacovazzo, A. Molinterni, R. Rizzi, *J. Appl. Crystallogr.*, **2001**, 34, 704-709.
20. Avogadro: an open-source molecular builder and visualisation tool. M. D. Hanwell, D. E. Curtis, D. C. Lonie, T. Vandermeersch, E. Zurek, G. R. Hutchison, *J. Cheminf*, **2012**, 4-17.
21. A. Cohelo, TOPAS-Academic, Coelho Software, Brisbane, Australia, **2007**.
22. This work was realized in collaboration with Prof. Jonathan W. Steed, Christopher D. Jones and Dmitry S. Yufit from the University of Durham, and Prof. Paola Taddei from the University of Bologna (Raman measurements), manuscript in preparation.

23. (a) J. A. Foster, R. M. Edkins, G. J. Cameron, N. Colgin, K. Fucke, S. Ridgeway, A. G. Crawford, T. B. Marder, A. Beeby, S. L. Cobb, J. W. Steed, *Chem. Eur. J.*, **2014**, 20, 279-291; (b) J. A. Foster, M. M. Piepenbrock, G. O. Lloyd, N. Clarke, J. A. K. Howard, J. W. Steed, *Nat. Chem.*, **2010**, 2, 1037-1043; c) C. D. Jones, J. W. Steed, *Chem. Soc. Rev.*, **2016**, 45, 6546-6596.
24. (a) J. M. Maier, P. Li, J. Hwang, M. D. Smith, K. D. Shimizu, *J. Am. Chem. Soc.*, **2015**, 137, 8014-8017; (b) E. A. Hall Griffith, E. L. Amma, *J. Am. Chem. Soc.*, **1974**, 96, 743-749.
25. (a) G. Kaupp, J. Schmeyers, M. Kato, K. Tanaka, N. Harata, F. Toda, *J. Phys. Org. Chem.*, **2001**, 14, 444; (b) I. Halasz, *Cryst. Growth Des.*, **2010**, 10, 2817; (c) D. K. Bučar, T. D. Hamilton, L. R. MacGillivray, in *Organic Nanostructures*, ed. J. L. Atwood and J. W. Steed, WILEY-VCH, Weinheim, **2008**, 305-315; (d) M. A. Garcia-Garibay, *Angew. Chem. Int. Ed.*, **2007**, 46, 8945-8947; (e) A. Natarajan, B. R. Bhogala, in *Supramolecular Photochemistry*, John Wiley & Sons, Inc., **2011**, 175-228.
26. (a) K. Biradha, R. Santra, *Chem. Soc. Rev.*, **2013**, 42, 950-967; (b) G. Wegner, *Pure Appl. Chem.*, **1977**, 49, 443-454; (c) C. R. Theocharis, W. Jones, Topotactic and topochemical photodimerisation of benzylidenecyclopentanones, in *Organic Solid State Chemistry*, ed. G. R. Desiraju, Elsevier, New York, **1987**, 47-68.
27. D. Bailey, N. Seifi, V. E. Williams, *Dyes Pigm.*, **2011**, 89, 313-318.
28. (a) N. Abasbegović, N. Vukotić, L. Colombo, *J. Chem. Phys.*, **1964**, 41, 2575-2577; (b) J. Räsänen, F. Stenman, E. Penttinen, *Spectrochim. Acta A*, **1973**, 29, 395-403; (c) W. F. Maddams, I. A. M. Royaud, *Spectrochim. Acta A*, **1990**, 46, 309-314; (d) I. López-Tocón, J. C. Otero, J. F. Arenas, J. V. Garcia-Ramos, S. Sanchez-Cortes, *Anal. Chem.*, **2011**, 83, 2518-2525; (e) F. R. Dollish, W. G. Fateley, F. F. Bentley, Wiley-Interscience, Chichester, **1974**; (f) A. Alparone, V. Librando, *Spectrochim. Acta A*, **2012**, 89, 129-136.
29. (a) S. Kou, H. Zhou, G. Tang, R. Li, Y. Zhang, J. Zhao, C. Wei, *Spectrochim. Acta A*, **2012**, 96, 768-775; (b) Y. S. Mary, H. T. Varghese, C. Y. Panicker, T. Thiemann, A. A. Al-Saadi, S. A. Popoola, C. Van Alsenoy, Y. Al Jasem, *Spectrochim. Acta A*, **2015**, 150, 533-542; (c) M. Brigodiot, J. M. Lebas, *Spectrochim. Acta A*, **1971**, 27, 1315-1324; (d) L. H. Colthup, S. E. Daly, Wiberley. *Introduction to Infrared and Raman Spectroscopy*. 3rd Edition, Academic Press, San Diego, **1990**.

30. (a) Y. Ebisuzaki, T. J. Taylor, J. T. Woo, M. Nicol, *Spectrochim. Acta A*, **1977**, 73, 253-264; (b) S. Singh and C. Sandorfy, *Can. J. Chem.*, **1969**, 47, 257-263.
31. L. Opilik, P. Payamyar, J. Szczerbinski, A. P. Schütz, M. Servalli, T. Hungerland, A. Dieter Schlüter, R. Zenobi, *ACS Nano*, **2015**, 9, 4252-4259.
32. (a) M. Brigodiot, J. M. Lebas, *J. Mol. Struct.*, **1976**, 32, 297-309; (b) K. Morris and J. Laane, *J. Mol. Struct.*, **1997**, 413-414, 13-20; (c) Y. S. Mary, T. S. Yamuna, C. Y. Panicker, H. S. Yathirajan, M. S. Siddegowda, A. A. Al-Saadi, C. Van Alsenoy, J. Ahmad, *Spectrochim. Acta A*, **2015**, 135, 652-661.
33. (a) K. S. Pitzer, D. W. Scott, *J. Am. Chem. Soc.*, **1943**, 65, 803-829; (b) F. R. Dollish, W. G. Fateley, F. F. Bentley, *Characteristic Raman frequencies of organic compounds*. Wiley-Interscience, Chichester, **1974**.
34. Y. B. Zheng, J. L. Payton, T. B. Song, B. K. Pathem, Y. Zhao, H. Ma, Y. Yang, L. Jensen, A. K. Y. Jen, P. S. Weiss, *Nano Lett.*, **2012**, 12, 5362-5368.
35. D. S. Cordeiro, P. Corio, *J. Braz. Chem. Soc.*, **2009**, 20, 80-87.
36. A. Altomare, C. Cuocci, C. Giacobozzo, A. Moliterni, R. Rizzi, N. Corriero, A. Falcicchio, *J. Appl. Cryst.*, **2013**, 46, 1231-1235.

CHAPTER II: THERMO- AND PHOTOCROMISM IN ORGANIC CRYSTALS

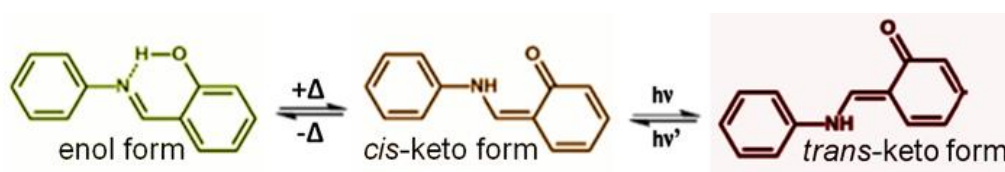
II.1 Introduction

In some molecular systems a variation of temperature or the absorption of electromagnetic radiation may induce colour change phenomena, which are known as thermochromism and photochromism, respectively.¹

N-salicylideneanilines (also called anils) are a well-known class of organic compounds which exhibit thermochromic as well as photochromic behaviour, in both solution and the solid state.² Recently, organic thermo- and photochromic materials have found applications in electronic display systems, optical switching devices, sensors, ophthalmic glasses and so on.³

Thermochromism is a temperature-induced reversible colour change, which is originated from the tautomerism between the phenolic OH and the NH of the imine group of the anils (see Scheme II.1).⁴ Typically, the enol form is uncoloured (or yellowish) and the *cis*-keto form is yellow (or light orange); these two forms are involved in the thermal tautomeric equilibrium.

Photochromism is a light-induced colour change and is due to the photoisomerisation of both the enol and the *cis*-keto form to the *trans*-keto form (see Scheme II.1). The isomerisation process has been reported in the literature as pedal motion since it is similar to pedals movement in a bicycle.⁵

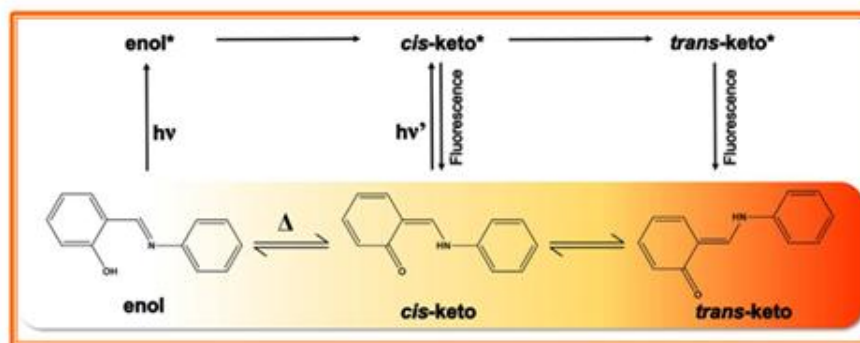


Scheme II.1. Proton transfer (from enol to *cis*-keto forms) and *cis-trans* isomerisation.

In the solid state molecules are restricted in comparison to those in solution or in the gas phase.^{5a} Solid state compounds of anils have been historically divided into two groups, i.e. thermo- and photochromic ones, based on the nature of their crystal packings.⁶ Thermochromism is commonly observed in dense crystal packings whereas photochromism is usually observed for "open" crystal packings. The solid-state evaluation of thermo- and photochromism is made considering the dihedral angles between the

aromatic rings (Φ) in anils. It has been stated that thermochromism is observed when the molecules have a planar conformation i.e. $\Phi < 25^\circ$; whereas photochromism is observed when $\Phi > 25^\circ$.^{5b,7} Thus, in order to observe photochromism, and to allow the pedal motion in the solid state - i.e. the isomerisation process -, the main condition required is to have the indispensable reaction volume within the crystal.^{5a} This is the reason why researchers have decided to categorise anils into two groups (thermo- and photochromic ones) since according to the dihedral angle rules not always the two phenomena - thermo/photochromism - can be simultaneously observed. Nevertheless, there are some exceptions to the empirical rules of the dihedral angles. Recently, some published studies on N-salicylideneanilines and N-salicylideneaminopyridines (as single component systems, and as co-crystals or salts) have reported that also a dense packing can allow photochromism in the solid state;⁸ therefore, thermochromism and photochromism can be observed at the same time since they are not mutually exclusive.^{8a,9} A way to avoid dense packing in the crystallisation process and at the same time to allow photochromism is the use of bulky substituents, i.e. tert-butyl or trityl groups.¹⁰ Crystal engineering may represent an alternative way to organic synthesis to induce photochromic properties keeping the same chromophore molecule, using, for instance, co-crystallisation or salification processes.¹¹ In this light, halogen bond¹² has recently attracted interest in the construction of supramolecular architectures and it can be employed in different fields either in materials science (e.g. supramolecular gelators,¹³ fluorescence-enhancement,¹⁴ phosphorescent materials¹⁵ and supramolecular liquid crystals,¹⁶) and in drug development.¹⁷

Thermochromism is a temperature dependent ground-state keto-enol tautomerisation via an intramolecular proton transfer between the enol form and the *cis*-keto form.¹⁸ The irradiation of these two forms with UV light ($\lambda = 365$ nm for the enol form and $\lambda = 450$ nm for the *cis*-keto form), allows the *cis-trans* photo-isomerisation toward the *trans*-keto form. In the case of excitation of the enol tautomer, the isomerisation takes place through the formation of an excited *cis*-keto intermediate, which is originated from an excited state intramolecular proton transfer (ESIPT), i.e. hydrogen transfer from an excited enol* to produce the excited *cis*-keto* form which lead to the formation of the *trans*-keto form (see Scheme II.2).^{8b,19}



Scheme II.2. Typical processes for thermo- and photochromism in anils, at ground and excited state.

II.2 Investigation of co-crystallisation effects on thermo- and photochromism in the solid state.

This work¹⁹ was focused on the relationship between structural and optical properties of some novel salicylidene aniline derivatives and their corresponding co-crystals. The aim of the work was to understand how some changes in the crystal packing can affect thermo- and photochromic phenomena in the solid state. Three different imines (labelled as **1**,²⁰ **2**²¹ and **3**) of 2-hydroxy-3-methoxybenzaldehyde (i.e. ortho-vanillin) have been synthesised and selected as parent compounds (see Figure II.1). Successively, co-crystallisation was used, as a crystal engineering approach, to co-crystallise the three parent molecules with a halogenated cofomer, 1,2,4,5-tetrafluoro-3,6-diiodobenzene (called **I2F4** for clarity, see Scheme II.3). We have first investigated the differences, in terms of crystal packing, between the parent compounds and their corresponding co-crystals, and then the thermo/photochromic features in all compounds.

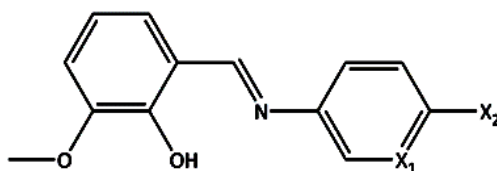


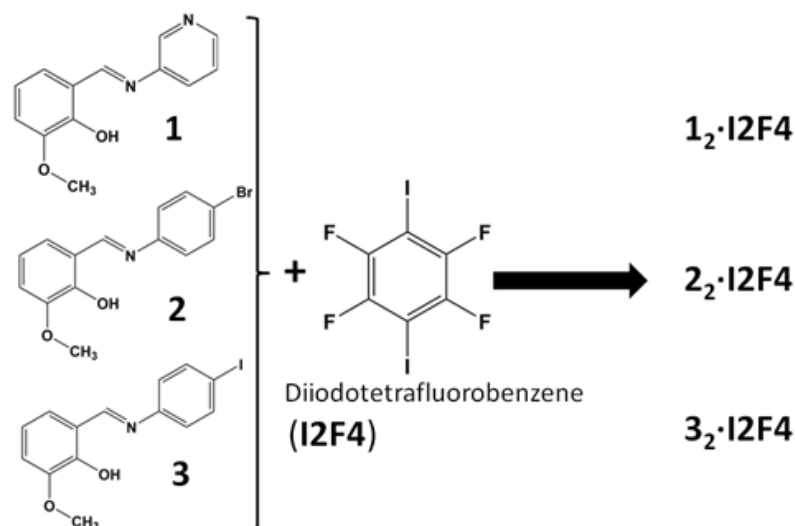
Figure II.1. General structure for the 2-hydroxy-3-methoxybenzaldehyde derivatives **1** ($X_1 = \text{N}$, $X_2 = \text{H}$), **2** ($X_1 = \text{C}$, $X_2 = \text{Br}$) and **3** ($X_1 = \text{C}$, $X_2 = \text{I}$).

All solids, both the parents compounds and their co-crystals, have been synthesised by the group of Prof. Wouters *via* mechanochemistry.^{22,8} In the words of Kaupp “*Mechanochemistry is the branch of solid state chemistry where intramolecular bonds are*

*mechanically broken.*²³ Mechanochemical synthesis, or *mechanochemistry* is a reaction between solid reactants which are activated by grinding.²⁴ The grinding process can be performed manually or mechanically by means of a ball mill, without the use of solvents.²⁵ Thus, mechanochemical reactions are “green” processes since they are solvent-free.²⁶ Sometimes, a few drops of solvent may be added to the solid reagents to facilitate or accelerate the reaction, and in this case the process is called *kneading*²⁷ or *liquid assisted grinding* (LAG).²⁸ The drawback of this process is the characterisation because, in order to know the crystal structure of the product by means of X-ray diffraction, crystals of millimetric size are required. Since solid-state grinding is a particle size reduction technique, usually it is necessary to recrystallise the obtained product, as it is the case for the solid compounds investigated in this work.

All compounds have been investigated by means of: i) single crystal (room and low temperature) and powder X-ray diffraction, ii) solid-state absorption and emission spectroscopy, iii) Fourier-transformed IR spectroscopy and iv) ¹³C and ¹⁵N CPMAS solid-state NMR. Solid-state NMR is a useful technique which can provide evidence of the tautomeric state of a molecule; its approach is based on the analysis of the ¹H, ¹³C and ¹⁵N nuclei.

The chemical shift of the tautomerism depends on the position of both double bonds and protons.²⁹

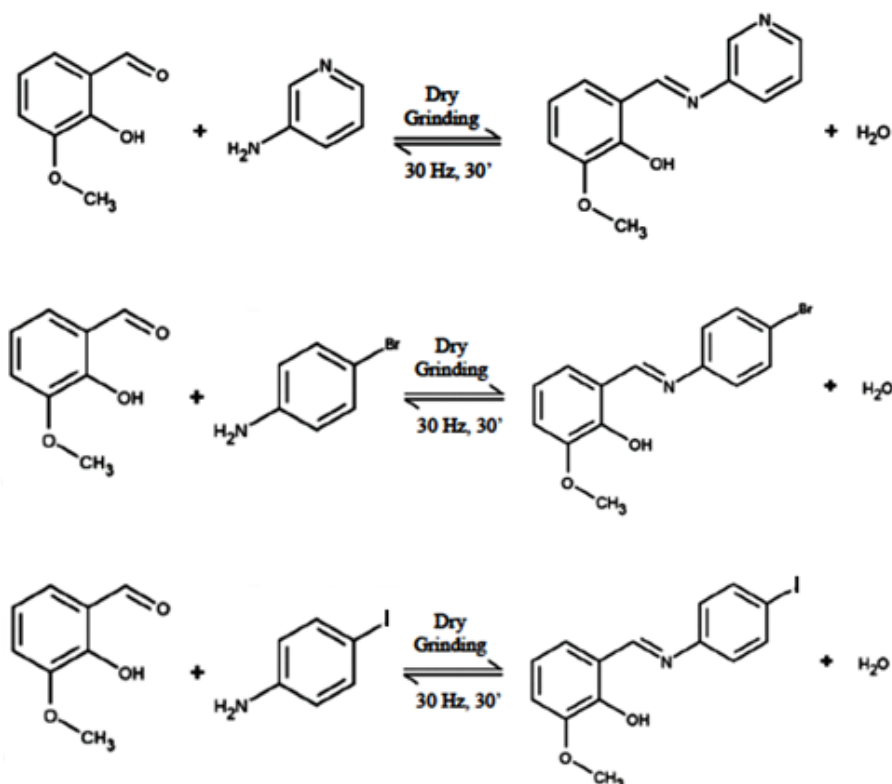


Scheme II.3. Parent compounds (1,2, 3) and their co-crystals with I₂F₄ (1₂·I₂F₄, 2₂·I₂F₄, 3₂·I₂F₄).

Scheme II.3 shows the parent compounds **1**, **2**, and **3**, which belong to different classes of anils, N-salicylide-3-aminopyridines (**1**) and p-halo monosubstituted N-salicylideneanilines (**2** and **3**), and their corresponding co-crystals with **I2F4**. Our expectation was that, in the co-crystallisation process, in the case of **1**·**I2F4** co-crystal, the N-atom of the pyridine moiety of **1** to act as a halogen-bond acceptor for **I2F4** by formation of a $N_{\text{pyridine}} \cdots I$ synthon. In the cases of **2**·**I2F4** and **3**·**I2F4** co-crystals, the halogen-bond interaction with the cofomer is expected to be directed toward the hydroxyl moiety of the chromophore, by a $O_{(\text{hydroxyl})} \cdots I$ synthon, because of the absence of the strong N(pyridine)-atom acceptor.

II.3 Results and discussion

Parent compounds **1**, **2**, and **3** and the corresponding co-crystals with **I2F4** (**1**·**I2F4**, **2**·**I2F4** and **3**·**I2F4**) have been synthesised by mechanochemistry, using a ball mill, without the use of solvents (see Scheme II.4).



Scheme II.4. Mechanochemical reactions for the synthesis of compounds **1**, **2** and **3**.

II.3.1 Crystal structures

For all compounds, bright and colourful crystals of millimetric size, suitable for single crystal X-ray diffraction measurements, were obtained from solution by room temperature, slow solvent evaporation (see Figure II.2).

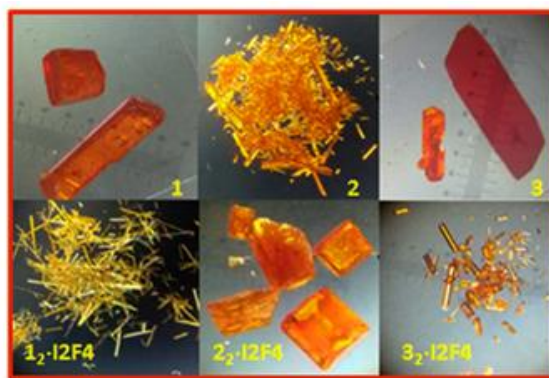
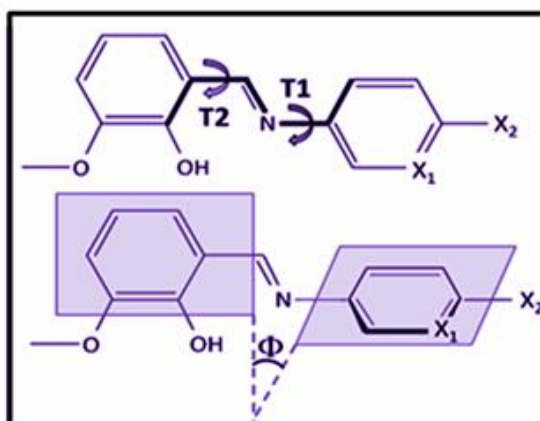


Figure II.2. Crystals of the compound investigated.

An analysis of the torsion angles, **T1** and **T2** (defined in Scheme II.5.), has been performed for the crystal packing of all compounds, **1**, **2** and **3** and of the co-crystalline materials **1₂·I₂F₄**, **2₂·I₂F₄** and **3₂·I₂F₄**, (see Table II.1 for the measured values of **T1** and **T2**).



Scheme II.5. **T1** and **T2** torsion angles in anil derivatives (top) and the Φ dihedral angle between the two aromatic rings (bottom).

Table II.1. Bond distances, torsion angles **T1** and **T2** and dihedral angles Φ .

	N1–C7 (Å)	C6–O1 (Å)	T1 (deg)	T2 (deg)	Φ (deg)
1 (RT)	1.281(3)	1.353(3)	-32.2(3)	1.4(3)	31.4
1 (LT)	1.289(3)	1.357(3)	-32.1(3)	2.0(3)	31.7
2 (RT)	1.281(7)	1.350(6)	12.9(4)	2.8(8)	10.5
2 (LT)	1.291(4)	1.356(3)	12.9(5)	2.4(6)	10.5
3_{solv} (RT)	1.281(7)	1.352(7)	1.1(7)	1.0(8)	2.4
	1.269(6)	1.345(6)	18.1(8)	1.1(8)	20.0
3_{solv} (LT)	1.293(5)	1.359(5)	5.2(5)	1.2(6)	7.8
	1.298(4)	1.364(4)	20.8(5)	0.6(5)	20.4
3A	1.301(11)	1.323(7)	18(1)	2(1)	15.8
3B	1.263(12)	1.352(10)	16(1)	4(2)	14.3
2_{0.7}3_{0.3}	1.310(13)	1.358(11)	18(2)	3(2)	13.4
1₂·I2F4 (RT)	1.282(6)	1.342(4)	153.6(4)	0.8(6)	34.3
1₂·I2F4 (LT)	1.297(9)	1.357(9)	153.6(7)	0(1)	34.8
2₂·I2F4 (RT)	1.268(6)	1.362(6)	36.1(7)	1.9(7)	34.4
2₂·I2F4 (LT)	1.290(5)	1.363(4)	35.4(5)	2.0(5)	33.0
3₂·I2F4 (RT)	1.272(6)	1.358(5)	34.2(6)	2.6(7)	31.3
3₂·I2F4 (RT)	1.291(4)	1.357(4)	31.3(4)	2.0(4)	29.3

Crystal structures of the parent compounds

Compound **1** crystallises in the $P2_12_12_1$ orthorhombic space group. Both at room (RT)³⁰ and low (LT, 108 K) temperature, the observed tautomeric form was the enol form, as supposed from the selected bond lengths between N1–C7 (Å) and C6–O1 (Å) (see Table II.1). The only strong hydrogen bond is of the intramolecular type; it includes the hydroxyl group and the iminic nitrogen and constraints the **T2** torsion angle to the near-planar value of 2.0° (see Table II.1), thus the crystal cohesion is principally due to dispersion forces. A value of the torsion angle **T1** around -32° was observed in both RT and LT determinations. Calculated values of Φ (dihedral angle between aromatic rings), in the RT and LT structures, are 31.4° and 31.7°, respectively. Compound **1** has shown only thermochromic behaviour, even though the value of its dihedral angle suitable to observe photochromism, it was $\Phi > 30^\circ$ (see Figure II.3).^{8a}

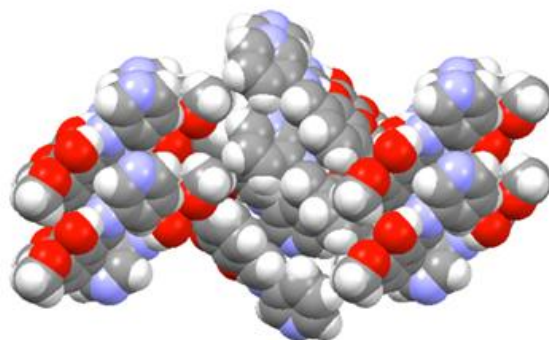


Figure II.3. Crystal structure of compound **1**.

Compound **2** crystallises in the orthorhombic $P2_12_12_1$ space group as well. The observed tautomeric form detected at RT and LT (147 K), is the enol form, as reported above in the case of compound **1**. The **T2** torsion angle is forced to a near-planar value by the hydroxyl group on one side and the iminic nitrogen on the other side. The values for **T1** and Φ are 12.9° and 10.5° , respectively (see Table II.1). By comparison between LT and RT structural determinations, no significant variations (in terms of bond length and torsion angles) have been found. In the crystal packing, a domination of π -stacking is observed, with piles of molecules arranged in a zig-zag manner (see Figure II.4). Compound **2** has shown both thermo- and photochromic behaviour.³¹

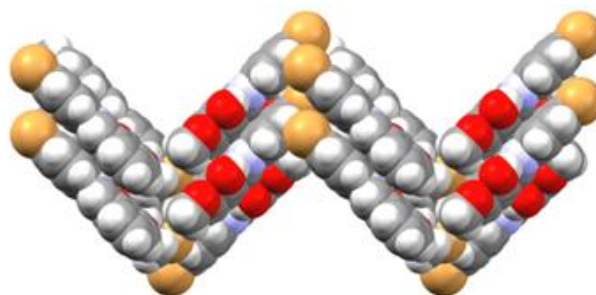


Figure II.4. Crystal structure of compound **2**.

Compound **3** was obtained in three different crystal forms, depending on the solvent used. This fact can be justified by the presence of the iodine atom which could promote the tendency to the formation of multiple forms, since, in the case of compound **2** (which is similar with the exception of an atom of bromine), this phenomenon was not observed. The first obtained compound was named **3A**, it was obtained as orange-red blocks, by slow evaporation from ethanol. It crystallises in the monoclinic $P2_1/c$ space group. In its structure, molecules are affected by positional disorder around a pseudo mirror plane perpendicular to the molecular plane, and near-planar molecules (**T1** ca. 2°) are stacked

along the *c*-axis and then arranged in a zig-zag fashion by a synergy of C–I···I (halogen···halogen interactions) and C–H··· π contacts (see Figure II.5, left).

A second crystal form, named **3B**, was obtained as orange-red prisms by recrystallisation from toluene. It crystallises in the orthorhombic $P2_12_12_1$ space group and it is isomorphous with the compound **2** (see Figure II.5, right).

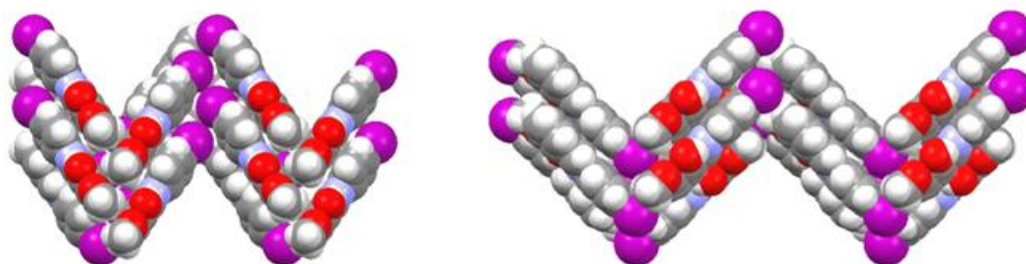


Figure II.5. Crystal structures of compounds **3A** (left) and **3B** (right).

The last compound, **3_{solv}**, was obtained as large orange-red prisms, via slow evaporation from EtOAc. **3_{solv}** crystallises in the triclinic *P*-1 space group with two molecules in the asymmetric unit. In its structure, pairs of molecules interact by π - π stacking in a head-to-tail fashion. Pairs are organized over a layer in a herringbone pattern, in which molecules are held together by C–I··· π contacts. Large voids have been found in its structure (see Figure II.6), they could potentially provide the necessary space in the structure for the *cis-trans* photoisomerisation.

TGA and DSC measurements, performed on **3_{solv}**, have shown a weight loss (ca. 4%) at ca. 50–60 °C and a corresponding endothermic event at 62 °C, respectively. This indicates the presence of crystallisation solvent. The solid of **3_{solv}** is stable up to melting (TDSC = 131 °C), which means that the molecules of **3** are arranged in a strong framework, while the solvent molecules must be distributed in the large cavities within the structure. The amount of solvent could be non-stoichiometric and with a high percentage of empty pores that could be different from crystal to crystal. The low-temperature data collection was not helpful in the detection of solvent within the structure of **3_{solv}**.

In all characterised forms (**3A**, **3B** and **3_{solv}**), molecules have been found in their enol form (see Table II.1). By comparison between LT and RT crystallographic determinations, no consistent variations of bond length and torsion angles have been found.

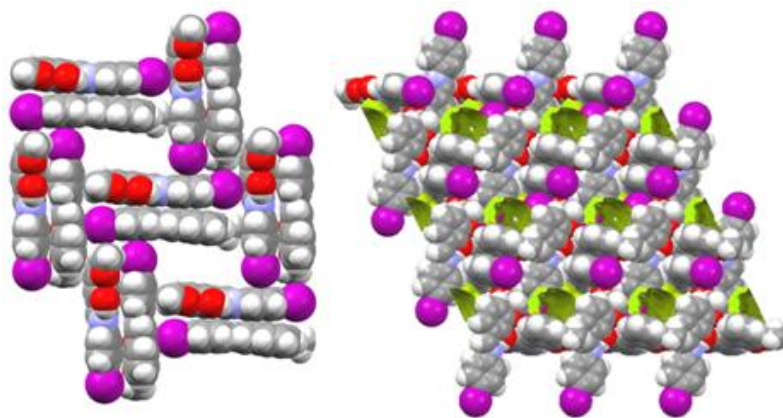


Figure II.6. Crystal structure of compound 3_{solv} .

Compounds **2** and **3B** are isomorphous; they crystallise in the space group $P2_12_12_1$ and differ only for the type of halogen atom (bromine and iodine, respectively). A common characteristic of isomorphous compounds is that they may form solid solutions, in various ranges of composition. We were interested in the possible influence of bromine and iodine on the photochromic behaviour, thus we prepared a solid solution of **2** and **3B**. Regardless of the starting stoichiometric ratio, a larger amount of bromine derivative was invariably found in the product, which corresponded to the formula $2_{0.7}3_{0.3}$. The obtained solid solution $2_{0.7}3_{0.3}$ is isomorphous with the parent compounds (**2** and **3B**, see Table II. 1) with bromine and iodine atoms disordered over the whole crystal.

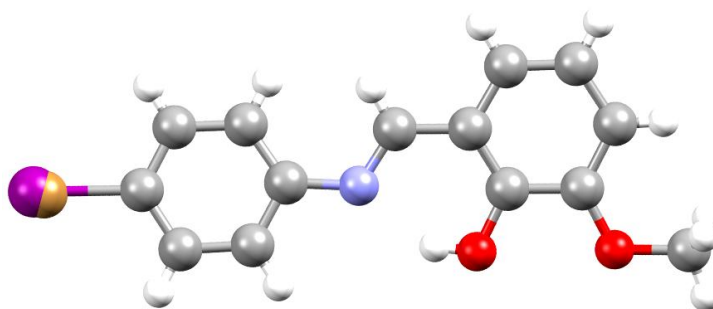


Figure II.7. Representation of the iodine/bromine disorder in the solid solution $2_{0.7}3_{0.3}$.

Crystal structures of the co-crystals with I2F4

Compound $1_2 \cdot \mathbf{I2F4}$ has been obtained upon recrystallisation from EtOAc/cyclohexane, as yellow-orange needles. It crystallises in the monoclinic $P2_1/n$ space group (see Table B.3 in Appendix B for details), with one molecule of **1** and half a molecule of **I2F4** in the asymmetric unit. In its crystal structure, two molecules of **1** are bonded to one molecule of

I2F4 via halogen bonds of the $I \cdots N(\text{pyridine})$ type. Molecules of **1** are stacked along the *a*-axis (see Figure II.8).

The observed tautomeric form, both at RT and LT, is the enol one (see Table II.1). The value of the dihedral angle Φ is around 34.3° and $T1 = 32.8(6)^\circ$. Comparing the torsion angles **T1** and **T2** in crystalline **1** and the corresponding co-crystal **1₂·I2F4**, no variations in terms of shape of compound **1** molecules are detected.

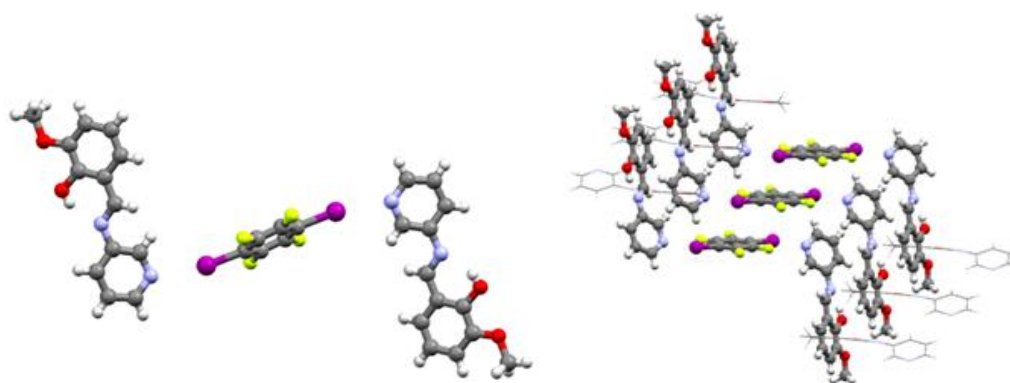


Figure II.8. Crystal structure of compound **1₂·I2F4**.

Co-crystal **2₂·I2F4** has been obtained as orange prisms, after recrystallisation from EtOAc/cyclohexane. It crystallises in the monoclinic $P2_1/n$ space group. Similarly to the previous compounds, the observed tautomeric form is the enol form (both at RT and LT). The **T2** torsion angle is near-planar and the **T1** torsion is $36.1(7)^\circ$ at RT and of 35.4° at LT; whereas the measured values of Φ are: 34.4° (RT) and 33.0° (LT). The crystal structure can be described by a layered network in which molecules interact edge-to-face. The interlayer forces are principally due to edge-to-face stacking between molecules of **2** and of **I2F4**, which is involved in a mixed-stacking with the salicylidene moiety of **2** (Figure II.9). In its structure is also possible to observe directional interactions of the $I \cdots O(\text{hydroxyl})$ type (structure parameters are provided in Table B.4, see Appendix B).

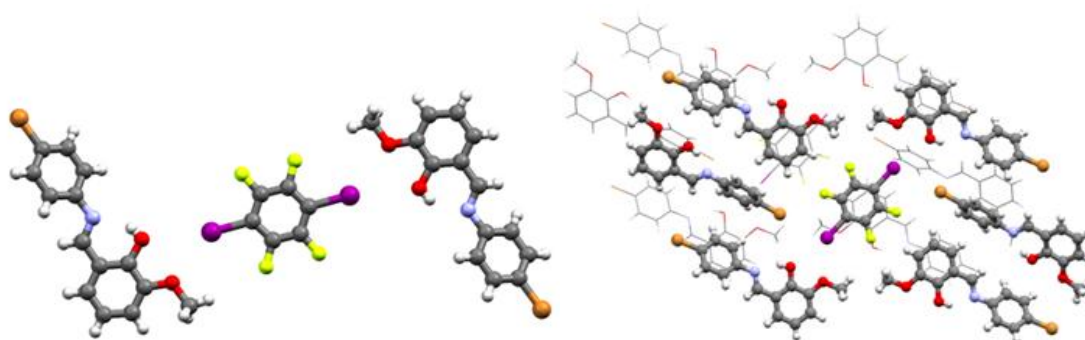


Figure II.9. Crystal structure of **2₂·I2F4**.

Compound **3₂·I2F4**, has been obtained, as orange prisms, after recrystallisation by slow evaporation of EtOAc/cyclohexane. It crystallises in the monoclinic $P2_1/n$ space group and is isostructural with **2₂·I2F4** (see Figure II.10). The enol form is, even in this case, the observed tautomeric form (both at RT and LT) (see Table II.1).

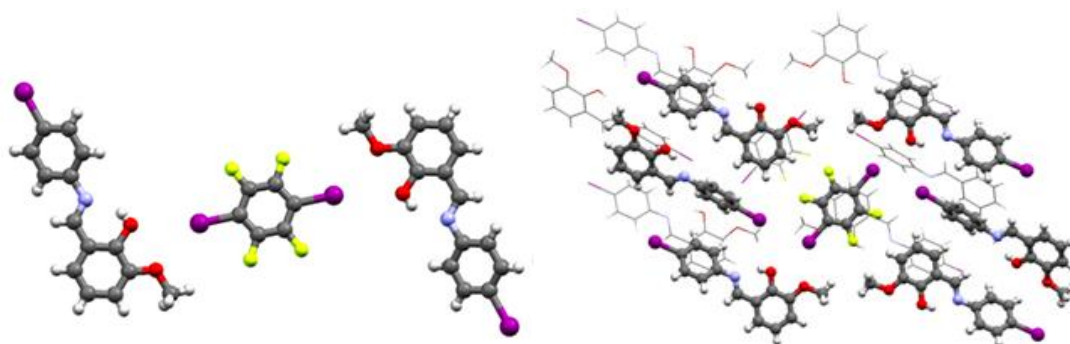


Figure II.10. Crystal structure of **3₂·I2F4**.

II.3.2 Solid state NMR spectroscopy

Parent compounds and the corresponding co-crystals have also been investigated by ^{13}C and ^{15}N CPMAS solid-state NMR experiments, in order to investigate on the tautomerism and the halogen bond (XB) occurrence.^{17,32}

Figures II.11 and II.12 show the relevant assignments in the ^{13}C and ^{15}N CPMAS spectra, respectively; while the ^{15}N chemical shifts (with assignments) are reported in Table II.2.

The ^{13}C chemical shifts of the C-OH and of the N=CH atoms as well as the ^{15}N chemical shift of the N=C atom, for parent compounds (**1**, **2** and **3_{solv}**) and the co-crystals (**1₂·I2F4**, **2₂·I2F4** and **3₂·I2F4**), are characteristic of the enol form. All structures, at room temperature, are characterised by the N···H-O interaction which was confirmed by the ^{15}N chemical shift of the N=CH atom around 285 ppm. The observed shifts in the co-crystals can be principally related to packing effects rather than N···O distances variations (see X-ray data). For all samples, the number of signals in the ^{13}C CPMAS spectra is consistent with one independent molecule ($Z'=1$) with the exception of compound **3**, which is characterised by independent molecules in the unit cell ($Z'=2$) as was observed by X-ray diffraction.

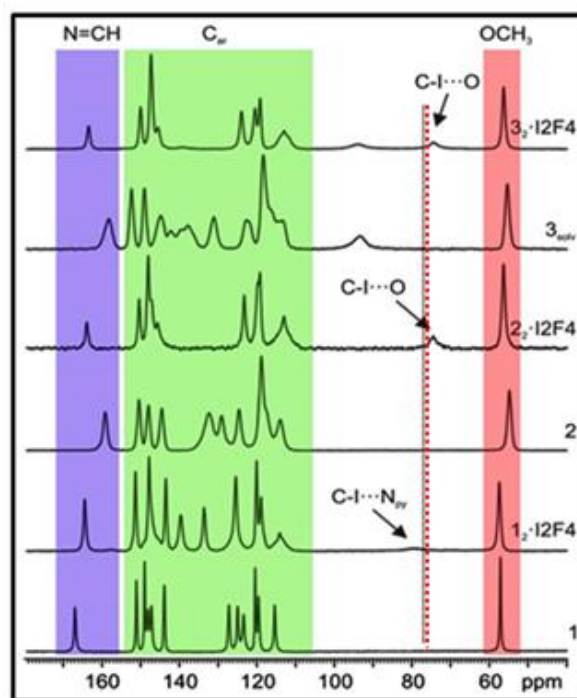


Figure II.11. RT ^{13}C (150.91 MHz) CPMAS spectra of parent compounds and corresponding co-crystals, recorded at 20 kHz. The red dotted line represents the position of the C-I signal of pure **I2F4**.

For the co-crystal **1₂·I2F4**, the occurrence of the halogen bond in which the pyridine nitrogen (N_{py}) atom is involved, has been observed by the ^{15}N CPMAS spectrum (Figure II.12). The XB formation can be indicated by the N_{py} signal, which undergoes a low-frequency shift, from 318.4 to 304.6 ppm upon co-crystallisation of **1** with **I2F4**. (Figure II.12).^{32b,33}

The formation of the halogen bond interaction has been also verified by the ^{13}C CPMAS spectrum, by the high-frequency shift of the C-I resonance from 77.0 ppm (pure **I2F4**) to 79.3 ppm (**1₂·I2F4**); which is in agreement with the lengthening of the C-I bond (from 2.075 to 2.095 Å) and it is compatible with previously reported shifts. For the co-crystals **2₂·I2F4** and **3₂·I2F4**, the observed shift of the C-I peak has been observed in the opposite direction (lower frequencies, from 77.0 ppm for pure **I2F4** to 74.4 and 74.5 ppm, respectively).

The obtained results may indicate that the XB interaction is very weak, as was also confirmed by the long $\text{I}\cdots\text{O}$ distances ($\text{I}\cdots\text{O}_{\text{CH}_3} = 3.264$ and 3.243 Å for **2₂·I2F4** and **3₂·I2F4**, respectively compared to **1₂·I2F4**, $\text{I}\cdots\text{N}_{\text{py}} = 2.878$ Å) and the poor directionality ($\text{C-I}\cdots\text{O}_{\text{CH}_3} = 140.7^\circ$ and 145.1° for **2₂·I2F4** and **3₂·I2F4**, respectively compare to **1₂·I2F4**, $\text{C-I}\cdots\text{N}_{\text{py}} = 168.9^\circ$).

We can conclude that ^{13}C chemical shift is more influenced by packing effects than by the polarisation induced by the halogen bond. In the case of $2_2 \cdot \text{I}_2\text{F}_4$ and $3_2 \cdot \text{I}_2\text{F}_4$, it seems that the driving force of the co-crystal formation is the packing efficiency rather than the halogen bond interaction formation.

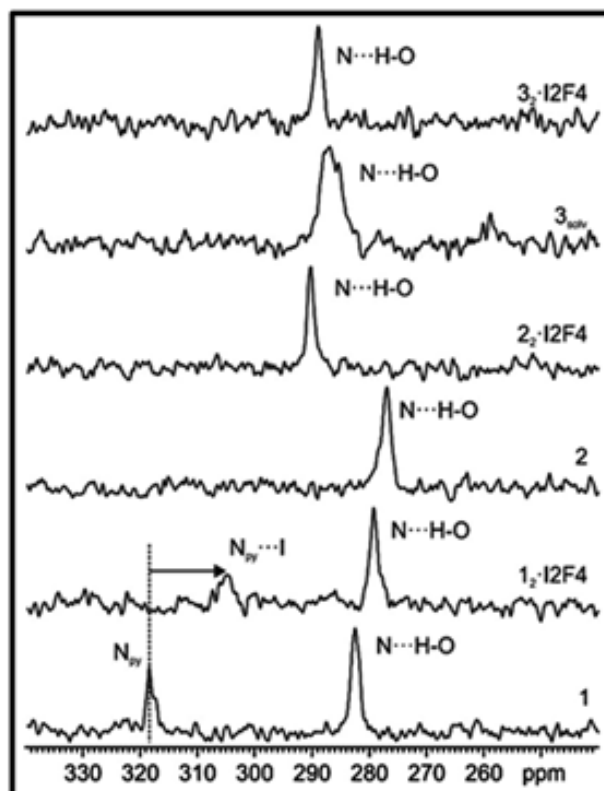


Figure II.12. RT ^{15}N (60.81 MHz) CPMAS spectra of parent compounds and corresponding co-crystals, recorded at 12 kHz.

Table II.2. RT ^{15}N chemical shifts with assignments for compounds **1**, **2** and 3_{solv} and their co-crystals $1_2 \cdot \text{I}_2\text{F}_4$, $2_2 \cdot \text{I}_2\text{F}_4$ and $3_2 \cdot \text{I}_2\text{F}_4$.

Sample	$\delta^{15}\text{N}$	Note
1	318.4	N_{py}
	282.4	$\text{C}=\text{N}\cdots\text{H}-\text{O}$
$1_2 \cdot \text{I}_2\text{F}_4$	304.6	$\text{N}_{\text{py}}\cdots\text{I}$
	279.2	$\text{C}=\text{N}\cdots\text{H}-\text{O}$
2	277.0	$\text{C}=\text{N}\cdots\text{H}-\text{O}$
$2_2 \cdot \text{I}_2\text{F}_4$	290.3	$\text{C}=\text{N}\cdots\text{H}-\text{O}$
3_{solv}^a	286.9	$\text{C}=\text{N}\cdots\text{H}-\text{O}$
$3_2 \cdot \text{I}_2\text{F}_4$	288.9	$\text{C}=\text{N}\cdots\text{H}-\text{O}$

^atwo molecules in the asymmetric unit.

II.3.3 Thermochromic behaviour

The effect of thermochromism can be easily appreciated on crystals by visual inspection. At low temperature the tautomeric equilibrium is completely shifted to the enol form, and the colour turns white (or light yellow), which is the typical colour of the enol form. When crystals are plunged in liquid nitrogen, immediately a colour change can be observed.^{5b} Figure II.13 shows pictures at room and at low temperature (77K) of the compounds under investigation.

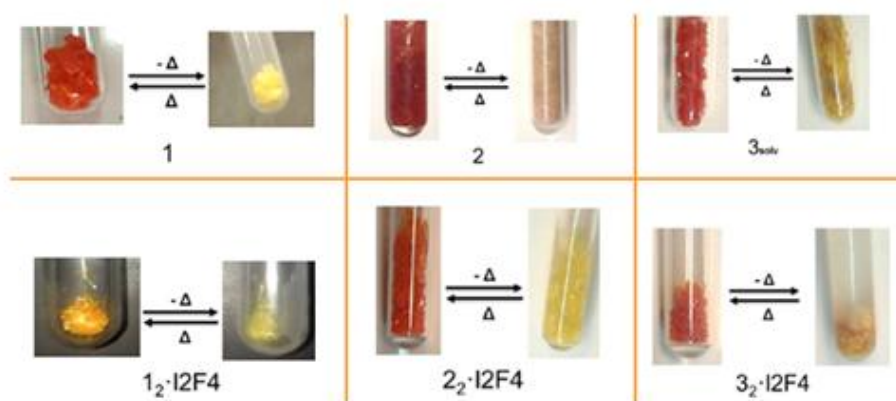


Figure II.13. Colour change, for parent compounds and their co-crystals, before and after immersion in liquid nitrogen.

In order to assess their thermochromic behaviour, absorption and emission properties have been measured, on parent compounds (**1**, **2**, **3_{solv}**) and their co-crystals (**1₂·I2F4**, **2₂·I2F4** and **3₂·I2F4**), at room (RT) and low temperature (LT, 77K). Samples have been measured as crystals and as ground crystals.

The absorption spectra of the ground crystals compounds (i.e. powder) are reported in Figure II.14. Two distinct broad bands are shown in the spectra of compounds **1**, **2**, and **3_{solv}**; one extending below $\lambda = 430$ nm and the second in the $\lambda = 430$ -550 nm region. These two bands are due to the π - π^* absorption of the enol form, and the thermally populated *cis*-keto form of the compounds, respectively.^{2,5a,6,8b,33d} The band around $\lambda = 470$ nm is characteristic of the *cis*-keto tautomer at room temperature, which was not identified by other characterisation techniques (i.e. X-ray diffraction and NMR in the solid state).^{5b} This discrepancy can be justified by the high absorption coefficient of the *cis*-keto form,³⁴ similar inconsistency has been reported in the literature in some cases.³⁵

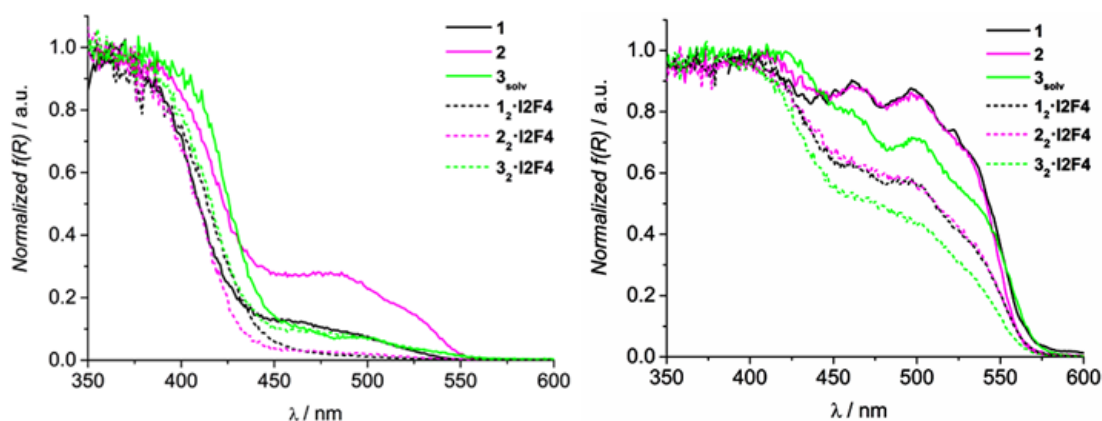


Figure II.14. Normalised absorption spectra of parent compounds and respective co-crystals (powder samples (left) and single crystal samples (right)).

Co-crystals spectra have shown similar features of those of their parent compounds, with the exception of a reduction of the contribution of the band at $\lambda = 470$ nm, especially in the case of $1_2 \cdot I2F4$ and $2_2 \cdot I2F4$.

The absorption spectra of the single crystal samples (see Figure II.14, right) show a different intensity distribution of the bands, with an evident absorption amplification in the $\lambda = 430$ -550 nm range. This aspect is due to a spectrum flattening in the region of high absorption (around $\lambda < 430$ nm) and an intensification in the long wavelength range (where the absorption is weaker) due to optical effects, related to scattering and reflection, occurring in the large size crystals (mm regime).³⁶

Figure II.15 shows the room temperature emission spectra of compounds **1**, **2**, 3_{solv} and their respective co-crystals (on powder samples) and Figure B.5 (see Appendix B) shows the emission spectra for crystal samples. The obtained emission spectral features upon excitation, in the $\lambda = 350$ -430 nm and in the $\lambda = 430$ -550 nm regions, were identical. Room temperature excitation spectra collected at $\lambda = 650/660$ nm (see Figure B.6 and B.7 for powders and single crystals, respectively) overlap the absorption bands with a comparable relative intensity.

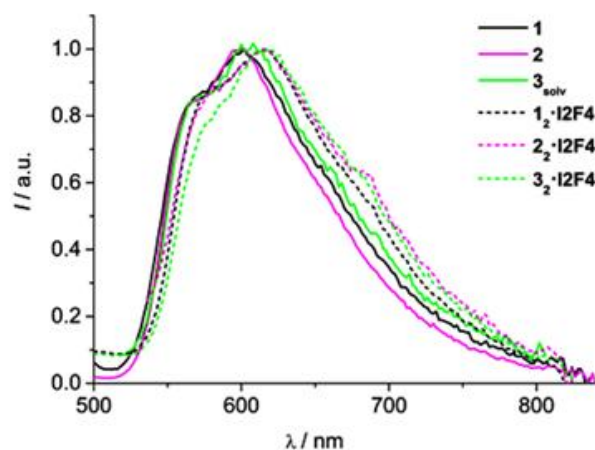


Figure II.15. Normalised room temperature emission spectra of powder samples of parent compounds and respective co-crystals. $\lambda_{\text{exc}} = 480$ nm.

The observed emission is due to the fluorescence of the *cis*-keto form, which can be obtained either via direct excitation of the *cis*-keto tautomer or by excitation of the enol tautomer. The excitation of these forms is followed by an excited state intramolecular proton transfer (ESIPT) process between the enol* and the *cis*-keto* forms.³⁷ As commonly observed for salicylideneaniline derivatives, no evidence of enol emission (below $\lambda = 500$ nm) has been observed, due to the fast kinetics of the ESIPT process, occurring in the sub-ps/few ps time regime in the solid state.³⁸

Comparing the emission features of compounds **1**, **2**, **3_{solv}** and their co-crystals, we observed a similar behaviour within the two series: whereas parent compounds **1**, **2** and **3_{solv}** show maxima at ca. $\lambda = 600$ nm, in the case of the co-crystals the fluorescence is red-shifted by 10-20 nm (Figure III.15 and B.5 and Table II.3). This shift is ascribed to a general excited state stabilisation effect due to the co-crystallisation process.

The nature of the emission was confirmed by absolute emission quantum yields, even if they were found to be below the limit of detection of our system (2%) and single exponential decays with lifetimes of few hundreds of ps were measured for all compounds (data are reported in Table II.3).

The latter data confirmed that the emission is due to the low-lying singlet excited state of the *cis*-keto tautomer.³⁸

Table II.3. Fluorescence data at RT and 77K for powder samples (in square brackets are reported the values for single crystal samples).

	298 K		77K	
	$\lambda_{\text{max}} / \text{nm}^{\text{a}}$	$\tau / \text{ps}^{\text{b}}$	$\lambda_{\text{max}} / \text{nm}^{\text{a}}$	$\tau / \text{ps}^{\text{b}}$
1	568 sh, 600 [574 sh, 602]	344 [344]	558, 598, 646 sh [558, 600, 642 sh]	185 (15%), 693 (85%) [273 (30%), 858 (70%)]
2	568 sh, 598 [572 sh, 598]	508 [511]	556, 594, 644 sh [558, 594, 642 sh]	164 (5%), 1328 (95%) [158 (5%), 1358 (95%)]
3_{solv}	570 sh, 606 [578 sh, 610]	175 [180]	558, 602, 650 sh [560, 604, 652 sh]	205 (30%), 674 (70%) [314 (55%), 896 (45%)]
1₂·I2F4	580 sh, 616 [584 sh, 616]	191 [210]	570, 610, 664 sh [570, 610, 662 sh]	204 (60%), 436 (40%) [262 (70%), 713 (30%)]
2₂·I2F4	580 sh, 614 [580 sh, 616]	133 [113]	574, 612, 662 sh [572, 608, 656 sh]	176 (50%), 401 (50%) [240 (50%), 456 (50%)]
3₂·I2F4	584 sh, 614 [580 sh, 618]	97 [98]	576, 616, 668 sh [578, 618, 670]	180 (30%), 334 (70%) [212 (70%), 454 (30%)]

^aFrom corrected emission spectra; ^bFluorescence lifetimes, excitation at $\lambda=407 \text{ nm}$.

A decrease in lifetime has been observed moving from parent compounds to their co-crystals; this effect can be ascribed to an external heavy atom effect induced by the halogenated coformer used in the co-crystallisation process.¹⁴

Low-temperature emission

Emission properties of all compounds, both on powder and single crystal samples, have also been investigated at low temperature (77 K). The emission features are similar to those observed at room temperature with the exception of resolution (see Figure II.16). The low-temperature spectra have shown a higher spectral resolution in the $\lambda = 540\text{-}590 \text{ nm}$ region, where a band appeared in place of the weak shoulder detected at room temperature and blue-shifted by ca. 10 nm with respect to it.

This phenomenon of a blue-shifted emission peak at low temperature has been observed in similar systems and it has been explained as an emissive *cis*-keto excited state characterised by a distorted and less stable conformation. At room temperature, this conformation is quenched because of the fast relaxation to the more stable planar excited state responsible for emission in the longer wavelength region.^{37,33d,39} For all compounds under investigation, a bi-exponential behaviour of the emission decay has been observed across the whole spectral region (Table II.3), which confirmed the existence of a conformational change in the excited states of the *cis*-keto form.

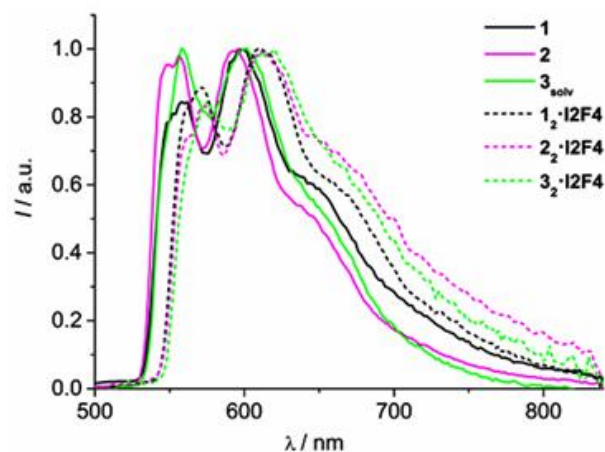


Figure II.16. Normalised emission spectra at LT of powder samples of compounds ($\lambda_{\text{exc}} = 450$ nm).

The analysis of the thermochromic features of the parent compounds and corresponding co-crystals permitted us to obtain these following results:

- i) the emission spectra of the co-crystals are bathochromically shifted by 10-20 nm compared to those of the parent compounds, this behaviour has been observed either at room and low temperature;
- ii) low-temperature excitation spectra (collected at $\lambda = 600\text{-}620$ nm) show an evident depression of the $\lambda = 430\text{-}550$ nm absorption region with respect to the same spectra collected at room temperature (see Figure B.9 and B.10, and, as one representative comparison see Figure II.17). This behaviour, responsible for the yellowing of the colour of the samples at LT, observable with the naked eye, is due to the decrease of the population of the *cis*-keto form in the ground state. The low temperature, indeed, inhibits the thermal enol-keto tautomerism and suppresses the formation of the *cis*-keto form which absorb in the $\lambda = 430\text{-}550$ nm region.

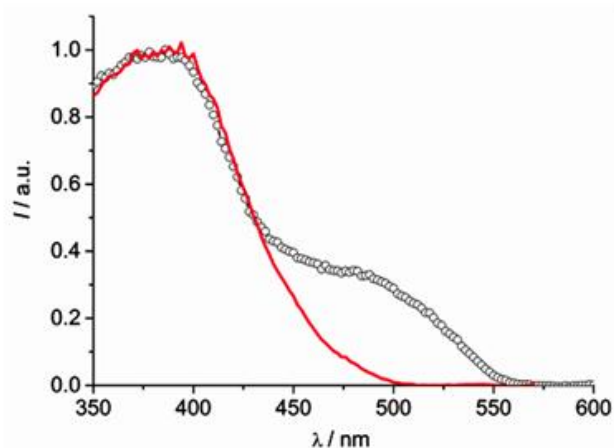


Figure II.17. Comparison of normalised excitation spectra of compound **1** (powder sample) at RT (open dots, $\lambda_{\text{em}} = 650$ nm) and at LT (red line, $\lambda_{\text{em}} = 600$ nm).

iii) the observed emission, ascribed to the excited *cis*-keto form, is a result of the fast ES IPT process that follows excitation of the enol tautomer. The ES IPT process is operative also at low temperature.^{35a,38a}

iv) all the examined compounds have exhibited thermochromism; it has been deduced by a careful comparison of room and low-temperature excitation spectra.

II.3.4 Photochromic behaviour

Photochromism has been investigated, for all compounds, by irradiating the powder samples at $\lambda = 365$ nm. Absorption, emission and FT-IR spectroscopy have been employed to investigate photochromism. On solids which have shown photochromism, have been performed both kinetics of the photochemical back reaction (excitation of samples at $\lambda = 546$ nm) and thermal fading (by leaving the samples in the dark at RT).

After UV irradiation, absorption and emission spectra were performed on samples. No variations were observed after irradiation of compounds **1**, **1₂·I2F4** and **3_{solv}** while for **2**, **2₂·I2F4** and **3₂·I2F4**, irradiation brought significant variations in the absorption spectral features. For compounds **2**, **2₂·I2F4** and **3₂·I2F4**, the emission behaviour, upon excitation at $\lambda = 400$ nm, has been analyzed as a function of the irradiation time. Figure III.18 shows the observed variations in the absorption and emission spectra for co-crystal **3₂·I2F4** upon irradiation at $\lambda = 365$ nm (the analogous results experiments for **2** and **2₂·I2F4** are reported in Figure B.12 and B.13). An increase of absorption was observed in the $\lambda = 450$ -600 nm region, due to irradiation, and a photostationary state was reached after 40 minutes of exposure (Figures II.18 (left), B.12 and B.13). The observed absorption variation in the

spectra can be ascribed to the formation of the *trans*-keto form which is formed by the enol→*trans*-keto photoreaction in the longer wavelength range of the spectrum ($\lambda = 500$ - 600 nm).^{7,10a,40} In the emission spectra, a change in the relative intensity of the bands was observed, i.e. an increase in the $\lambda = 600$ - 800 nm region and a decrease of the shoulder at $\lambda = 560$ - 570 nm (Figures II.17 (right), B.12 and B.13 (right); the spectra have been arbitrarily scaled to better visualise changes in the intensity ratio).

Excitation spectra were collected, at $\lambda = 575$ nm and $\lambda = 650$ nm, in the photostationary state (Figure B.14). They have shown that the absorption in the $\lambda = 450$ - 600 nm region contributes to a larger extent to emission at $\lambda = 650$ nm. Therefore, the observed emission in the $\lambda = 600$ - 800 nm region can be reliably ascribed to the *trans*-keto form of the investigated anils.

Emission lifetimes were measured in the photostationary state ($\lambda > 650$ nm; 449 ps, 126 ps and 97 ps for **2**, **2₂·I2F4** and **3₂·I2F4**, respectively) and they were comparable to those obtained before irradiation (values are reported in Table II.3).

Co-crystal **3₂·I2F4** is reported as example, since it is the one showing the largest spectral changes due to photoisomerisation (Figure II.18).

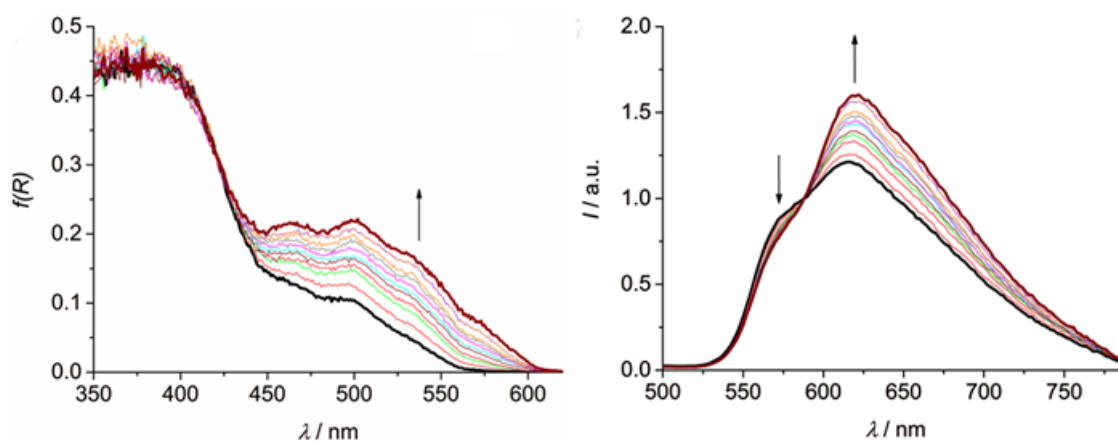


Figure II.18. Absorption (left) and emission (right) spectra of **3₂·I2F4** before (black thick) and after (red thick) irradiation at $\lambda = 365$ nm for 40 min (20 min LP and 20 min HP). Thin lines represent spectra at intermediate times. In emission the spectra have been arbitrarily normalised at $\lambda = 588$ nm; $\lambda_{\text{exc}} = 400$ nm.

In literature, the suggested mechanism for the photochromic process states that upon excitation of the enol form and the related proton transfer, the excited distorted keto intermediate may deactivate to both the lower lying *cis*-keto or the *trans*-keto excited states

since it is the precursor of both.^{35a,39} The emission of the photogenerated *trans*-keto tautomer is not common and it has been rarely reported in literature.^{8b,35b,41}

The initial absorption spectra of **2**, **2₂·I2F4** and **3₂·I2F4** can be totally recovered in two ways: i) photochemically, upon excitation of the samples at $\lambda = 546$ nm and ii) thermally, by leaving the samples in the dark (room temperature).

Spectral and kinetic features of the recovery processes are shown in Figures B.15 - B-19. Some differences in the two processes have been observed: photochemical back reactions are characterised by a bi-exponential behaviour, instead, the thermal fading processes by first-order reactions (Figure II.19). For the *trans*-keto form of solid-state anils, a two-stage thermal decay has been previously reported in the literature.^{7,10,41b} The two co-crystals **2₂·I2F4** and **3₂·I2F4** have shown a much faster back reactions compared to the parent compound **2**: the photoconversion kinetics of the *trans*-keto tautomer is of the order of tens of seconds for **2₂·I2F4** and **3₂·I2F4** and tens of minutes for **2** (Figures B.15 and B.16).

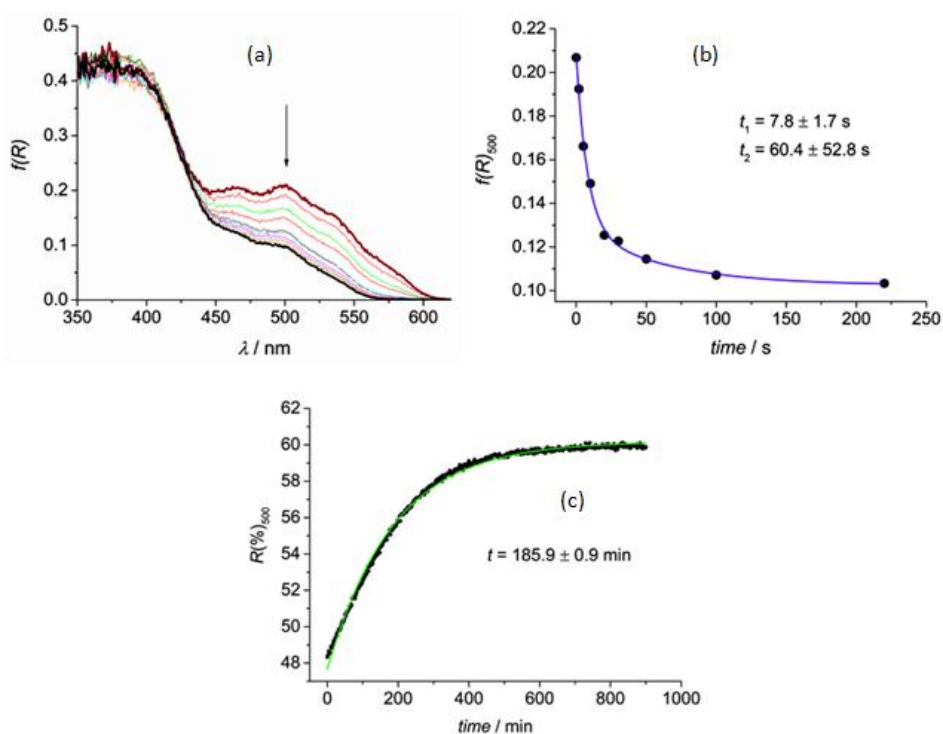


Figure II.19. (a) Absorption spectral changes of **3₂·I2F4** starting from the photostationary state and following irradiation at $\lambda = 465$ nm for 220 s. (b) Data points at $\lambda = 500$ nm from graph (a) and bi-exponential fitting (blue). (c) Variation of the reflectance of **3₂·I2F4** at $\lambda = 500$ nm as a function of time, starting from the photostationary state and following the thermal back reaction; in green the mono-exponential fitting.

Regarding the thermal fading, for the *trans*-keto form of compounds **2**, **2₂·I2F4** and **3₂·I2F4** conversion times of 604 min, 65 min and 186 min have been measured, respectively. This can serve as a confirmation that compound **2** undergoes the slowest process.

II.3.5 FT-IR spectroscopy

FT-IR spectroscopy measurements were performed for all compounds, which were dispersed in KBr pellets.

FT-IR spectra were collected on pellets before and after UV irradiation (20 min at $\lambda = 365$ nm). After the irradiation process, some visible variations in the spectra were found, in agreement with the formation of the *trans*-keto form.^{8a,42} The band ascribed to the C=N stretching of the enol form (around 1612 cm^{-1}) decreases and the small band due to the C=O stretching of the *trans*-keto tautomer (around 1642 cm^{-1}) appears. The original spectrum was recovered by thermal treatment (80°C , 20 min), this can serve as confirmation of reversibility of the process. A colour change can be observed during this process: from yellow to orange upon irradiation, and to yellow again after thermal treatment (see Figure II.20 for **2₂·I2F4** and Figures B.20 and B.21 in Appendix B for the other compounds discussed in the present work). FT-IR results are in agreement with those observed in absorption and emission measurements.

Photochromism was observed in the case of compounds **2**, **2₂·I2F4** and **3₂·I2F4**.

It was not observed in compounds **3_{solv}**, **3A** and **3B**, which is curious since compound **3B**, being isomorphous with **2**, which resulted to be photochromic, was expected to behave similarly. Finally, the **2_{0.7}3_{0.3}** solid solution did not show photochromism effect; we assumed that the presence of a lower amount of iodine with respect to bromine can be sufficient to switch off the photochromic behaviour.

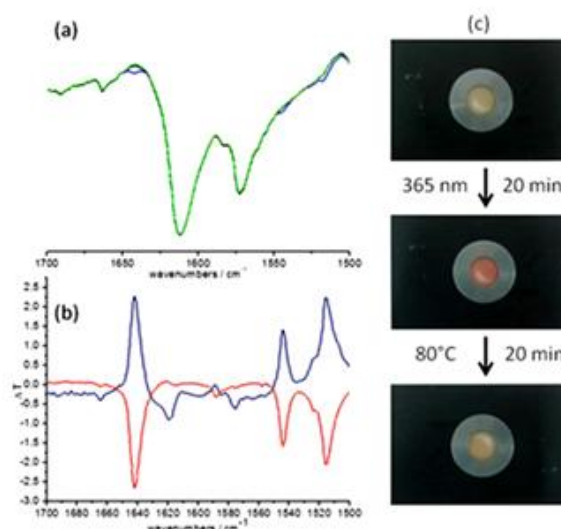


Figure II.20. FT-IR measurements for $2_2 \cdot \text{I2F4}$ dispersed in KBr pellets: (a) spectra of the untreated sample (black), after irradiation (blue) and after thermal recovery (green); (b) comparison of the untreated and the irradiated spectra (blue) and between the irradiated and the thermal recovered one (red); (c) pictures taken on the measured KBr pellets.

II.4 Conclusions

We have investigated on thermo- and photochromism phenomena in a series of selected N-salicylideneanilines and N-salicylideneaminopyridines, using co-crystallisation as a crystal engineering approach. The goal of the work was to investigate the differences, in terms of crystal packing, between the parent compounds (i.e. **1**, **2**, **3**) and their co-crystals, obtained by means of reaction with **I2F4** ($1_2 \cdot \text{I2F4}$, $2_2 \cdot \text{I2F4}$, $3_2 \cdot \text{I2F4}$).

All the investigated compounds have been synthesised by means of mechanochemistry and obtained with high yield without the use of solvents. Compound **3** was obtained in three different crystal forms, i.e. **3A** (EtOH), **3B** (toluene), **3_{solv}** (EtOAc solvate). The same tendency to form multiple crystal forms was not observed for the compound **2**, which is isostructural with **3**.

The formation of the halogen bond C-I \cdots O(hydroxyl) - the hydroxyl involved in the enol/*cis*-keto tautomerism - does not displace the ground state enol/*cis*-keto balance toward the *cis*-keto form, neither at room nor at low temperature.

Thermochromism was observed for all compounds (colour change from yellow-orange to pale yellow by lowering the temperature). Photochromic behaviour was observed only for compounds $2_2 \cdot \text{I2F4}$ and $3_2 \cdot \text{I2F4}$. Although several studies in the field report that thermo-

and photochromism are mutually exclusive, some investigated crystalline have shown both phenomena.

Photochemical back reaction and thermal fading process have been investigated in all compounds, the first one is described as a bi-exponential process and the second one as a first-order reaction.

Either negative and positive violations of the dihedral angle-based rule have been found. Crystalline **1** and **1₂·I2F4** are non-photochromic despite suitable values of $\Phi > 25^\circ$ (negative violations) whereas crystalline **2** is photochromic since it presents not a suitable value of Φ (positive violation). Although crystals **2** and **3B** are isostructural, they did not show similar behaviour. In fact, **2** is photochromic whereas **3B** does not show such a behaviour.

The solid solution of compound **2** and **3**, compound **2_{0.7}3_{0.3}**, even though it is isostructural to solids **2** and **3B**, it did not show photochromic behaviour. This effect can in part be due to the hindering effect of the large iodine atom on the free pedal motion.

An effect of the iodine atom was also observed in the case of co-crystals **2₂·I2F4** and **3₂·I2F4** where the p-iodine substituent is not big enough to turn photochromism off, but it delays (of about three times) the thermal fading process. We observed that the ability to undergo photoisomerisation for co-crystals **2₂·I2F4** and **3₂·I2F4** is higher with respect to **2**. This was confirmed by the fact that the photochemical back reaction (tens of seconds for **2** and tens of minutes for **2₂·I2F4** and **3₂·I2F4** respectively) and the thermal fading process (604 min, 65 min and 186 min for **2**, **2₂·I2F4** and **3₂·I2F4** respectively) are much faster for compounds **2₂·I2F4** and **3₂·I2F4** with respect to compound **2**. These results are consistent with a structure opening effect made by the insertion of the I2F4 coformer in the crystal packing.

The obtained results highlight how co-crystallisation can affect the solid-state photochromic behaviour. The empirical rules (considerations based only on structural considerations) not always can be employed for the rationalisation/prediction of photochromism.

III.5 Experimental section

Materials: *Ortho*-Vanillin (*2-Hydroxy-3-methoxybenzaldehyde*), 3-aminopyridine, 4-bromoaniline and 4-iodoaniline were bought from Sigma-Aldrich and were used as commercially obtained. Solvents used for crystallisation (EtOH, EtOAc, cyclohexane and toluene) were used without further purification.

Syntheses: N-salicylideneanilines, N-salicylideneaminorpyridines and their corresponding co-crystals were synthesised by mechanosynthesis. Syntheses were performed by grinding with a Retsch MM 400 Mixer Mill, equipped with two jars in which five 2 mL Eppendorf tubes can be installed with 8–10 stainless steel grinding balls (1 mm diameter) in a sample. A near-total conversion is obtained due to the absence of residual peaks of both reagents in the ground product. The conversion was always verified by a comparison of the chemical and structural identity between bulk materials and single crystals, by comparing simulated and experimental powder diffraction patterns (see Figures B.3 and B.4 in Appendix B).

1: (E)-2-methoxy-6-(pyridin-3-yliminomethyl)phenol. Compound **1** was synthesised by grinding of equimolar amounts of 3-aminopyridine and *ortho*-vanillin. Orange prisms of compound **1**, suitable for X-ray analysis, have been obtained after 4 days, by slow evaporation from a saturated solution of ethyl acetate at room temperature.

2: 2-[(1E)-[(4-bromophenyl)imino]methyl]-6-methoxyphenol. Compound **2** was also synthesised by grinding of equimolar amounts of 4-bromoaniline and *ortho*-vanillin. Orange needles of compound **2**, suitable for X-ray analysis, have been obtained from a saturated solution in ethyl acetate after 3 days by slow evaporation at room temperature.

3A, 3B, 3_{solv}: 2-[(1E)-[(4-iodophenyl)imino]methyl]-6-methoxyphenol. The synthesis was done by grinding of equimolar amounts of 4-iodoaniline and *ortho*-vanillin. Recrystallisation from several solvents was performed in order to obtain single crystals suitable for X-ray diffraction. Moreover, two polymorphs and a solvate form of **3** were obtained, depending on the crystallisation conditions. Orange-red blocks of form **3A** were obtained by slow evaporation of a saturated solution in EtOH. Orange-red crystals of form **3B** were obtained by seeding **2** in a saturated toluene solution, and leaving it to slowly evaporate, while orange-red prisms of form **3_{solv}** were obtained by recrystallisation from ethyl acetate.

Comparison between experimental (the ground powder, taken directly after synthesis) and calculated (on the basis of single crystal data for **3A**, **3B** and **3_{solv}**) diffractograms reveals the selective formation of form **3A** (see Figure B.3).

2_{0.7}-3_{0.3} solid solution: Equimolar quantities of **2** and **3_{solv}** were dissolved in ethyl acetate; crystals of suitable dimensions for X-ray diffraction were obtained after 2 days by slow evaporation of solvent at room temperature.

1₂·I2F4: Co-crystallisation of compound **1** and **I2F4** was achieved by grinding (2:1 molar ratio). Orange-yellow single-crystals (needles) suitable for X-ray diffraction have been obtained, after 5 days, by slow evaporation of saturated solutions in ethanol/cyclohexane.

2₂·I2F4: Co-crystallisation was performed by grinding of compound **2** and **I2F4** (2:1 molar ratio). After recrystallisation from ethanol/cyclohexane, at room temperature, orange prisms have been obtained.

3₂·I2F4: Co-crystallisation was performed by grinding of compound **3** and **I2F4** in a 2:1 molar ratio. Recrystallisation in ethanol/cyclohexane yielded orange prisms after 4 days.

Single crystal X-ray diffraction: Single-crystal diffraction data for **1**, **2**, **3_{solv}**, **1₂·I2F4**, **2₂·I2F4** and **3₂·I2F4** were collected at RT and LT on a Gemini Ultra R system (4-circle kappa platform, Ruby CCD detector) using Mo K α ($\lambda = 0.71073\text{\AA}$) radiations. Single-crystal diffraction data for **3A**, **3B** and **2_{0.7}·3_{0.3}** were collected at RT on an Oxford X'Calibur S CCD diffractometer equipped with a graphite monochromator (Mo K α radiation, $\lambda = 0.71073\text{\AA}$). Structures were solved by direct methods using the WinGX suite of programs⁴³ with Sir-2014⁴⁴ and then refined using either SHELX-97 or SHELXL-2014⁴⁵. Non-hydrogen atoms were anisotropically refined and the hydrogen atoms (not implicated in H-bonds) in the riding mode with isotropic temperature factors fixed at 1.2 times U(eq) of the parent atoms. Hydrogen atoms implicated in hydrogen bonds were localized by Fourier difference maps. The solvent of crystallisation in the structure of **3_{solv}** could not be unambiguously determined, therefore, the contribution of the solvent to the calculated structure factors was taken into account by using the SQUEEZE procedure of PLATON.⁴⁶ Positional disorder (70:30) in crystalline **3A** was treated by first refining the occupancy parameter of iodine, then fixing the occupancy factor and freely refining the thermal parameter. The whole minor image of disorder was located experimentally, but only the iodine atom was refined anisotropically. Disorder in the bromine/iodine position was treated analogously in the solid solution **2_{0.7}·3_{0.3}**. The program Mercury⁴⁷ was used for molecular graphics.

Powder Diffraction Measurements: X-ray powder diffractograms in the 2θ range 5-40° (step size 0.02°; time/step, 20s; 40mA x 40kV) were collected on a Panalytical X'Pert PRO automated diffractometer equipped with a X'Celerator detector and in Bragg-Brentano geometry using Cu K α radiation. The program Mercury⁴⁷ has been used for simulation of X-ray powder patterns on the basis of single crystal data.

FT-IR spectroscopy: FT-IR spectra were collected using a Bruker Alpha FT-IR spectrometer. FT-IR spectra in the range 1700-1500 cm^{-1} were run on KBr pellets (sample amount: 1-2 mg, KBr amount: 200 mg), resolution was set to 2 cm^{-1} , and 128 cycles for both background and measurement were collected. Spectra were run before and after 20 min of UV irradiation ($\lambda = 365\text{ nm}$) on the same pellet sample. Pellets were irradiated

directly in the sample holder using 2 UV-LED (LED ENGINE LZ1-10UV00-0000, $\lambda = 365$ nm) placed at a distance of 1 cm each. If a change in the colour or in the spectrum was observed, a further spectrum was measured after thermal treatment (pellet kept in the oven at 80°C for 20 minutes).

Crushed pellets were subjected to powder X-Ray diffraction analysis to exclude any solid state reaction triggered by pressure during pellet formation. As evidenced by powder patterns all crystalline materials resulted stable and did not react with KBr during pellet preparation (see Appendix B for details).

Solid-state NMR spectroscopy: Solid-state NMR spectra were acquired on a Jeol ECZR 600 instrument operating at 600.17, 150.91 and 60.81 MHz for ^1H , ^{13}C and ^{15}N nuclei, respectively. The samples were packed in a 3.2 mm rotor (volume = 50 μL) and spun at 20 and 12 kHz for ^{13}C and ^{15}N nuclei, respectively. All data were collected at ambient probe temperatures. All ^{13}C and ^{15}N experiments employed the RAMP-CP pulse sequence (^1H 90° pulse=2.189 μs , contact time = 9 and 4 ms, respectively) with the TPPM ^1H decoupling with an rf field of 75 kHz during the acquisition period. Detailed acquisition parameters may be found in Appendix B (Table B.5). ^{13}C and ^{15}N chemical shift scales were referenced with the resonance of hexamethylbenzene (^{13}C methyl signal at 17.4 ppm), and glycine (^{15}N signal at 33.4 ppm with respect to NH_3), respectively as external standards.

Absorption and emission spectroscopy: Measurements were performed both on single crystals and on gently crushed powder samples placed inside two quartz slides. Reflectance spectra of solid samples were acquired with a PerkinElmer Lambda 9 UV/Vis/NIR spectrophotometer equipped with a 60 mm integrating sphere and converted in absorption spectra using the Kubelka–Munk function.⁴⁸ Emission spectra were collected in front-face mode with an Edinburgh FLS920 fluorimeter equipped with a Peltiercooled Hamamatsu R928 PMT (200–850 nm), and corrected for the wavelength dependent phototube response. Absolute emission quantum yields were determined according to the method reported by Ishida et al.,⁴⁹ by using the same fluorimeter equipped with a 4 inch Labsphere integrating sphere. The limit of detection of the system is 0.020. Measurements at 77K made use of quartz capillary tubes immersed in liquid nitrogen contained in a home-made quartz Dewar. Band maxima and luminescence intensities are obtained with uncertainties of 2 nm and 10%, respectively. Fluorescence lifetimes were determined with an IBH 5000F time-correlated single-photon counting apparatus equipped with a TBX Picosecond Photon Detection Module by using a pulsed 407 nm laser diode (59 ps pulse width)

powered by a Hamamatsu C4725 light pulser as excitation source. Analysis of the fluorescence decay profiles against time was accomplished with the Decay Analysis Software DAS6 provided by the manufacturer. The estimated error on lifetime determinations is 10%.

Photochemistry: Photochromic investigations have been performed by irradiating a thin layer of the powder sample, placed inside two quartz slides, by using a collimated 100 W Hg arc lamp and selecting the desired spectral lines ($\lambda = 365$ or 546 nm) by means of bandpass interference filters. Forward reactions ($\lambda_{\text{irr}} = 365$ nm) made use of two different light powers: 2 mW cm^{-2} (low power: LP) and 20 mW cm^{-2} (high power: HP), the former obtained by using a neutral density filter. For back reactions ($\lambda_{\text{irr}} = 546$ nm) the light intensity was 5 mW cm^{-1} . Thermal fading was analyzed by a reflectance (%) time scan at a single wavelength ($\lambda = 500$ nm) performed with the spectrophotometer described above; the experimental conditions allowed for a close to dark environment.

Thermogravimetric Analyses (TGA): Measurements were performed with a Perkin-Elmer TGA7 in the temperature range $40\text{--}350$ °C under N_2 gas flow at a heating rate of 5.00 °C min^{-1} .

Differential Scanning Calorimetry (DSC): Measurements were performed with a Perkin-Elmer PyrisDiamond DSC. Samples (3-5 mg) were placed in aluminum open pans. Heating was carried out at 5.00 °C min^{-1} for all samples, in the temperature range $40\text{--}140$ °C.

II.6 References

1. J. Zhang, Q. Zou, H. Tian, *Adv. Mater.*, **2013**, 25, 378–399.
2. (a) T. Fujiwara, J. Harada, K. Ogawa, *J. Phys. Chem. B*, **2004**, 108, 4035–4038; *J. Phys. Chem. C*, **2017**, 121, 6898–6908; (b) J. Quertinmont, A. Carletta, N. A. Tumanov, T. Leyssens, J. Wouters, B. Champagne, *J. Phys. Chem. C*, **2017**, 121, 6898–6908.
3. (a) S. Kawata, Y. Kawata, *Chem. Rev.*, **2000**, 100, 1777–1788; (b) J. Cusido, E. Deniz, F. M. Raymo, *European J. Org. Chem.*, **2009**, 2009, 2031–2045.
4. K. Johmoto, A. Sekine, H. Uekusa, *Cryst. Growth Des.*, **2012**, 12, 4779–4786.
5. (a) J. Harada, K. Ogawa, *Chem. Soc. Rev.*, **2009**, 38, 2244–2252; (b) E. Hadjoudis, I. M. Mavridis, *Chem. Soc. Rev.*, **2004**, 33, 579–588.
6. J. Harada, T. Fujiwara, K. Ogawa, *J. Am. Chem. Soc.*, **2007**, 129, 16216–16221.
7. K. Johmoto, T. Ishida, A. Sekine, H. Uekusa, Y. Ohashi, *Acta Crystallogr. Sect. B*

- Struct. Sci.*, **2012**, 68, 297–304.
8. (a) A. Carletta, X. Buol, T. Leysens, B. Champagne, J. Wouters, *J. Phys. Chem. C*, **2016**, 120, 10001–10008; (b) F. Robert, A. D. Naik, B. Tinant, R. Robiette, Y. Garcia, *Chem. - A Eur. J.*, **2009**, 15, 4327–4342.
 9. (a) K. M. Hutchins, S. Dutta, B. P. Loren, L. R. MacGillivray, *Chem. Mater.*, **2014**, 26, 3042–3044; (b) P.-L. Jacquemin, K. Robeyns, M. Devillers, Y. Garcia, *Chem. - A Eur. J.*, **2015**, 21, 6832–6845.
 10. (a) I. O. Staehle, B. Rodríguez-Molina, S. I. Khan, M. A. Garcia-Garibay, *Cryst. Growth Des.*, **2014**, 14, 3667–3673; (b) M. Sliwa, S. Létard, I. Malfant, M. Nierlich, P. G. Lacroix, T. Asahi, H. Masuhara, P. Yu, K. Nakatani, *Chem. Mater.*, **2005**, 17, 4727–4735.
 11. (a) G. R. Desiraju, *Angew. Chemie Int. Ed.*, **2007**, 46, 8342–8356; (b) G. R. Desiraju, *Angew. Chemie Int. Ed. English*, **1995**, 34, 2311–2327.
 12. P. Metrangolo, G. Resnati, *Chem. - A Eur. J.*, **2001**, 7, 2511–2519.
 13. L. Meazza, J. A. Foster, K. Fucke, P. Metrangolo, G. Resnati, J. W. Steed, *Nat. Chem.*, **2012**, 5, 42–47.
 14. F. Grepioni, S. d'Agostino, D. Braga, A. Bertocco, L. Catalano, B. Ventura, *J. Mater. Chem. C*, **2015**, 3, 9425–9434.
 15. (a) S. d'Agostino, F. Grepioni, D. Braga, B. Ventura, *Cryst. Growth Des.*, **2015**, 15, 2039–2045; (b) H. Wang, R. X. Hu, X. Pang, H. Y. Gao, W. J. Jin, *CrystEngComm*, **2014**, 16, 7942–7948.
 16. J. Xu, X. Liu, J. K.-P. Ng, T. Lin, C. He, *J. Mater. Chem.*, **2006**, 16, 3540–3545.
 17. M. Baldrighi, G. Cavallo, M. R. Chierotti, R. Gobetto, P. Metrangolo, T. Pilati, G. Resnati, G. Terraneo, *Mol. Pharm.*, **2013**, 10, 1760–1772.
 18. K. Ogawa, Y. Kasahara, Y. Ohtani, J. Harada, *J. Am. Chem. Soc.*, **1998**, 120, 7107–7108.
 19. (a) A. Carletta, F. Spinelli, S. d'Agostino, B. Ventura, M. R. Chierotti, R. Gobetto, J. Wouters, F. Grepioni, *Chem.–Eur. J.*, **2017**, 23, 5317–5329; (b) This work was done in collaboration with: i) Prof. Johan Wouter's group from the University of Namur (Belgium); ii) Dr. Barbara Ventura from National Research Council of Italy (ISOF-CNR, Bologna, Italy) - I worked, under her supervision, on the photophysical characterisation of the compounds investigated - and iii) Prof. Roberto Gobetto and Prof. Michele Chierotti from the University of Torino (Italy, for the solid state NMR measurements).

20. Z. L. Jing, R.-N. Li, N. Yang, *Acta Crystallogr. Sect. E*, **2007**, 63, 3001–3001.
21. C. S. Zheng, N. Yang, M. Li, Z.-L. Jing, *Acta Crystallogr. Sect. E*, **2005**, 61, 3613–3614.
22. (a) D. Braga, L. Maini, F. Grepioni, *Chem. Soc. Rev.*, **2013**, 42, 7638–7648; (b) A. Carletta, J. Dubois, A. Tilborg, J. Wouters, *CrystEngComm*, **2015**, 17, 3509–3518; (c) A. Tilborg, G. Springuel, B. Norberg, J. Wouters, T. Leyssens, *Cryst. Growth Des.*, **2014**, 14, 3408–3422.
23. (a) G. Kaupp, *J. Phys. Org. Chem.*, **2008**, 21, 630–643; (b) G. Kaupp, *CrystEngComm*, **2009**, 11, 388.
24. F. Toda, *Acc. Chem. Res.*, **1995**, 28, 480.
25. D. Braga, F. Grepioni, *Angew. Chem. Int. Ed.*, **2004**, 43, 4002–4011.
26. (a) T. Frisčić and W. Jones, *Cryst. Growth Des.*, **2009**, 9, 1621; (b) J. L. Do, T. Frisčić, *ACS Cent. Sci.*, **2017**, 3, 13–19.
27. D. Braga, S. L. Giaffreda, F. Grepioni, A. Pettersen, L. Maini, M. Curzi, M. Polito, *Dalton Trans.*, **2006**, 1249.
28. S. L. James, C. J. Adams, C. Bolm, D. Braga, P. Collier, T. Frisčić, F. Grepioni, K. D. M. Harris, G. Hyett, W. Jones, A. Krebs, J. Mack, L. Maini, A. G. Orpen, I. P. Parkin, W. C. Shearouse, J.W. Steed, D.C. Waddelli, *Chem. Soc. Rev.*, **2012**, 41, 413–447.
29. (a) M. Angeles Garcia, C. Ljpez, R. M. Claramunt, A. Kenz, M. Pierrot, J. Elguero, *Helv. Chim. Acta*, **2002**, 85, 2763–2776; (b) W. Holzer, R. M. Claramunt, C. Ljpez, I. Alkorta, J. Elguero, *Solid State Nucl. Magn. Reson.*, **2008**, 34, 68–76; (c) J. Elguero, F. H. Cano, C. Foces-Foces, A. L. Llamas-Saiz, H. Limbach, F. Aguilar-Parrilla, R. M. Claramunt, C. Ljpez, *J. Heterocycl. Chem.*, **1994**, 31, 695–700; (d) C. Foces-Foces, A. L. Llamas-Saiz, R. M. Claramunt, C. Ljpez, J. Elguero, *J. Chem. Soc. Chem. Commun.*, **1994**, 1143–1145; (e) J. Elguero, *Cryst. Growth Des.*, **2011**, 11, 4731–4738.
30. G. Cavallo, P. Metrangolo, R. Milani, T. Pilati, A. Priim-gi, G. Resnati, G. Terraneo, *Chem. Rev.*, **2016**, 116, 2478–2601.
31. E. Hadjoudis, M. Vittorakis, I. Moustakali-Mavridis, *Tetrahedron*, **1987**, 43, 1345–1360.
32. (a) C. M. Widdifield, G. Cavallo, G. A. Facey, T. Pilati, J. Lin, P. Metrangolo, G. Resnati, D. L. Bryce, *Chem. - A Eur. J.*, **2013**, 19, 11949–11962; (b) M. Baldrighi, D. Bartesaghi, G. Cavallo, M. R. Chierotti, R. Gobetto, P. Metrangolo, T. Pilati, G.

- Resnati, G. Terraneo, *CrystEngComm*, **2014**, 16, 5897–5904.
33. (a) R. Pettinari, F. Marchetti, C. Pettinari, F. Condello, B. W. Skelton, A. H. White, M. R. Chierotti, R. Gobetto, *Dalton Trans.*, **2016**, 45, 5404–5404; (b) M. R. Chierotti, R. Gobetto, *Chem. Commun.*, **2008**, 1621–1634; (c) I. Yavari, J. D. Roberts, *Magn. Reson. Chem.*, **1979**, 12, 87–91; (d) P. Cerreia Vioglio, M. R. Chierotti, R. Gobetto, *CrystEngComm*, **2016**, 18, 9173–9184.
34. K. Johmoto, A. Sekine, H. Uekusa, *Cryst. Growth Des.*, **2012**, 12, 4779–4786.
35. (a) G. M. Mercier, K. Robeyns, T. Leyssens, *Cryst. Growth Des.*, **2016**, 16, 3198–3205; (b) E. Hadjoudis, A. Rontoyianni, K. Ambroziak, T. Dziembowska, I. M. Mavridis, *J. Photochem. Photobiol. A Chem.*, **2004**, 162, 521–530.
36. J. W. Ledbetter, *J. Phys. Chem.*, **1966**, 70, 2245–2249.
37. A. Ségerie, F. Castet, M. B. Kanoun, A. Plaquet, V. Liégeois, B. Champagne, *Chem. Mater.*, **2011**, 23, 3993–4001.
38. (a) G. Kortüm, W. Braun, G. Herzog, *Angew. Chemie Int. Ed.* **1963**, 2, 333–341; (b) S. Taro, T. Kobayashi, T. Inabe, *J. Phys. Chem. A*, **1997**, 101, 644–649.
39. M. Sliwa, N. Mouton, C. Ruckebusch, S. Aloïse, O. Poizat, G. Buntinx, R. Métivier, K. Nakatani, H. Masuhara, T. Asahi, *J. Phys. Chem. C*, **2009**, 113, 11959–11968.
40. M. Sliwa, S. Létard, I. Malfant, M. Nierlich, P. G. Lacroix, T. Asahi, H. Masuhara, P. Yu, K. Nakatani, *Chem. Mater.*, **2005**, 17, 4727–4735; (b) D. Higelin, H. Sixl, *Chem. Phys.*, **1983**, 77, 391–400.
41. (a) M. Avadanei, V. Cozan, S. Shova, J. A. Paixão, *Chem. Phys.* **2014**, 444, 43–51; (b) D. A. Safin, M. G. Babashkina, K. Robeyns, Y. Garcia, *RSC Adv.* **2016**, 6, 53669–53678.
42. T. Haneda, M. Kawano, T. Kojima, M. Fujita, *Angew. Chemie Int. Ed.*, **2007**, 46, 6643–6645.
43. L. J. Farrugia, *J. Appl. Crystallogr.*, **2012**, 45, 849–854.
44. M. C. Burla, R. Caliandro, B. Carrozzini, G. L. Casciarano, C. Cuocci, C. Giacovazzo, M. Mallamo, A. Mazzone, G. Polidori, *J. Appl. Crystallogr.*, **2015**, 48, 306–309.
45. G. M. Sheldrick, *Acta Crystallogr. Sect. C*, **2015**, 71, 3–8.
46. A. L. Spek, *J. Appl. Crystallogr.*, **2003**, 36, 7–13.

47. C. F. Macrae, I. J. Bruno, J. A. Chisholm, P. R. Edgington, P. McCabe, E. Pidcock, L. Rodriguez-Monge, R. Taylor, J. van de Streek, P. A. Wood, *J. Appl. Crystallogr.*, **2008**, 41, 466.
48. B. C. Gates, H. Knözinger, F. C. Jentoft, *Advances in Catalysis Vol. 52*, Academic Press, **2009**.
49. H. Ishida, S. Tobita, Y. Hasegawa, R. Katoh, K. Nozaki, *Coord. Chem. Rev.*, **2010**, 254, 2449–2458.

Appendix A

[2+2] photoreactions

Structural solution of [1H]NO₃ from powder diffraction data

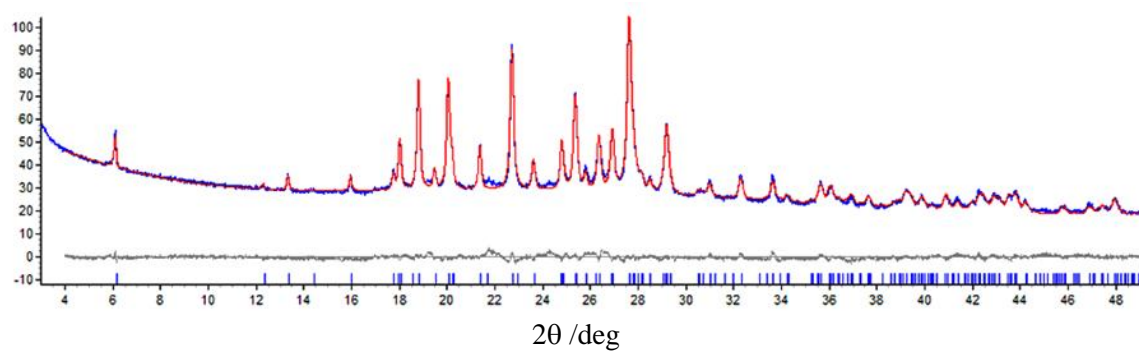


Figure A.1. Experimental (blue), calculated (red) and difference (grey) patterns for [1H]NO₃.

Crystallographic tables

Table A.1. Crystal data and details of measurements for crystalline [1H]₂SO₄·H₂O (I), [1H]BF₄ (I) and (II), [1H]PF₆, and [1H]NO₃.

	[1H] ₂ SO ₄ ·H ₂ O (I)	[1H]BF ₄ (I)	[1H]BF ₄ (II)	[1H]PF ₆	[1H]NO ₃ ^a
Formula	C ₁₈ H ₂₂ N ₂ O ₉ S	C ₉ H ₁₀ BF ₄ NO ₂	C ₉ H ₁₀ BF ₄ NO ₂	C ₉ H ₁₀ F ₃ NO ₂ P _{0.50}	C ₉ H ₁₀ N ₂ O ₅
Fw (g/mol)	442.44	250.99	250.99	236.67	226.06
Crystal System	Monoclinic	Monoclinic	Triclinic	Triclinic	Monoclinic
Space group	P2 ₁ /c	I2/a	P-1	P-1	P2 ₁ /c
Z	4	8	2	2	4
a (Å)	13.1014(6)	7.262(5)	7.2802(11)	5.5647(5)	5.14519(1)
b (Å)	11.7129(4)	10.026(5)	9.0670(15)	5.8519(8)	28.63202(6)
c (Å)	13.2735(6)	30.424(5)	9.7329(16)	15.8200(15)	7.01640(2)
α (deg)	90	90	115.130(16)	85.376(9)	90
β (deg)	100.385(4)	96.193(5)	100.802(13)	86.255(7)	104.50484(5)
γ (deg)	90	90	101.825(14)	72.178(10)	90
V (Å ³)	2003.52(15)	2202.2(19)	541.32(15)	488.40(9)	1000.699(1)
T(K)	293	293	293	293	293
Dcalc (g/cm ³)	1.467	1.514	1.540	1.609	-
μ (mm ⁻¹)	0.217	0.148	0.150	0.227	-
Measd reflns	9219	5174	4239	3631	-
Indep reflns	4638	2496	2441	2181	-
R ₁	0.0751	0.0650	0.0857	0.0703	-
wR ₂ (all data)	0.2440	0.1385	0.2686	0.1832	-
Rwp	-	-	-	-	5.1
Rexp	-	-	-	-	3.4
χ ²	-	-	-	-	1.5

^a Structural solution from powder data.

Table A.2. Crystal data and details of measurements for crystalline [1H]Cl at each stage of its photodimerisation.

	[1H]Cl	[1H]Cl 86%	[1H]Cl 80%	[1H]Cl 74%	[1H]Cl 68%	[1H]Cl 51%	[1H]Cl 41%	[1H]Cl 37%	[1H]Cl 25%	[1H]Cl 0%
Formula	C ₉ H ₁₀ ClNO ₂									
Fw (g/mol)	199.63	199.63	199.63	199.63	199.63	199.63	199.63	199.63	199.63	199.63
Crystal System	Monoclinic									
Space group	P2 ₁ /c									
Z	4	4	4	4	4	4	4	4	4	4
a (Å)	5.5837(7)	5.6063(2)	5.6180(3)	5.6294(5)	5.6409(5)	5.6523(7)	5.6523(7)	5.6907(5)	5.7167(6)	5.7431(17)
b (Å)	8.5339(10)	8.5811(7)	8.5855(7)	8.5824(8)	8.5631(8)	8.5616(14)	8.5616(14)	8.4732(18)	8.417(2)	8.221(3)
c (Å)	19.865(2)	19.4662(17)	19.373(2)	19.252(3)	19.131(3)	19.105(5)	19.105(5)	18.860(3)	18.889(3)	19.012(6)
α (deg)	90	90	90	90	90	90	90	90	90	90
β (deg)	92.074(11)	91.595(7)	91.521(7)	91.427(9)	91.475(10)	91.471(17)	91.471(17)	91.741(9)	91.904(10)	92.47(3)
γ (deg)	90	90	90	90	90	90	90	90	90	90
V (Å ³)	946.0(2)	936.12(12)	934.08(15)	929.83(19)	923.78(19)	924.3(3)	913.1(2)	909.0(2)	908.4(3)	896.8(5)
T(K)	293	293	293	293	293	293	293	293	293	293
Dcalc (g/cm ³)	1.402	1.416	1.420	1.426	1.435	1.435	1.452	1.459	1.460	1.479
μ (mm ⁻¹)	0.369	0.373	0.374	0.375	0.378	0.378	0.382	0.384	0.384	0.389
Measd reflns	3904	4265	4165	3487	10461	3256	8472	3408	3420	6135
Indep reflns	2155	2145	2131	1584	2304	1580	1561	1554	1551	2136
R1	0.0700	0.0948	0.0925	0.0854	0.0877	0.1149	0.0875	0.1019	0.1034	0.1088
wR2 (all data)	0.1218	0.2018	0.1923	0.1914	0.2345	0.2367	0.2163	0.2266	0.2125	0.3918

Table A.3. Crystal data and details of measurements for crystalline [1H]₂SO₄·H₂O (II) at each stage of its photodimerisation.

	[1H] ₂ SO ₄ ·H ₂ O (II)	[1H] ₂ SO ₄ ·H ₂ O (II) 88%	[1H] ₂ SO ₄ ·H ₂ O (II) 70%	[1H] ₂ SO ₄ ·H ₂ O (II) 58%	[1H] ₂ SO ₄ ·H ₂ O (II) 27%	[1H] ₂ SO ₄ ·H ₂ O (II) 20%	[1H] ₂ SO ₄ ·H ₂ O (II) 0%
Formula	C ₁₈ H ₂₂ N ₂ O ₉ S	C ₁₈ H ₂₂ N ₂ O ₉ S	C ₁₈ H ₂₂ N ₂ O ₉ S	C ₁₈ H ₂₂ N ₂ O ₉ S	C ₁₈ H ₂₂ N ₂ O ₉ S	C ₁₈ H ₂₂ N ₂ O ₉ S	C ₁₈ H ₂₂ N ₂ O ₉ S
Fw (g/mol)	442.44	442.44	442.44	442.44	442.44	442.44	442.44
Cryst. System	Triclinic						
Space group	P-1						
Z	2	2	2	2	2	2	2
a (Å)	7.3374(8)	7.3066(9)	7.2590(10)	7.2497(10)	7.1238(19)	7.0960(5)	7.0956(7)
b (Å)	10.5566(12)	10.5681(17)	10.5719(15)	10.6164(17)	10.631(2)	10.6518(9)	10.6597(13)
c (Å)	13.8798(15)	13.8909(16)	13.8895(18)	13.902(2)	13.925(3)	13.9338(12)	13.9430(15)
α (deg)	103.793(10)	104.253(12)	104.423(12)	104.762(14)	106.010(17)	106.307(8)	106.348(10)
β (deg)	99.924(9)	99.577(10)	98.792(11)	98.258(13)	95.898(18)	95.377(7)	95.271(9)
γ (deg)	102.838(10)	102.609(12)	102.601(12)	102.574(13)	102.081(19)	101.948(7)	101.923(10)
V (Å ³)	988.76(19)	986.7(2)	982.9(2)	987.2(3)	976.7(4)	975.91(14)	977.41(19)
T(K)	293	293	293	293	293	293	293
D _{calc} (g/cm ³)	1.486	1.489	1.495	1.488	1.504	1.506	1.503
μ (mm ⁻¹)	0.219	0.220	0.221	0.220	0.222	0.222	0.222
Measd reflns	8036	7514	7771	7361	7796	14762	7914
Indep reflns	4494	4446	4480	4469	4453	4647	4462
R ₁	0.0681	0.0788	0.1020	0.1236	0.1032	0.1009	0.1076
wR ₂ (all data)	0.1686	0.2483	0.3671	0.4059	0.3381	0.3155	0.2698

X-Ray powder diffraction

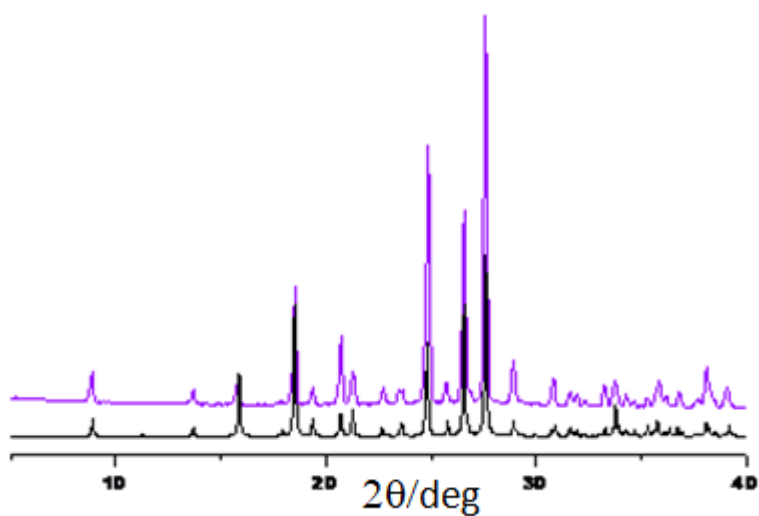


Figure A.2. Experimental (violet pattern) and simulated (black pattern) X-ray powder diffraction patterns for $[1H]Cl$.

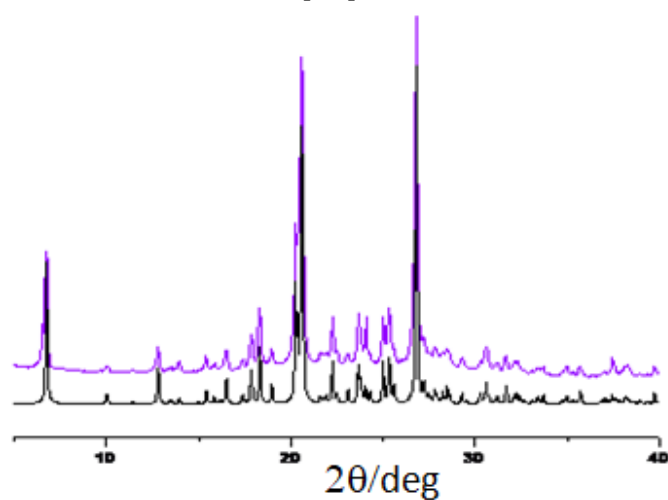


Figure A.3. Experimental (violet line) and simulated (black line) X-ray powder diffraction patterns for $[1H]_2[SO_4] \cdot H_2O$ (I).

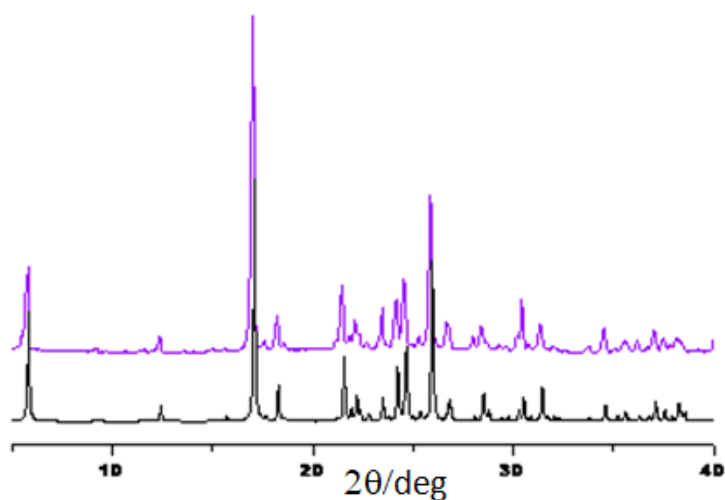


Figure A.4. Experimental (violet line) and simulated (black line) X-ray powder diffraction patterns for $[1H]BF_4$ (I).

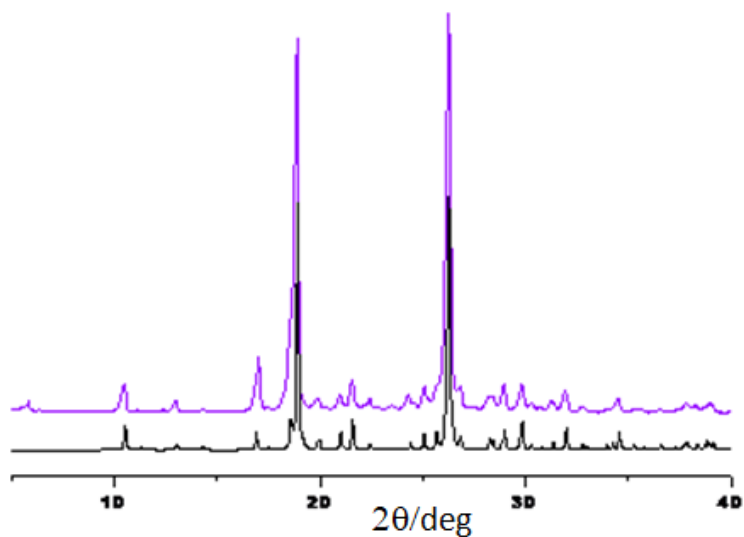


Figure A.5. Experimental (violet line) and simulated (black line) X-ray powder diffraction patterns for $[1H]BF_4$ (II).

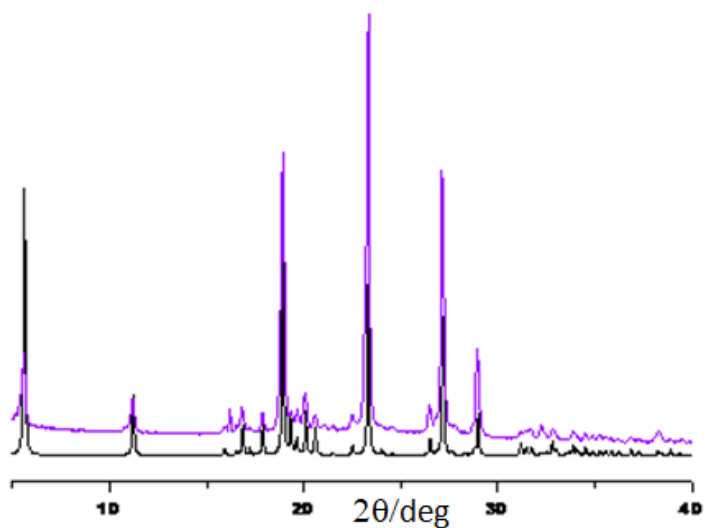


Figure A.6. Experimental (violet line) and simulated (black line) X-ray powder diffraction patterns $[1H]PF_6$.

[4+4] photoreactions

Crystallisation of MAMA from gel

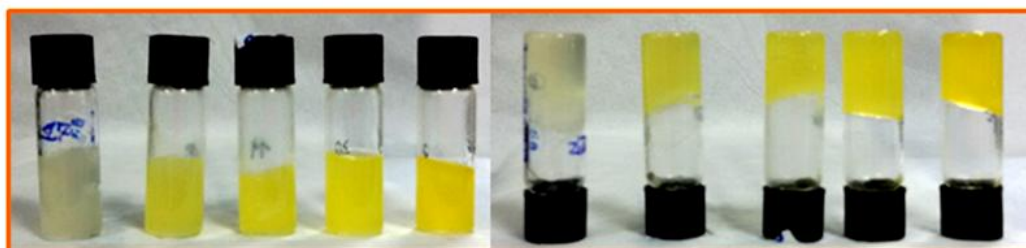


Figure A.7. Crystallisation of MAMA from bis-urea derivative low molecular weight gelator. Unluckily, no crystals have been obtained.

Solution of MAMA from powder diffraction data

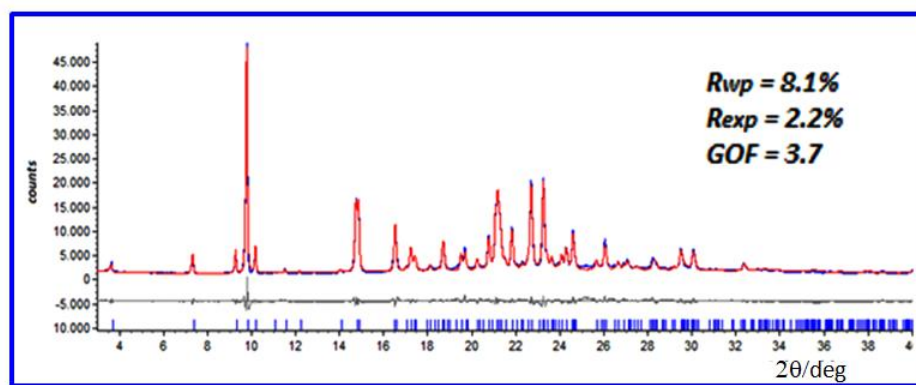


Figure A.8. Final Rietveld refinement of MAMA: calculated (red), experimental (blue) and difference (grey) patterns.

Crystallographic data**Table A.4.** Crystal data and details of measurements for crystalline MAMA, DMAMA, Ag(MAMA)₂[PF₆], Ag(MAMA)₂[BF₄], [Ag(MAMA)₂][Ag(NO₃)₂], and [DMAMAH₂]Br₂.

	MAMA ^a	DMAMA	[Ag(MAMA)₂][PF₆]	[Ag(MAMA)₂][BF₄]	[Ag(MAMA)₂][Ag(NO₃)₂]	[DMAMAH₂]Br₂
Formula	C ₁₅ H ₁₆ N	C ₁₆ H ₁₅ N	C ₃₂ H ₃₀ AgF ₆ NP	C ₃₂ H ₃₀ AgBF ₄ N	C ₁₆ H ₁₅ AgN ₂ O ₃	C ₃₂ H ₃₂ Br ₂ N ₂
Fw (g/mol)	221.30	221.29	695.42	637.28	391.17	604.42
Crystal System	Triclinic	Triclinic	Monoclinic	Monoclinic	Monoclinic	Monoclinic
Space group	P-1	P-1	C2/c	C2/c	C2/c	P2 ₁ /n
Z	2	2	8	8	8	4
Z'	2	2 x 0.5	0.5	0.5	0.5	0.5
a (Å)	24.1250(1)	8.1706(5)	19.4884(9)	18.6597(9)	20.4242(12)	9.202(5)
b (Å)	9.65362(3)	9.2479(6)	10.4542(4)	10.2048(4)	8.1480(4)	7.953(5)
c (Å)	5.48188(2)	16.4024(10)	14.4045(9)	14.7676(8)	18.6493(13)	18.223(5)
α (deg)	100.5596(4)	92.8970(10)	90	90	90	90
β (deg)	96.2248(5)	93.1560(10)	96.753(5)	100.540(5)	108.776(7)	93.342(5)
γ (deg)	85.6998(3)	110.3720(10)	90	90	90	90
V (Å ³)	1245.69(5)	1156.88(13)	2914.3(3)	2764.6(2)	2938.4(3)	1331.4(12)
T(K)	293	293	293	293	293	293

D_{calc} (g/cm ³)	1.180	1.271	1.585	1.531	1.768	1.508
μ (mm ⁻¹)	-	0.074	0.810	0.781	1.386	3.069
Measd reflns	-	18826	7545	6336	7363	5040
Indep reflns	-	6729	3379	3140	3375	2348
R_1	-	0.0555	0.083	0.0602	0.0786	0.0740
w R_2 (all data)	-	0.1639	0.204	0.222	0.1626	0.1003
R_{wp}	8.2	-	-	-	-	-
R_{exp}	2.1	-	-	-	-	-
GOF	3.7	1.069	1.126	0.978	1.119	0.916

a: solved by powder diffraction data.

X-Ray powder diffraction

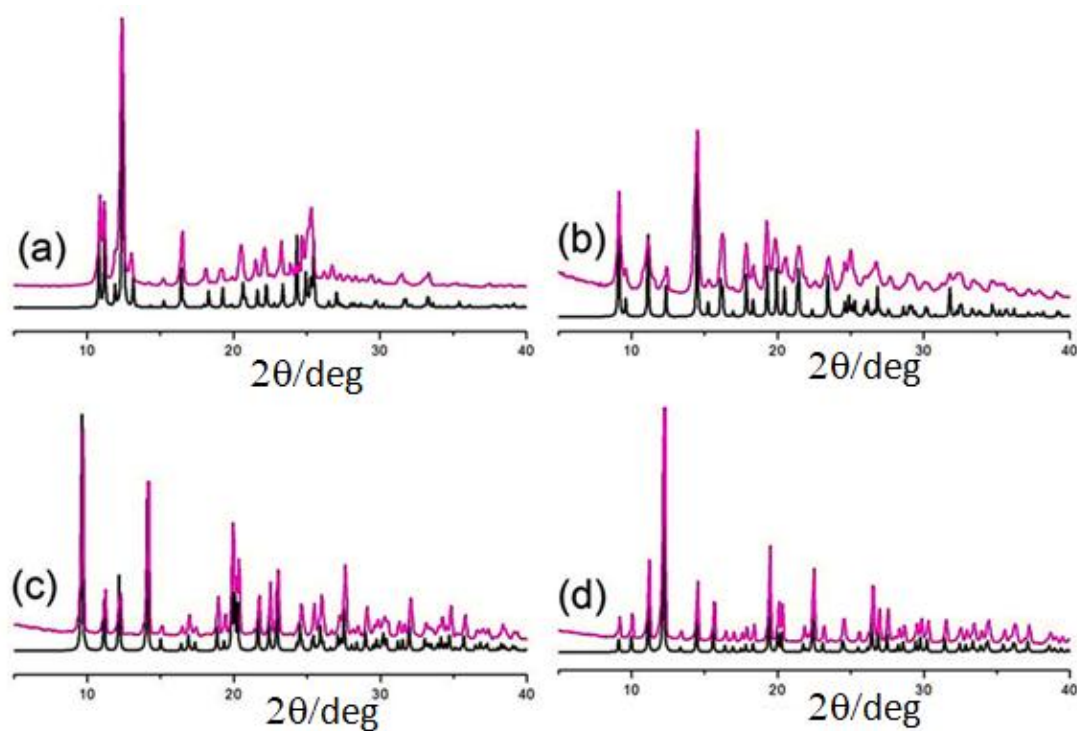


Figure A.9. Experimental (purple line) and simulated (black line) X-ray powder diffraction patterns for DMAMA (a), $[\text{Ag}(\text{MAMA})_2][\text{PF}_6]$ (b), $[\text{Ag}(\text{MAMA})_2][\text{BF}_4]$ (c) and $[\text{Ag}(\text{MAMA})_2][\text{Ag}(\text{NO}_3)_2]$ (d).

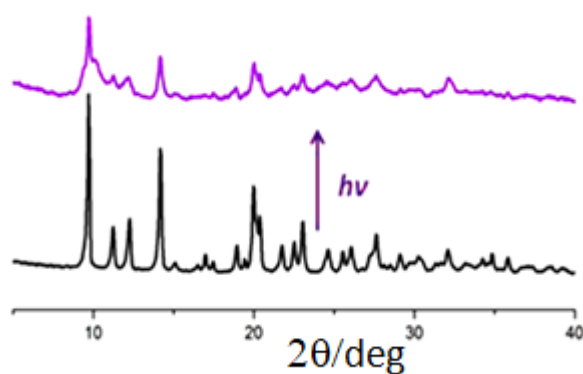


Figure A.10. Comparison between experimental XRPD patterns run before (black line) and after UV irradiation (violet line) for $[\text{Ag}(\text{MAMA})_2][\text{BF}_4]$.

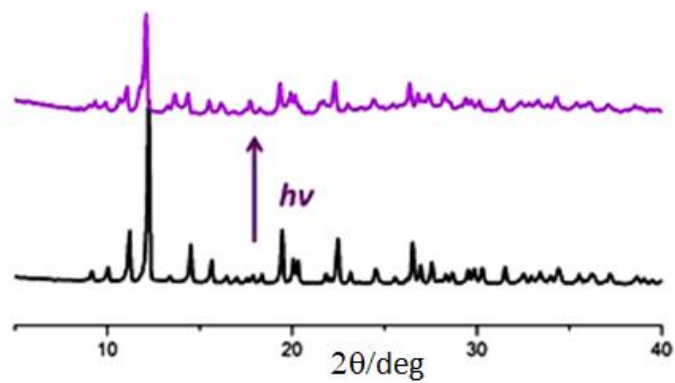


Figure A.11. Comparison between experimental XRPD patterns run before (black line) and after UV irradiation (violet line) for $[\text{Ag}(\text{MAMA})_2][\text{Ag}(\text{NO}_3)_2]$.

Raman spectroscopy

Table A.5. Main Raman band wavenumbers and assignments for MAMA and DMAMA. The band wavenumbers of dianthracene are reported for comparison.

The characteristic bands of fused benzene rings are highlighted in bold and those of the dimer are indicated in red.

Assignments	MAMA	DMAMA	Dianthracene ¹	Assignments
CC ring stretching in anthracene ^{2,3} , in alkyl-substituted anthracenes ⁴ , and 9-substituted derivatives ^{5,6}	1625 vw			
		1597-1591 m	1603-1592	Phenyl CC stretching in 9,10-dihydroanthracene ⁷ and ortho-xylene ^{8,9}
CC ring stretching in anthracene and 9-substituted derivatives ^{2,5,3}	1575 sh	1576 sh	1582	Phenyl CC stretching in dianthracene ¹ and 9,10-dihydroanthracene ⁷
CC ring stretching in anthracene and 9-substituted derivatives ^{2,5,3,6}	1558 s			
Aromatic CH in plane bending ⁵ and CC ring stretching ⁶ in anthracene ¹⁰ and 9-substituted derivatives	1503-1493 w			
CC ring stretching in anthracene and 9-substituted derivatives ^{2,5} , aromatic CH in plane bending in anthracene ^{5,3}	1477 m	1479 mw	1464	Phenyl CC stretching in 9,10-dihydroanthracene ⁷
CH ₃ symmetric deformation ⁸	1453 w	1453 w		
CC ring stretching in anthracene ^{2,5,3} and 9-substituted anthracene ^{8,11} characteristic of fused benzene rings¹²	1408 vs	1410 w		
Aromatic CH in plane bending in anthracene ^{5,3} , CC ring stretching in 9-substituted anthracene ^{6,8,11} , CH ₃ antisymmetric deformation ^{8,6}	1381 m			
Aromatic CH in plane bending in anthracene and 9-substituted anthracene ⁵	1356 ms			
		1348 vw	1338	Tertiary CH deformation ⁸
Aromatic CH in plane bending in anthracene ^{5,3}	1278 m	1271 vw	1265	CH in plane bending in 9,10-dihydroanthracene ⁷
CC ring stretching ^{2,3} and aromatic CH in plane bending ⁵ in anthracene	1258 m	1261 sh	1263	CH out of phase bending in 9,10-dihydroanthracene ⁷
		1211 vs	1228	CC symmetric stretching in 9,10-dihydroanthracene ⁷ , ortho-dialkylbenzenes ^{8,9}
		1194 sh br	1187	CC antisymmetric stretching in 9,10-dihydroanthracene ⁷ , internal quaternary carbon atom ⁸
CH in plane bending in anthracene ^{2,5,3}	1181 m		1178	
		1167 mw	1158	Internal tertiary carbon atom ⁸
CH in plane bending in anthracene and 9-substituted anthracene ^{5,3,6} , aliphatic CH bending ^{6,8}	1155-1142 vw	1153-1141 vw		
Aromatic CH in plane bending ⁵ and CC ring stretching ³ in anthracene and 9-substituted anthracene	1101 vw			
		1085 w		CH bending out of phase in 9,10-dihydroanthracene ⁷ , aliphatic CC stretching ¹³
	1043 vw	1042 vs	1038	CH bending in plane in 9,10-dihydroanthracene ⁷ , phenyl ring stretching + deformation in 9,10-dihydroanthracene ¹⁴ , ortho-disubstituted benzene ⁸ , internal tertiary carbon atom ⁸
Aromatic CH in plane bending in anthracene ⁵	1020 m	1016 mw	1024	Phenyl ring breathing in 9,10-dihydroanthracene ¹⁴
Aromatic CH out of plane bending in anthracene ² , CC ring stretching + aliphatic CH out of plane wagging in 9-substituted anthracene ¹⁵	985 vw	989 mw	996	CH out of plane bending in 9,10-dihydroanthracene ⁷
Aromatic CH out of plane bending in anthracene and 9-substituted anthracene ^{5,3,6}	972 sh			
Aromatic CH out of plane bending ^{5,3} in anthracene and ring in plane bending ⁵ in 9-substituted anthracene	957 sh			
Aromatic CH out of plane bending in anthracene ⁵ , CH ₃ bending ⁶	949 w	951-938 vw	950	CH out of plane bending in 9,10-dihydroanthracene ⁷

Ring in plane bending ^{5,6} and aromatic CH out of plane bending ^{3,6} in 9-substituted anthracene	904 vw			
		898-888 m	890-885	Aliphatic CC stretching in dimers of anthracene derivatives ¹⁶ , skeletal bending in 9,10-dihydroanthracene ⁷
Aromatic CH out of plane bending ^{5,6} of the group approximately perpendicular to the longer axis of the anthracene molecule (i.e. at the 10 position) ¹⁷	879 w			
Aromatic CH out of plane bending in anthracene and 9-substituted anthracene ^{5,6}	866 w	869 vw		CH out of plane bending in 9,10-dihydroanthracene ⁷
Aromatic CH out of plane bending in anthracene ⁵ , CH ₂ bending ⁶	848 w	854 vw	851	CH out of plane bending in 9,10-dihydroanthracene ⁷
Ring in plane bending in anthracene ⁵ and aromatic CH out of plane bending in 9-substituted anthracene ⁶ , CH ₂ bending ^{6,8}	834 w	832 w, sh		
Ring in plane bending in anthracene ⁵	818 w	816 mw	820	Aliphatic CH out of plane bending in dianthracene ¹⁷
aromatic CH out of plane bending ³ of the groups approximately parallel to the longer axis of the anthracene molecule (i.e. no 10 position) ¹⁷	750 w	750 mw	760	CH out of plane bending in 9,10-dihydroanthracene ⁷ and ortho-disubstituted benzene ¹⁷
aromatic CH out of plane bending in anthracene ^{5,17} ; ring out of plane bending in 9-substituted anthracene ^{5,15}	733 w br			
Ring in plane bending in anthracene ²	703 m	701 m	711	
Ring in plane bending in anthracene and 9-substituted anthracene ^{5,6}	693 m			
		685 m		Ring torsion in anthrone ¹³
Ring in plane bending in anthracene ^{2,5}	637 vw	636-627 w	637	
Ring out of plane bending ³ and ring torsion ⁵ in anthracene	576 vw	571 w	584	Ring in plane bending in ortho-xylene ^{8,18}
Ring in plane bending in 9-substituted anthracene ⁶	548 w	555 w	555	
Ring in plane bending in anthracene ²	535 vw	528 w		Skeletal bending in 9,10-dihydroanthracene ⁷
Ring in plane bending in anthracene ^{2,5}	520 w	513 w	516	Phenyl out of phase bending in 9,10-dihydroanthracene ⁷
Ring torsion ^{5,6} , ring out of plane bending ³ in anthracene and 9-substituted anthracene	476 w			
		445 w		Ring deformation in ortho-xylene ¹⁸ , internal tertiary carbon atom ⁸
Ring in plane bending in 9-methyl anthracene ^{8,18}	421 ms			
		406 m		Phenyl out of plane bending in 9,10-dihydroanthracene ⁷
Ring bending in plane ^{2,5,6} , ring torsion ⁶ , in 9-methyl anthracene ^{8,18} characteristic of fused benzene rings¹²	394 ms			
Ring out of plane bending in anthracene ²	366 w	365 m	361	Skeletal bending in 9,10-dihydroanthracene ⁷
ring torsion in 9-substituted anthracene ⁶	334 w	332 sh		
		326 s	327	CC deformation in dianthracene ¹
Ring torsion ⁵ and ring out of plane bending ³ in anthracene	237 w	242 w		Ring out of phase flapping in 9,10-dihydroanthracene ⁷
Ring out of plane bending in anthracene ² , ring torsion in 9-substituted ⁶	214 vw			
		153 vs		Lattice modes in dianthracene ¹ , central ring in plane bending in 9,10-dihydroanthracene ⁷
Ring torsion in anthracene ⁵ , CC bending in plane in 9-methyl anthracene ¹⁸	148 w			
		137 vs	141	Lattice modes in dianthracene ¹
Ring torsion in anthracene and 9-substituted anthracene ^{5,6}	105 s	116 s	110	Lattice modes in dianthracene ¹
	74 vs	75 vs	71	Lattice modes in dianthracene ¹

v = very; w = weak; m = medium; s = strong; br = broad; sh = shoulder

Figures A.12 - 14 show the Raman spectra of the $[\text{Ag}(\text{MAMA})_2][\text{BF}_4]$, $[\text{Ag}(\text{MAMA})_2][\text{PF}_6]$ and $[\text{Ag}(\text{MAMA})_2][\text{Ag}(\text{NO}_3)_2]$ complexes, respectively, and the Raman spectrum of MAMA is reported as comparison. Upon coordination, similar changes were observed in the spectra of the complexes, while some bands are specifically assignable to the different counterions,¹⁹ as indicated in the figures; with regards to $[\text{Ag}(\text{MAMA})_2][\text{Ag}(\text{NO}_3)_2]$ (Figure A.15), the strengthening of the band at 1477 cm^{-1} is assignable to the contribution of the $\text{N}=\text{O}$ stretching mode and is a marker of the NO_3^- bidentate coordination.²⁰

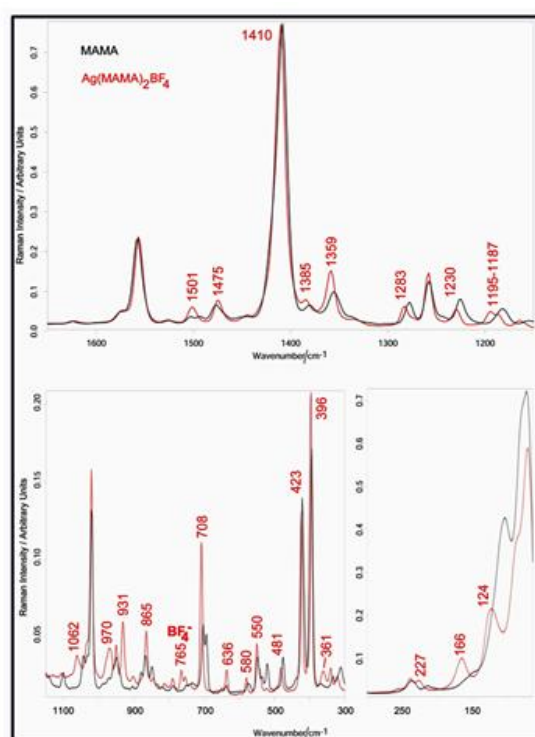


Figure A.12. Raman spectra of MAMA (black) and $[\text{Ag}(\text{MAMA})_2][\text{BF}_4]$ (red). The band assignable to the BF_4^- ion has been indicated (765 cm^{-1} : FBF symmetric stretching).

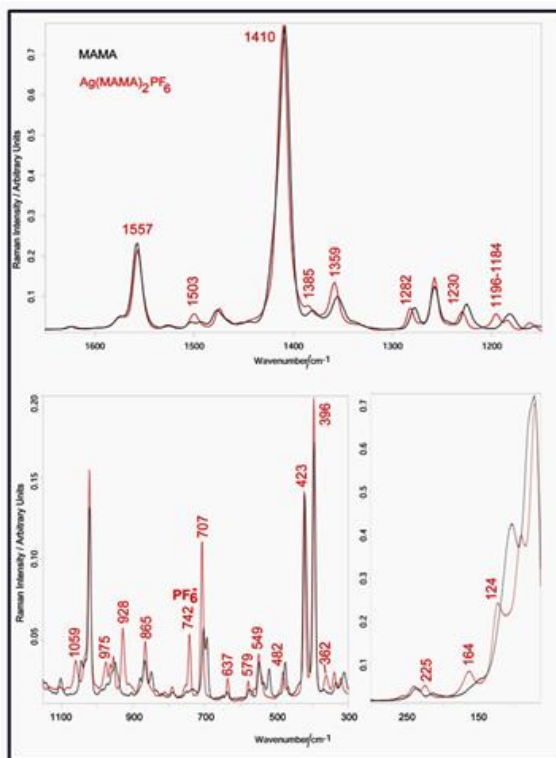


Figure A.13. Raman spectra of MAMA (black) and $[\text{Ag}(\text{MAMA})_2][\text{PF}_6]$ (red). The band assignable to the PF_6^- ion has been indicated (742 cm^{-1} : FPF symmetric stretching).

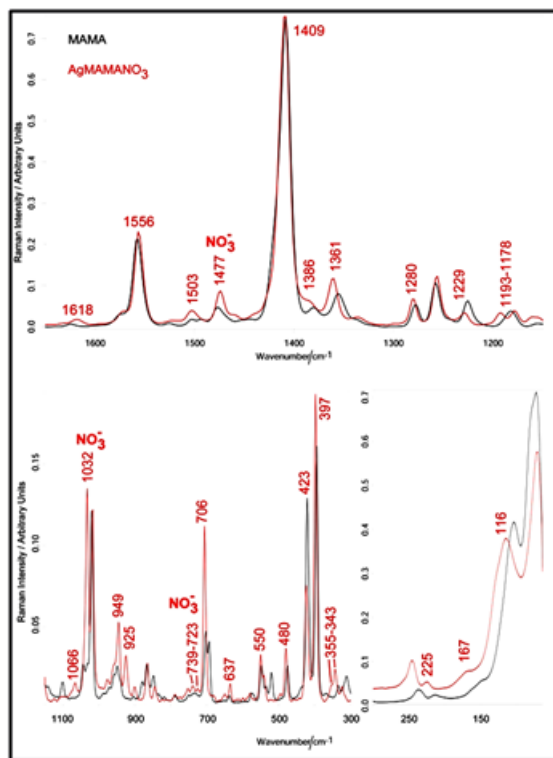
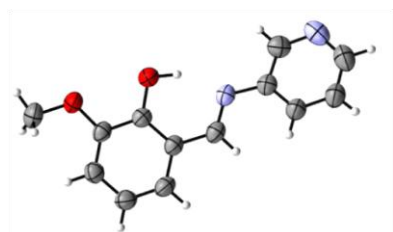


Figure A.14. Raman spectra of MAMA (black) and $[\text{Ag}(\text{MAMA})_2][\text{NO}_3]$ (red). The bands assignable to the NO_3^- ion have been indicated (1477 cm^{-1} : N=O stretching in bidentate NO_3^- ; 1032 cm^{-1} : ONO symmetric stretching; $739\text{-}723\text{ cm}^{-1}$: in plane NO_3^- deformation).

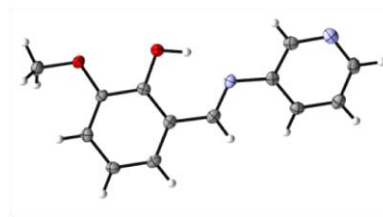
References:

1. Y. Ebisuzaki, T. J. Taylor, J. T. Woo, M. Nicol., *J. Chem. Soc.*, **1977**, 73, 253-264.
2. N. Abasbegović, N. Vukotić, L. Colombo, *J. Chem. Phys.*, **1964**, 41, 2575-2577.
3. J. Räsänen, F. Stenman, E. Penttinen, *Spectrochim. Acta A*, **1973**, 29, 395-403.
4. L.H. Colthup, S.E. Daly, Wiberley. Introduction to Infrared and Raman Spectroscopy. 3rd Edition, Academic Press, San Diego, **1990**.
5. A. Alparone, V. Librando, *Spectrochim. Acta A*, **2012**, 89, 129-136.
6. Y. S. Mary, H. T. Varghese, C. Y. Panicker, T. Thiemann, A. A. Al-Saadi, S. A. Popoola, C. Van Alsenoy, Y. Al Jasem, *Spectrochim. Acta A*, **2015**, 150, 533-542.
7. K. Morris, J. Laane, *J. Mol. Struct.*, **1997**, 13-20, 413-414.
8. F. R. Dollish, W. G. Fateley, F.F. Bentley, Characteristic Raman frequencies of organic compounds. Wiley-Interscience, Chichester, **1974**.
9. K.S. Pitzer, D.W. Scott., *J. Am. Chem. Soc.*, **1943**, 65, 803-829.
10. W.F. Maddams, I.A.M. Royaud. *Spectrochim. Acta A*, **1990**, 46, 309-314.
11. M. Brigodiot, J. M. Lebas, *Spectrochim. Acta A*, **1971**, 27, 1325-1336.
12. I. López-Tocón, J. C. Otero, J. F. Arenas, J. V. Garcia-Ramos, S. Sanchez-Cortes Anal. Chem., **2011**, 83, 2518-2525.
13. Y. S. Mary, T.S. Yamuna, C. Yohannan Panicker, H.S. Yathirajan, M.S. Siddegowda, A. A. Al-Saadi, C. Van Alsenoy, J. A. War, *Spectrochim. Acta A*, **2015**, 135, 652-661.
14. M. Brigodiot, J. M. Lebas, *J. Mol. Struct.*, **1976**, 32, 297-309.
15. S. Kou, H. Zhou, G. Tang, Rongqing Li, Y. Zhang, J. Zhao, C. Wei, *Spectrochim. Acta A*, **2012**, 96, 768-775.
16. L. Opilik, P. Payamyar, J. Szczerbinski, A. P. Schütz, M. Servalli, T. Hungerland, A. Dieter Schlüter, R. Zenobi, *ACS Nano*, **2015**, 9, 4252-4259.
17. S. Singh, C. Sandorfy, *Can. J. Chem.*, **1969**, 47, 257-263.
18. M. Brigodiot, J. M. Lebas, *Spectrochim. Acta A*, **1971**, 27, 1315-1324.
19. (a) K. Nakamoto. Infrared and Raman spectra of inorganic and coordination compounds. Part A: Theory and Applications in Inorganic Chemistry. 5th Edition. Wiley Inter-Science, New York, **1997**; (b) R. A. Nyquist, C. L. Putzig and M. A. Leugers. Handbook of Infrared and Raman spectra of inorganic compounds and organic salts. Academic Press San Diego, **1997**.
20. K. Nakamoto. Infrared and Raman spectra of inorganic and coordination compounds. Part B: Applications in Coordination, organometallic and Bioinorganic Chemistry. 5th Edition. Wiley Inter-Science, New York, **1997**.

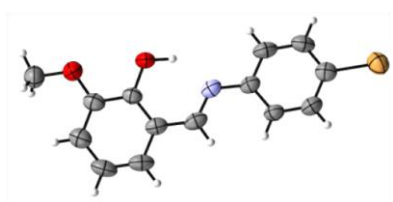
Appendix B



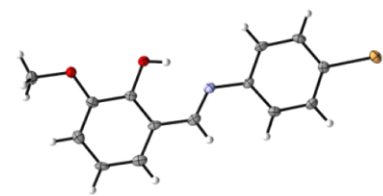
1 (RT)



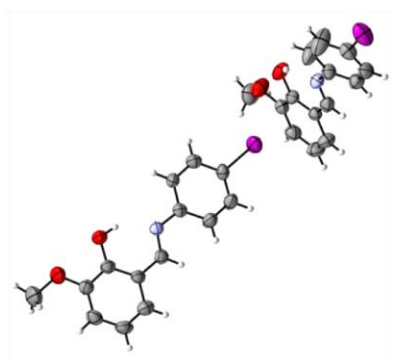
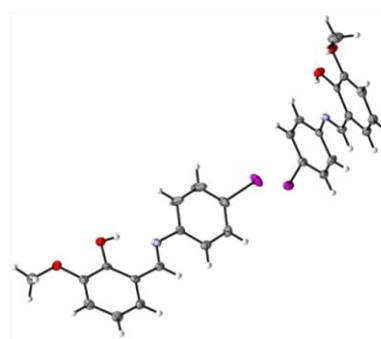
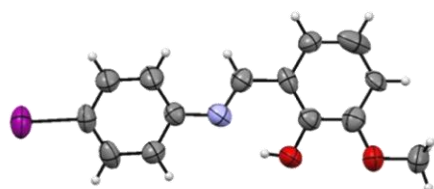
1 (LT)



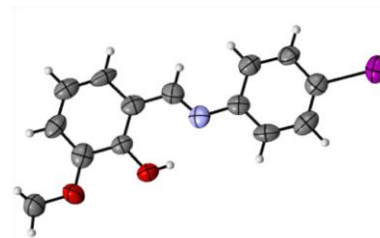
2 (RT)



2 (LT)

 3_{solv} (RT) 3_{solv} (LT)

3A (main image of disorder)



3B (RT), isomorphous with 2

Figure B.1. ORTEP diagrams for the pure molecular solids 1-3, at room and low temperature.

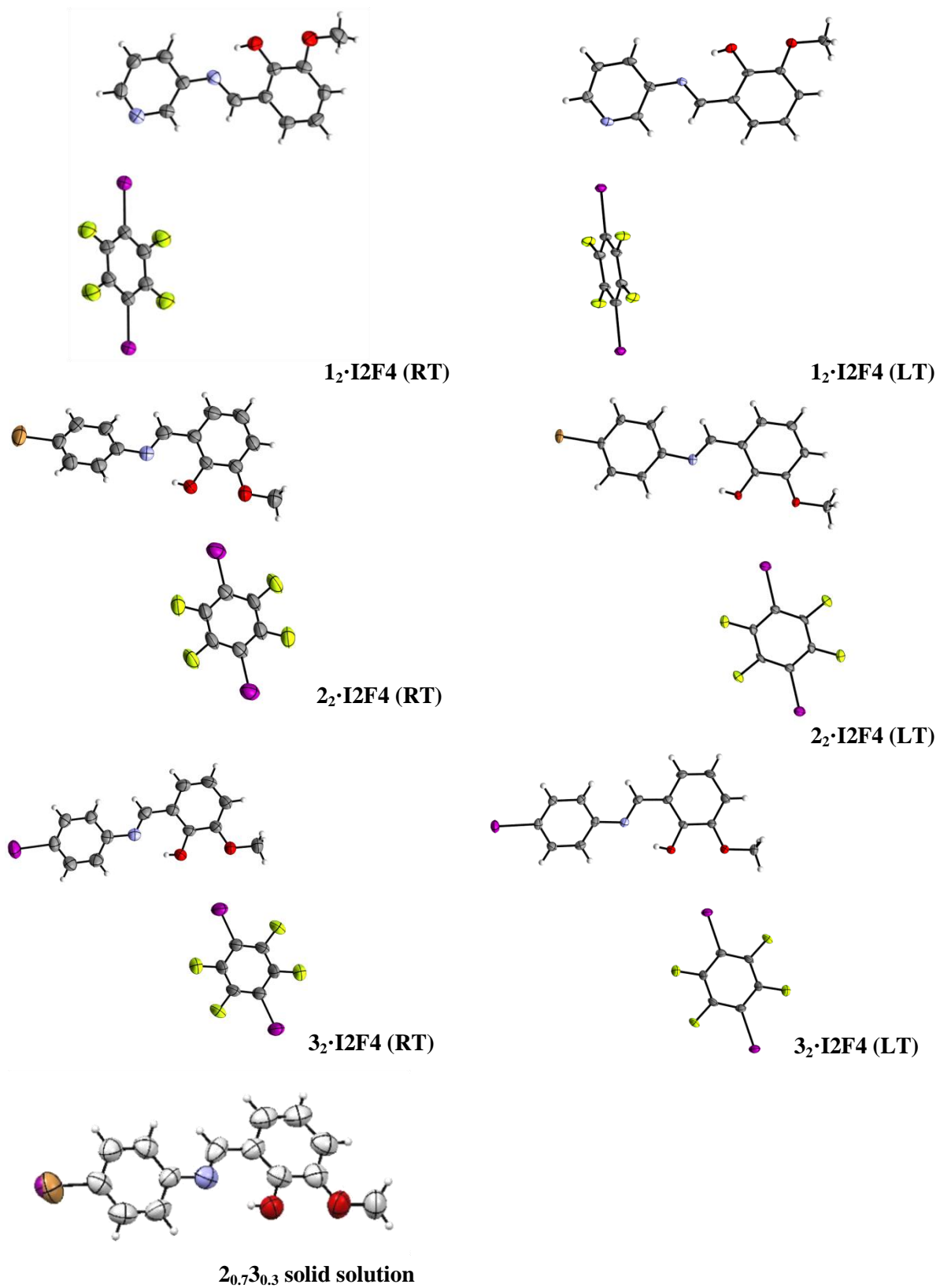


Figure B.2. ORTEP diagrams for the co-crystals of **1-3** with the co-former **I₂F₄**.

Table B.1. Crystal data and details of measurements for crystalline **1**, **2** and **3_{solv}** at room and low temperature.

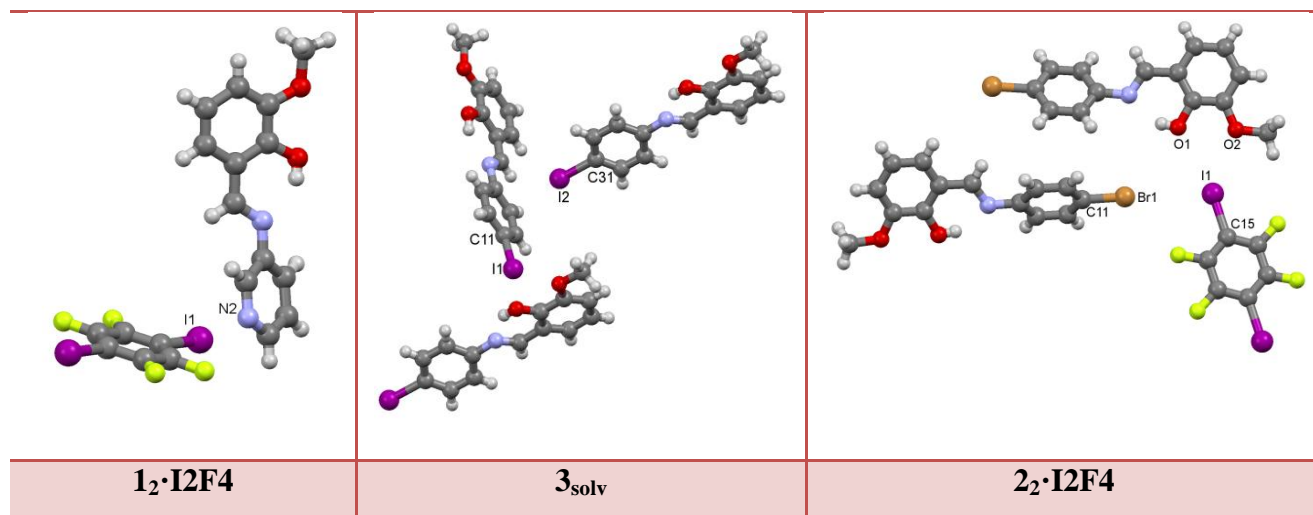
	1 (RT)	2 (RT)	3_{solv} (RT)	1 (LT)	2 (LT)	3_{solv} (LT)
Formula	C ₁₃ H ₁₂ N ₂ O ₂	C ₁₄ H ₁₂ BrNO ₂	C ₁₄ H ₁₂ INO ₂	C ₁₃ H ₁₂ N ₂ O ₂	C ₁₄ H ₁₂ BrNO ₂	C ₁₄ H ₁₂ INO ₂
Fw (g/mol)	228.25	306.16	353.15	228.25	306.16	353.15
Crystal system	Orthorhombic	Orthorhombic	Triclinic	Orthorhombic	Orthorhombic	Triclinic
Space group	P2 ₁ 2 ₁ 2 ₁	P2 ₁ 2 ₁ 2 ₁	P-1	P2 ₁ 2 ₁ 2 ₁	P2 ₁ 2 ₁ 2 ₁	P-1
a (Å)	5.6190(4)	4.9234(2)	11.2134(6)	5.5415(4)	4.8229(3)	11.0853(4)
Z	4	4	4	4	4	4
b (Å)	9.2825(7)	12.5234(8)	12.4384(7)	9.197(3)	12.5498(11)	12.2243(6)
c (Å)	21.7490(14)	20.5990(11)	12.7482(8)	21.5766(15)	20.3554(10)	12.4559(5)
α (deg)	90	90	109.977(4)	90	90	110.222(3)
β (deg)	90	90	108.168(5)	90	90	106.487(4)
γ (deg)	90	90	103.656(6)	90	90	102.947(5)
V (Å ³)	1134.39(14)	1270.09(12)	1466.26(19)	1099.7(4)	1232.04(15)	1418.06(13)
Crystal size (mm)	0.20 x 0.40 x 0.54	0.35 x 0.38 x 0.58	0.17 x 0.28 x 0.50	0.20 x 0.45 x 0.55	0.55, 0.30, 0.18	0.25 x 0.45 x 0.53
T (K)	293	293	293	108	147	108
Nref	1983	2222	5164	1783	2091	4984
Npar	160	168	329	159	168	335
R ₁	0.0321	0.0408	0.0432	0.0347	0.0244	0.0269
GoF	1.03	1.07	1.03	1.08	1.070	1.04
wR ₂ (all data)	0.0791	0.0855	0.1038	0.0796	0.0479	0.0695

Table B.2. Crystal data and details of measurements for crystalline **3A**, **3B** and **2_{0.7}3_{0.3}**.

	3A	3B	2_{0.7}3_{0.3}
Formula	C ₁₄ H ₁₂ INO ₂	C ₁₄ H ₁₂ INO ₂	C ₁₄ H ₁₂ Br _{0.70} I _{0.30} NO ₂
Fw (g/mol)	353.16	353.15	320.25
Crystal system	Monoclinic	Orthorhombic	Orthorhombic
Space group	P2 ₁ /c	P2 ₁ 2 ₁ 2 ₁	P2 ₁ 2 ₁ 2 ₁
Z	4	4	4
a (Å)	12.3849(11)	4.958(5)	4.9488(5)
b (Å)	16.7076(10)	12.518(5)	12.5366(13)
c (Å)	6.6782(5)	21.479(5)	20.993(2)
α (°)	90	90	90
β (°)	104.83	90	90
γ (°)	90	90	90
V (Å ³)	1335.78(17)	1333.1(15)	1302.5(2)
Crystal size (mm)	0.05 x 0.04 x 0.03	0.1 x 0.05 x 0.04	0.05 x 0.04 x 0.03
T(K)	293	293	293
Nref	2783	2647	2968
Npar	194	166	175
R ₁	0.0559	0.0605	0.0725
GoF	0.979	1.130	1.016
wR ₂	0.1784	0.1702	0.2225

Table B.3. Crystal data and details of measurements for crystalline **1₂·I2F4**, **2₂·I2F4** and **3₂·I2F4** at room and low temperature.

	1₂·I2F4 (RT)	2₂·I2F4 (RT)	3₂·I2F4 (RT)	1₂·I2F4 (LT)	2₂·I2F4 (LT)	3₂·I2F4 (LT)
Empirical formula	C ₁₃ H ₁₂ N ₂ O ₂ , 0.5(C ₆ F ₄ I ₂)	C ₁₄ H ₁₂ BrNO ₂ , 0.5(C ₆ F ₄ I ₂)	C ₁₄ H ₁₂ INO ₂ , 0.5(C ₆ F ₄ I ₂)	C ₁₃ H ₁₂ N ₂ O ₂ , 0.5(C ₆ F ₄ I ₂)	C ₁₄ H ₁₂ BrNO ₂ , 0.5(C ₆ F ₄ I ₂)	C ₁₄ H ₁₂ INO ₂ , 0.5(C ₆ F ₄ I ₂)
Fw (g/mol)	429.18	507.09	554.08	429.18	507.09	554.08
Crystal system	Monoclinic	Monoclinic	Monoclinic	Monoclinic	Monoclinic	Monoclinic
Space group	P2 ₁ /n	P2 ₁ /n	P2 ₁ /n	P2 ₁ /n	P2 ₁ /n	P2 ₁ /n
Z	4	4	4	4	4	4
a (Å)	4.6502(3)	7.1058(5)	7.5577(4)	4.6036(3)	7.0795(3)	7.6958(3)
b (Å)	28.0826(19)	9.4229(7)	9.2626(4)	27.982(2)	9.3289(4)	9.0189(3)
c (Å)	12.1429(8)	26.348(2)	25.9451(17)	12.0308(6)	25.9574(12)	25.5175(11)
α (deg)	90	90	90	90	90	90
β (deg)	94.695(6)	93.649(8)	96.577(5)	96.165(5)	93.004(4)	98.428(4)
γ (deg)	90	90	90	90	90	90
V (Å ³)	1580.42(18)	1760.6(2)	1804.31(17)	1540.82(17)	1711.97(13)	1751.98(12)
Crystal size (mm)	0.10 x 0.20 x 0.35	0.15 x 0.29 x 0.56	0.17 x 0.50 x 0.60	0.05 x 0.25 x 0.60	0.20 x 0.34 x 0.60	0.28 x 0.37 x 0.60
T(K)	293	293	293	115	105	150
Nref	2795	3102	3159	2724	3014	3001
Npar	210	223	222	213	222	222
R1	0.0409	0.0411	0.0374	0.0574	0.0281	0.0211
GoF	1.11	1.08	1.09	1.12	1.00	1.30
wR ²	0.0805	0.0978	0.0869	0.1451	0.0616	0.0527

Table B.4. Selected parameters for halogen bonds.

	Halogen...halogen interaction (type II)				Halogen bond		
	Contact type	X...X distance (Å)	$\theta 1$ (deg) (C11-X...I)	$\theta 2$ (deg) (X...I-C15)	Contact type	A...I distance (Å) (A = O, N)	A...I-C angle (deg) (A = O, N)
$1_2 \cdot I_2F_4$	/	/	/	/	I1...N2	2.878(4)	168.9
$1_2 \cdot I_2F_4$ (LT)	/	/	/	/	I1...N2	2.855(6)	168.5
$2_2 \cdot I_2F_4$	I1...Br1	3.9239(9)	173.4	106.5	I1...O1 I1...O2	3.447(4) 3.263(4)	169.1 141.3
$2_2 \cdot I_2F_4$ (LT)	I1...Br1	3.8775(6)	173.8	107.5	I1...O1 I1...O2	3.442(2) 3.208(2)	169.0 141.6
$3_2 \cdot I_2F_4$	I2...I1	3.9568(7)	173.5	108.4	I2...O1 I2...O2	3.501(3) 3.243(3)	169.3 145.1
$3_2 \cdot I_2F_4$ (LT)	I2...I1	3.8810(5)	172.3	107.8	I2...O1 I2...O2	3.488(2) 3.198(2)	168.8 145.5
C-I...π halogen bond							
	Contact type	I...Cg distance (Å)	C...Cg distance (Å)	C-I...Cg angle (deg)			
3_{solv}	C31-I2...Cg1	3.56	5.66	178.7			
	C11-I1...Cg2	3.57	5.63	166.5			
3_{solv} (LT)	C31-I2...Cg1	3.46	5.56	177.7			
	C11-I1...Cg2	3.46	5.52	160.3			
Cg1 = calculated at C8-C13 six-membered ring (molecule A) Cg2 = calculated at C21-C27 bond (molecule A)							

XRPD

Figures B.3 and B.4 show a comparison of chemical and structural identity between bulk materials and single crystals by comparing simulated and experimental powder diffraction patterns.

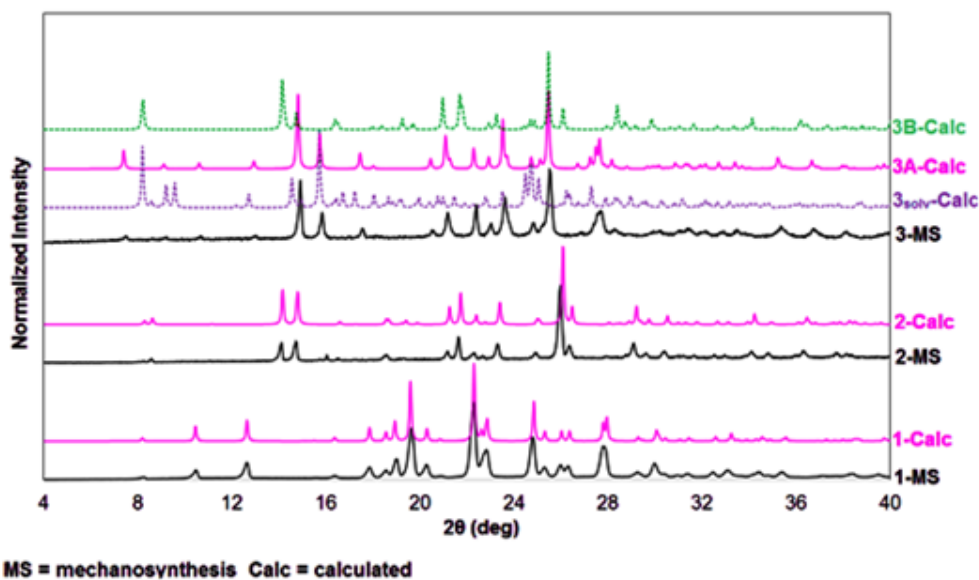


Figure B.3. XRPD comparison between calculated (calc) and experimental (MS: mechanosynthesis) for parent compounds **1**, **2**, **3_{solv}**, **3A** and **3B**.

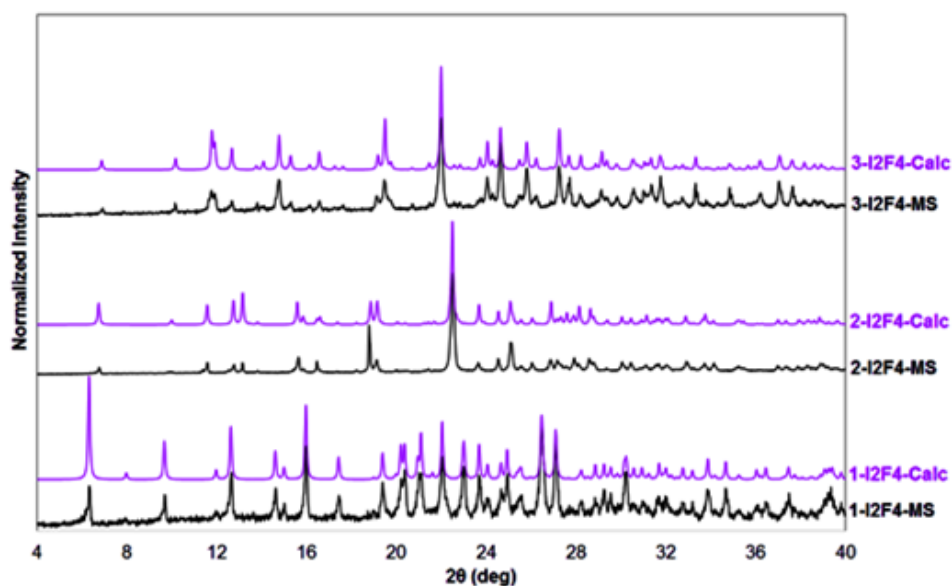


Figure B.4. XRPD comparison between calculated (calc) and experimental (MS: mechanosynthesis) for co-crystals compounds **1₂·I2F4**, **2₂·I2F4** and **3₂·I2F4**.

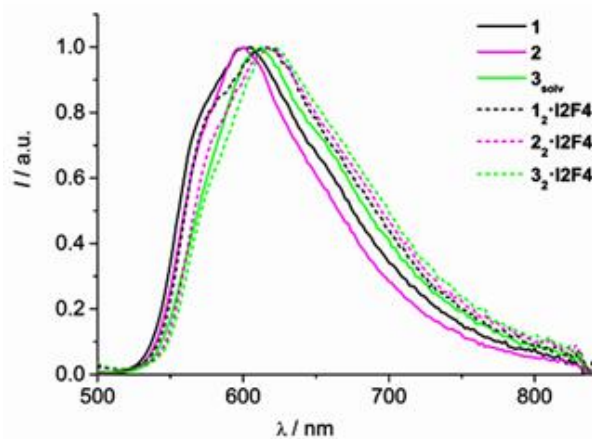


Figure B.1. Normalised room temperature emission spectra of single crystal samples of compounds **1**, **2**, **3_{solv}** and respective co-crystals. $\lambda_{\text{exc}} = 480$ nm.

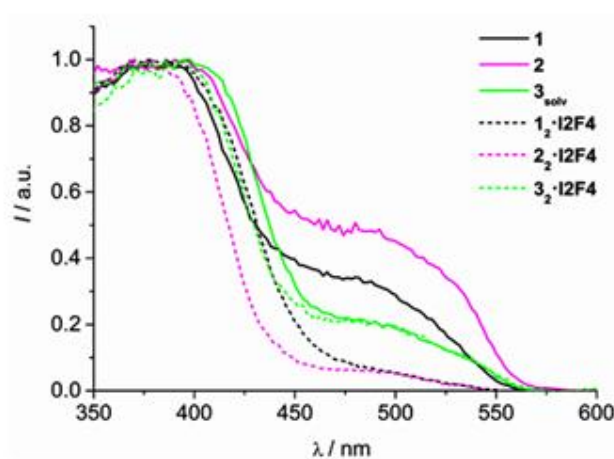


Figure B.6. Normalised room temperature excitation spectra of powder samples of compounds **1**, **2**, **3_{solv}** and respective co-crystals. $\lambda_{\text{em}} = 650$ nm.

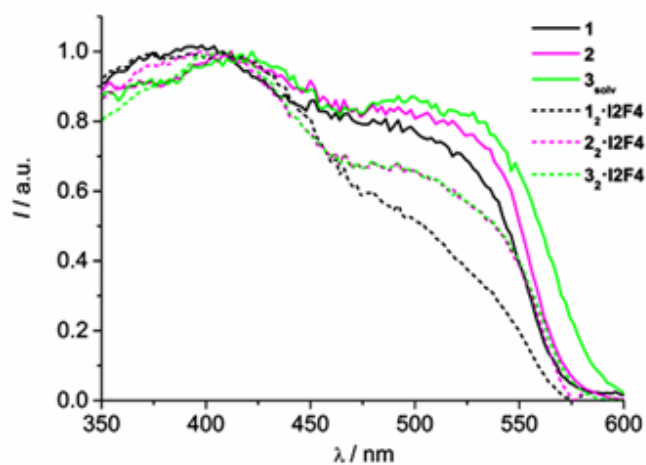


Figure B.2. Normalised room temperature excitation spectra of single crystal samples of compounds **1**, **2**, **3_{solv}** and respective co-crystals. $\lambda_{\text{em}} = 660$ nm.

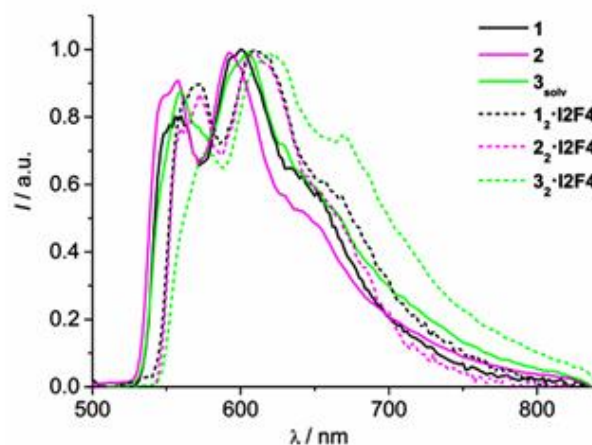


Figure B.3. Normalised emission spectra at 77 K of single crystal samples of compounds **1**, **2**, **3_{solv}** and respective co-crystals. $\lambda_{\text{exc}} = 450$ nm.

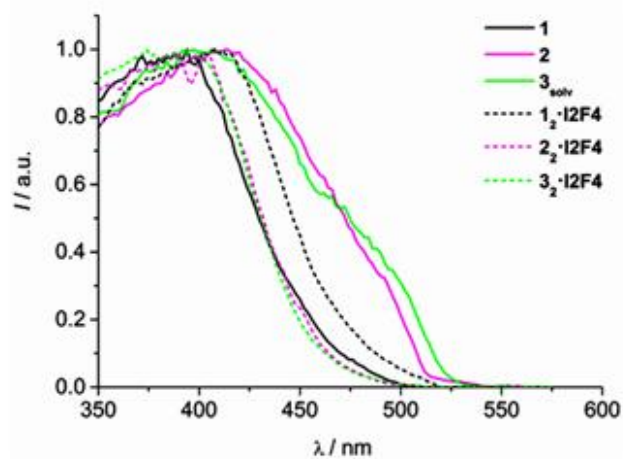


Figure B.4. Normalised excitation spectra at 77 K of powder samples of compounds **1**, **2**, **3_{solv}** and respective co-crystals. $\lambda_{\text{em}} = 600/620$ nm.

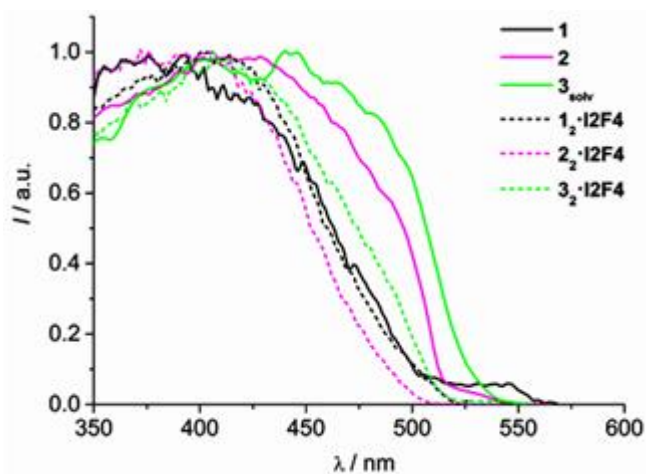


Figure B.5. Normalised excitation spectra at 77 K of single crystal samples of compounds **1**, **2**, **3_{solv}** and respective co-crystals. $\lambda_{\text{em}} = 600$ nm.

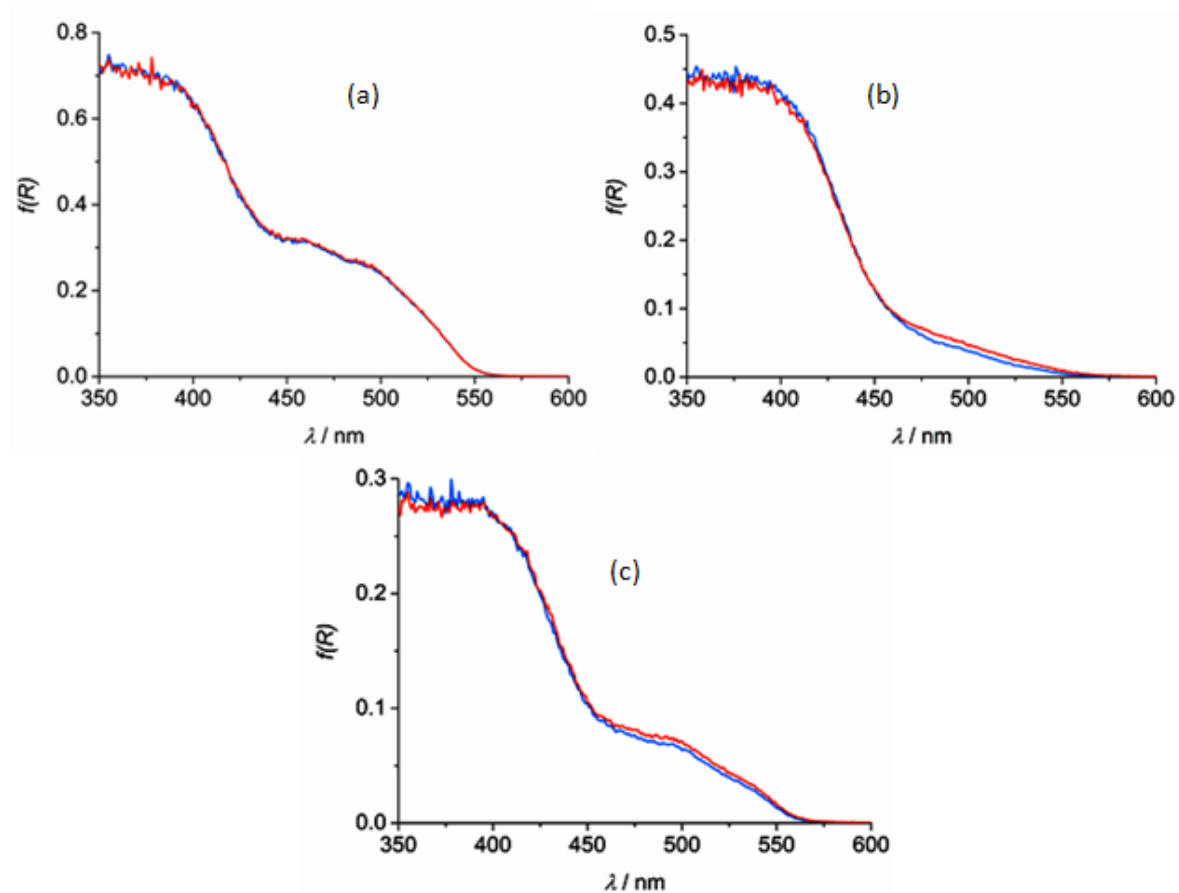


Figure B.11. Absorption spectra of powder samples of compounds **1** (a), **1₂·I₂F₄** (b), and **3_{solv}** (c) before (blue) and after (red) HP irradiation at $\lambda = 365$ nm for 20 min.

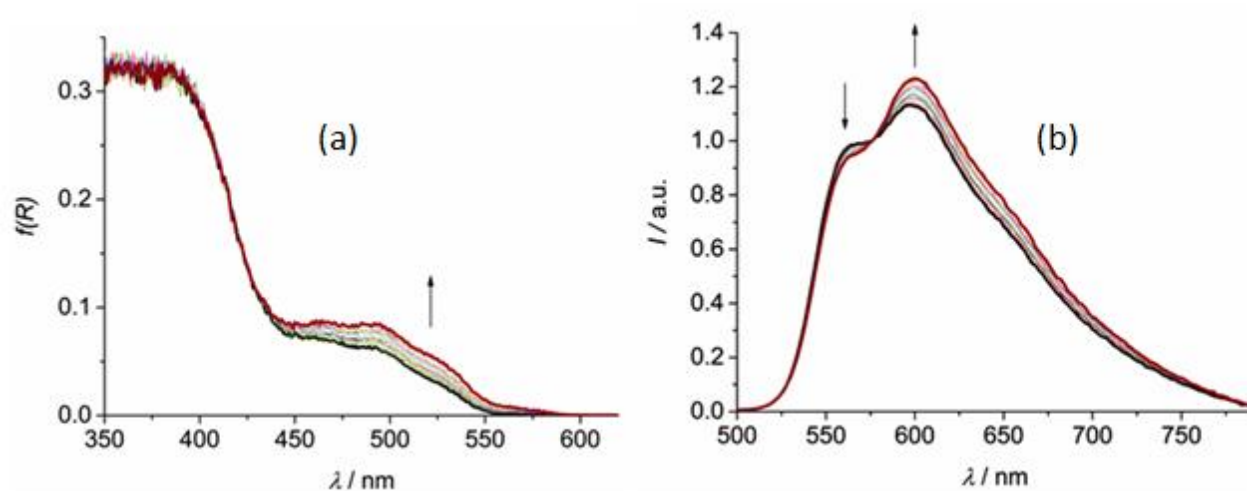


Figure B.12. Absorption (a) and emission (b) spectra of **2** before (black thick) and after (red thick) irradiation at $\lambda = 365$ nm for 40 min (20 min LP and 20 min HP). Thin lines represent spectra at intermediate times. In (b) the spectra are arbitrarily normalised at $\lambda = 576$ nm; $\lambda_{\text{exc}} = 400$ nm.

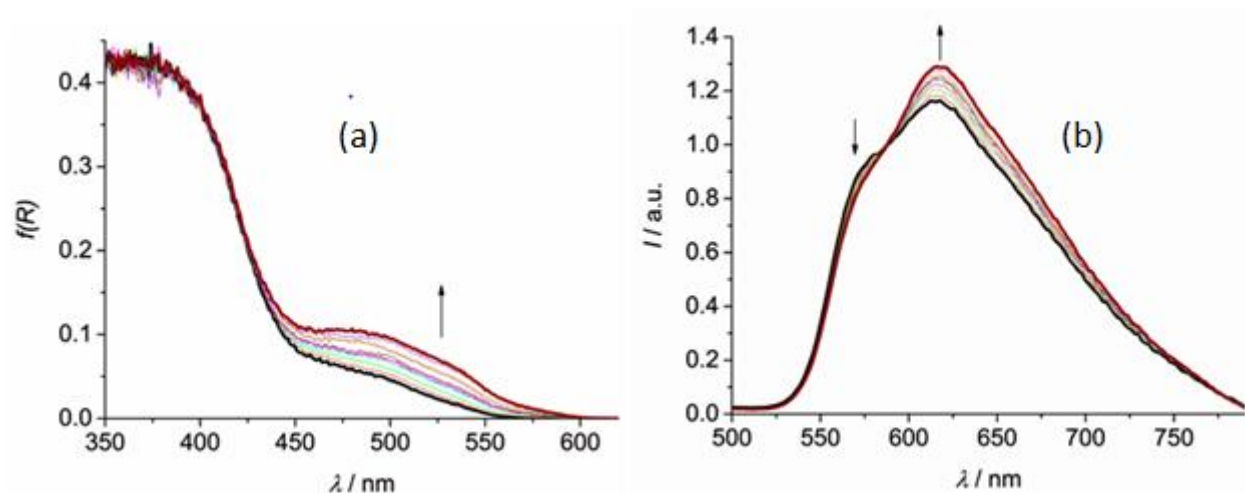


Figure B.13. Absorption (a) and emission (b) spectra of $2_2 \cdot \text{I2F4}$ before (black thick) and after (red thick) irradiation at $\lambda = 365$ nm for 40 min (20 min LP and 20 min HP). Thin lines represent spectra at intermediate times. In (b) the spectra are arbitrarily normalised at $\lambda = 588$ nm; $\lambda_{\text{exc}} = 400$ nm.

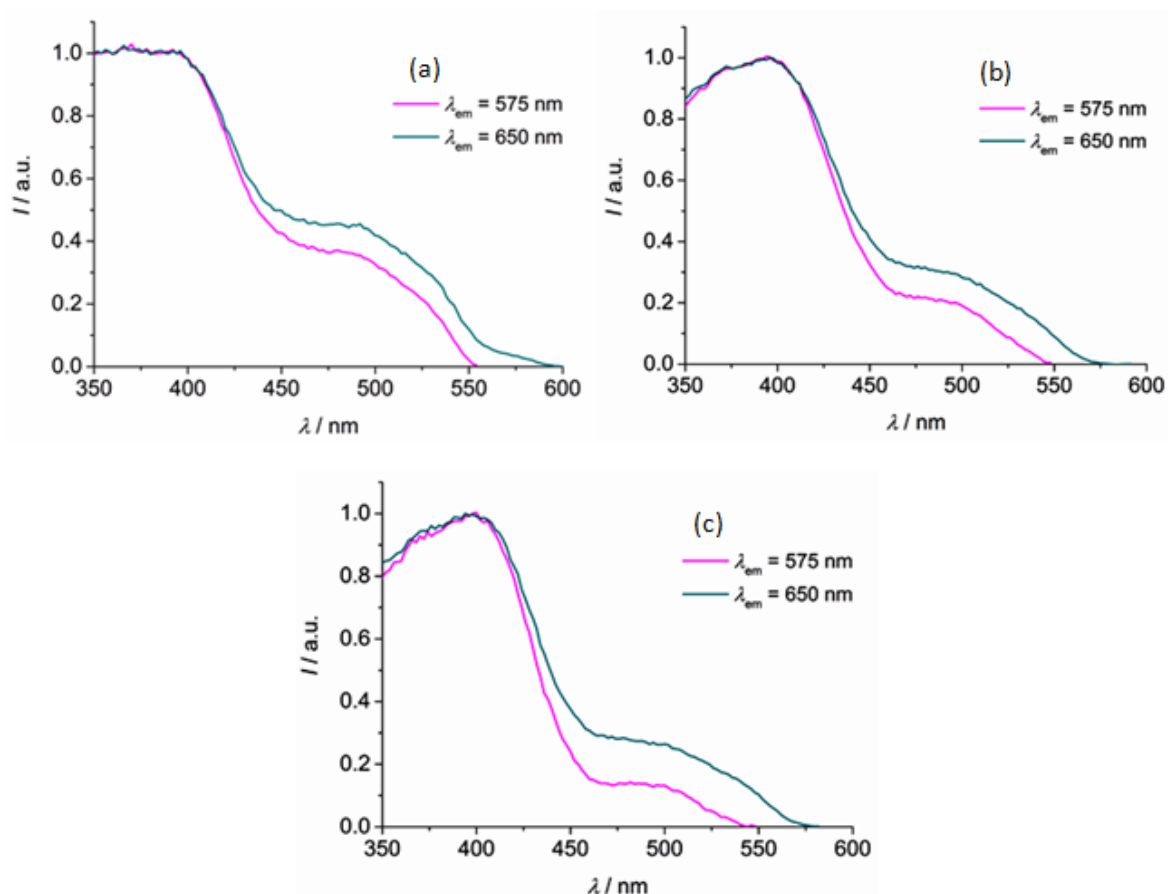


Figure B.14. Normalised excitation spectra of powder samples of **2** (a), $2_2 \cdot \text{I2F4}$ (b) and $3_2 \cdot \text{I2F4}$ (c) collected at $\lambda = 575$ nm and $\lambda = 650$ nm in the photostationary state.

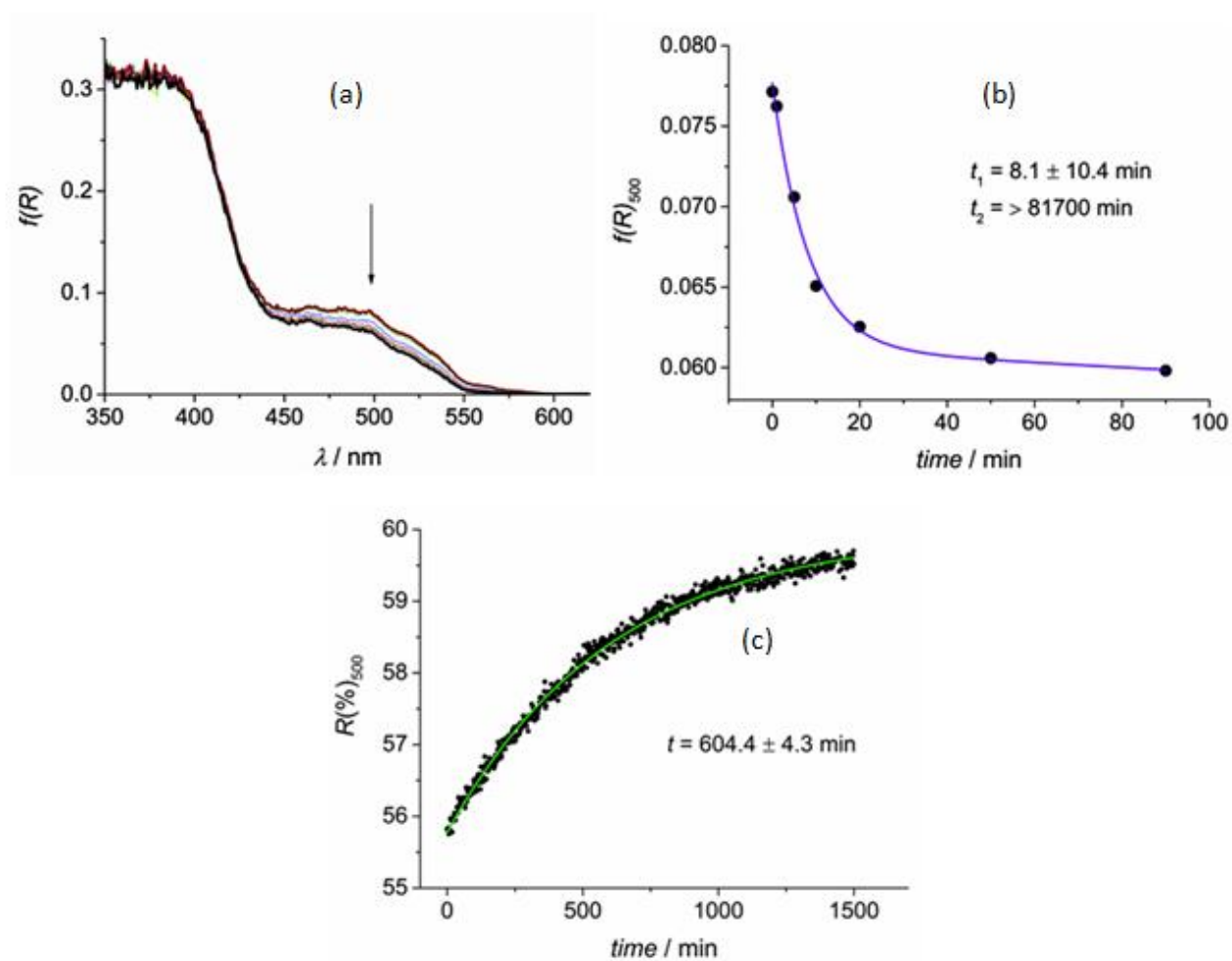


Figure B.15. (a) Absorption spectral changes of **2** starting from the photostationary state and following irradiation at $\lambda = 465 \text{ nm}$ for 90 min. (b) Data points at $\lambda = 500 \text{ nm}$ from graph (a) and bi-exponential fitting (blue). (c) Variation of the reflectance of **2** at $\lambda = 500 \text{ nm}$ as a function of time, starting from the photostationary state and following the thermal back reaction; in green the mono-exponential fitting.

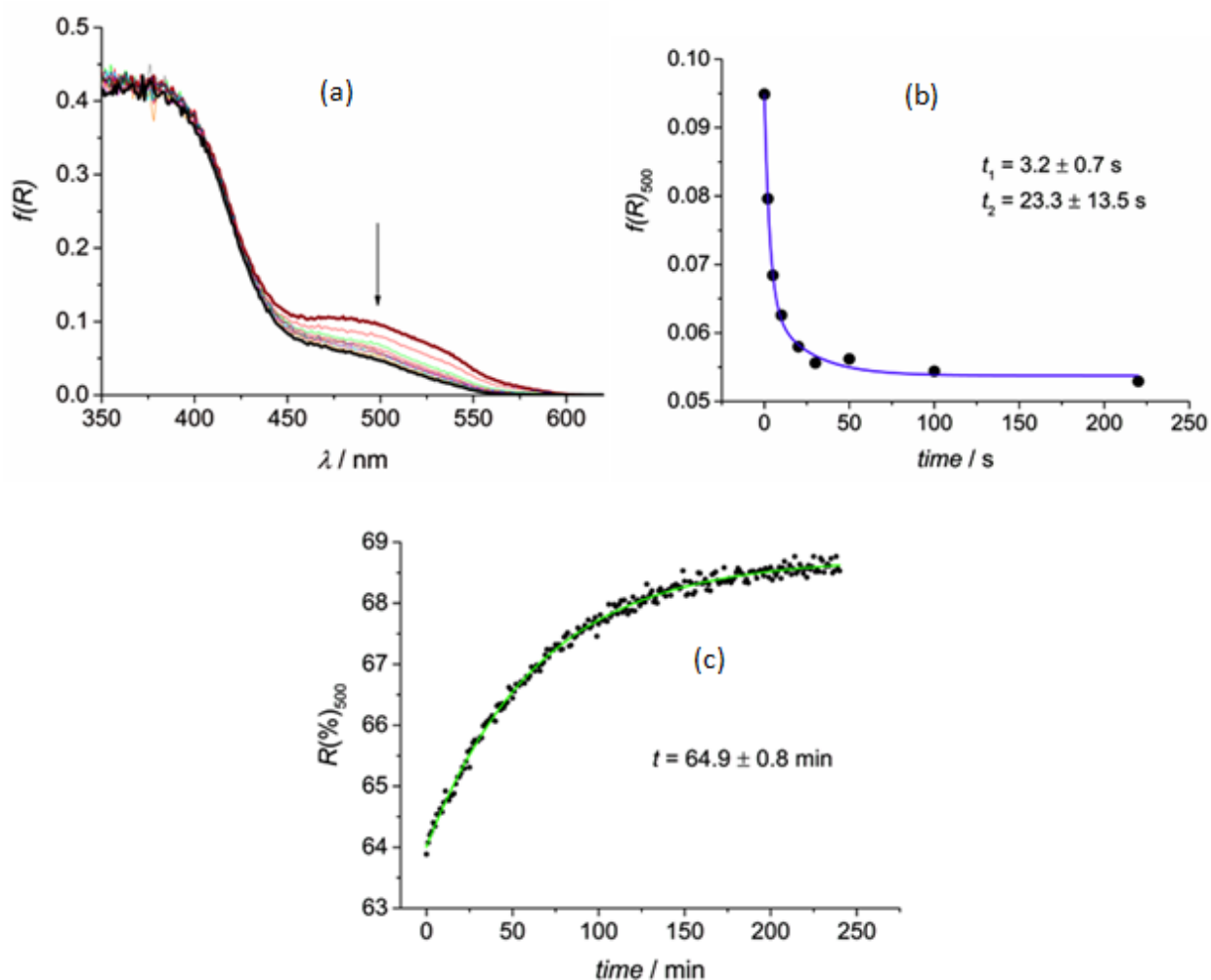


Figure B.16. (a) Absorption spectral changes of $2_2 \cdot \text{I2F4}$ starting from the photostationary state and following irradiation at $\lambda = 465$ nm for 220 s. (b) Data points at $\lambda = 500$ nm from graph (a) and bi-exponential fitting (blue). (c) Variation of the reflectance of $2_2 \cdot \text{I2F4}$ at $\lambda = 500$ nm as a function of time, starting from the photostationary state and following the thermal back reaction; in gree the mono-exponential fitting.

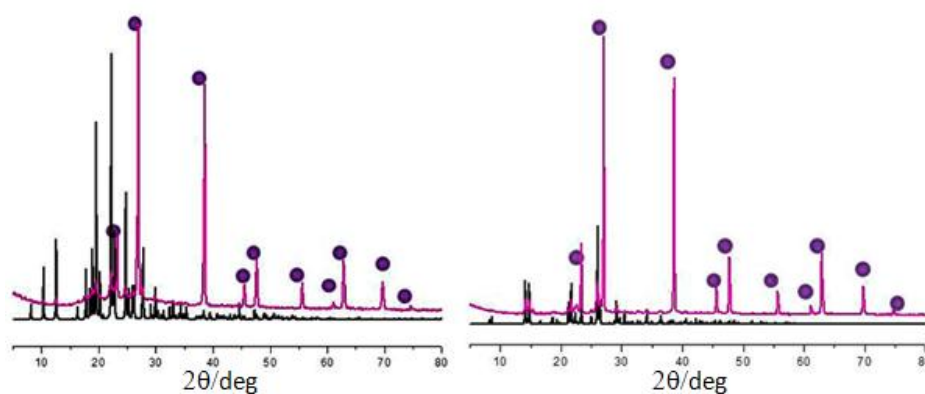


Figure B.17. Powder X-ray diffraction patterns recorded on crushed KBr pellets containing samples of **1** (a) and **2** (b). Experimental (purple line) and simulated (black line) X-ray powder diffraction patterns. Purple circles indicate the KBr phase.

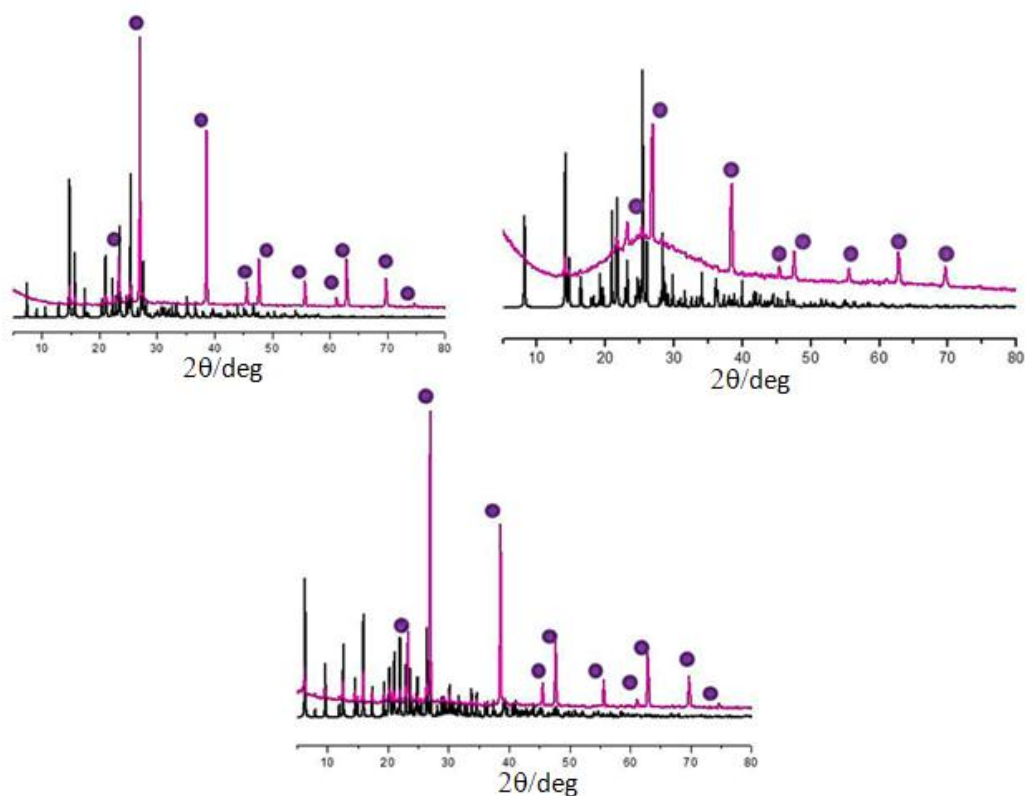


Figure B.18. Powder X-ray diffraction patterns recorded on crushed KBr pellets containing samples of **3A** (a), **3** (b) and $1_2 \cdot I_2F_4$ (c). Experimental (purple line) and simulated (black line) X-ray powder diffraction patterns. Purple circles indicate the KBr phase.

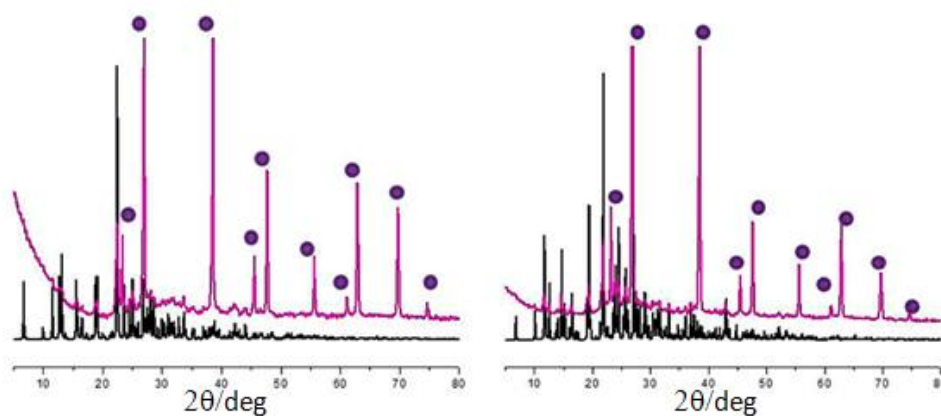


Figure B.19. Powder X-ray diffraction patterns recorded on crushed KBr pellets containing samples of $2_2 \cdot I_2F_4$ (a) and $3_2 \cdot I_2F_4$ (b). Experimental (purple line) and simulated (black line) X-ray powder diffraction patterns. Purple circles indicate the KBr phase.

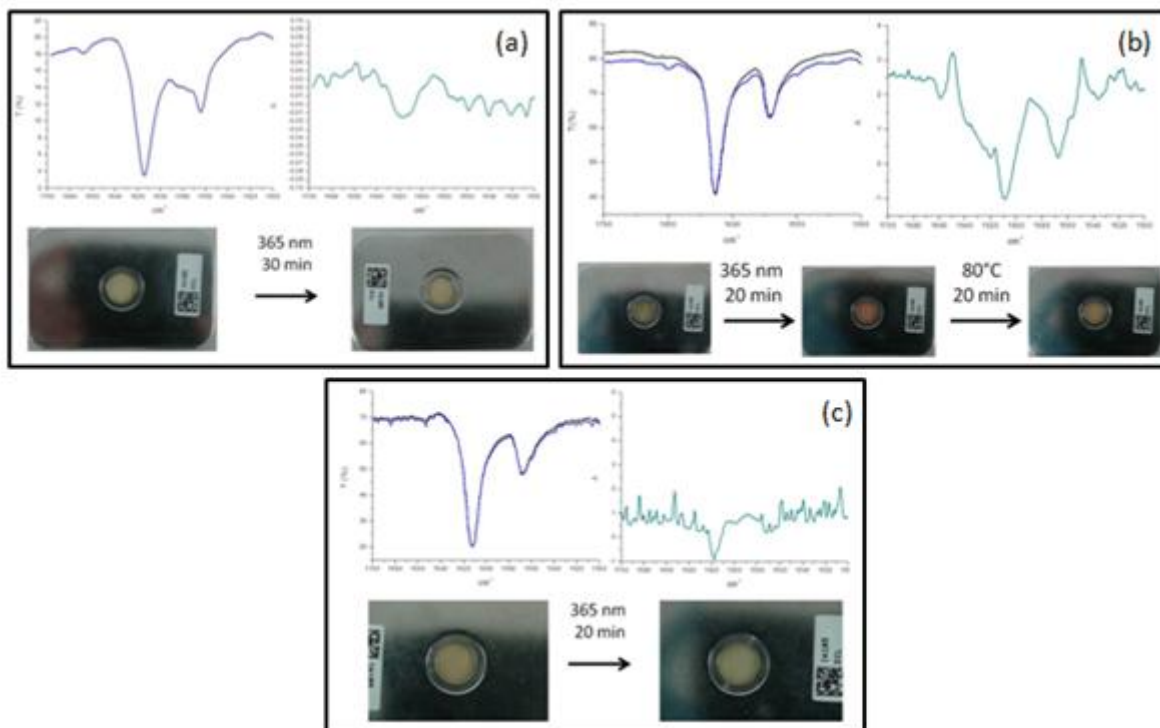


Figure B.20. FTIR spectra and pictures for compounds **1** (a), **2** (b) and **3a** (c) dispersed in KBr pellets.

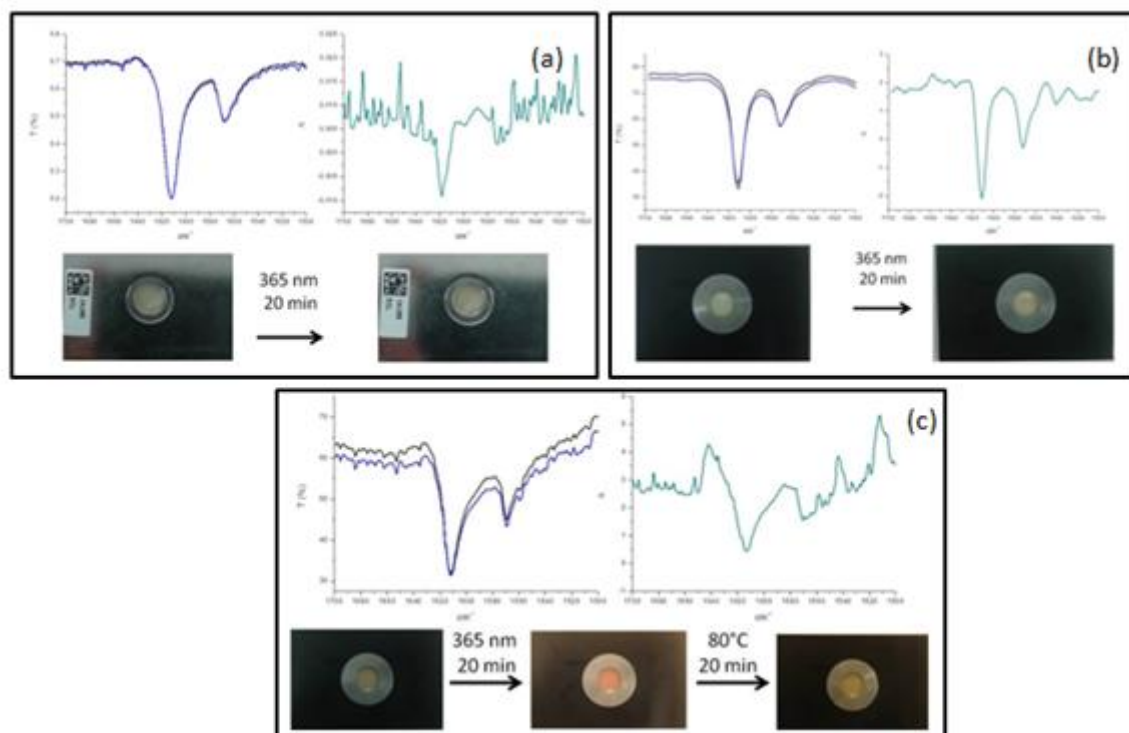


Figure B.21. FTIR spectra and pictures for compounds **3b** (a), and co-crystals **1·I₂F₄** (b) and **3·I₂F₄** (c) dispersed in KBr pellets.

Table B.5. Solid-state NMR acquisition parameters for samples **1**, **2** and **3_{solv}** and their co-crystals.

sample	¹³ C		¹⁵ N		Relaxation delay (s)
	Resolution (Hz)	scans	Resolution (Hz)	scans	
1	30	274	30	8000	11.4
1₂·I2F4	30	1700	30	11000	14.8
2	30	2500	26	10500	6.0
2₂·I2F4	30	1000	26	34000	7.3
3	30	1600	31	27500	9.1
3₂·I2F4	30	8000	26	14000	5.8

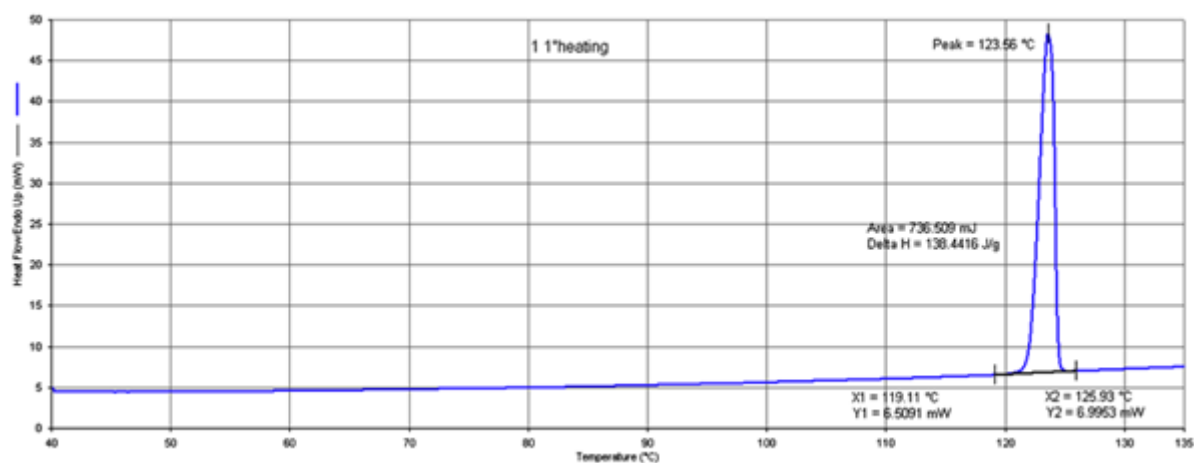
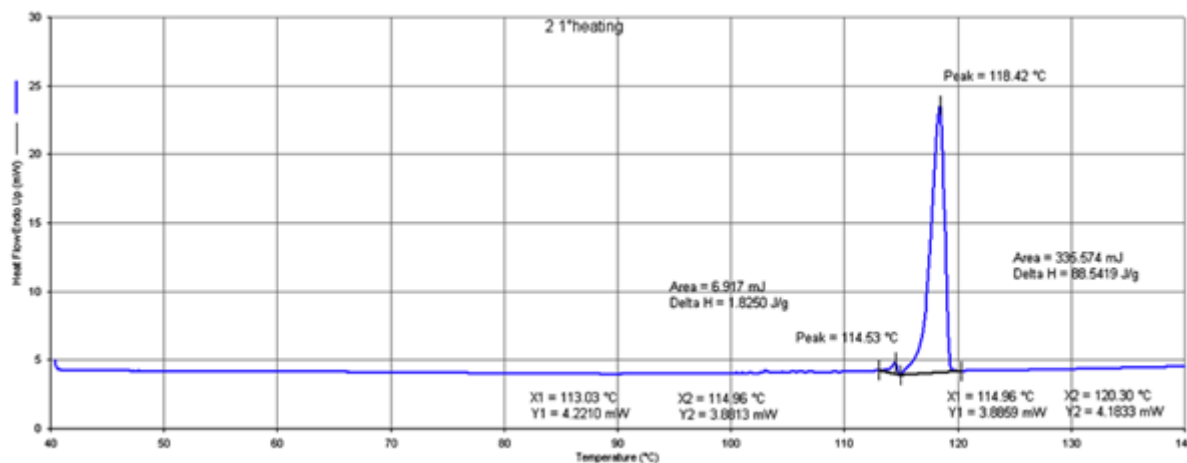
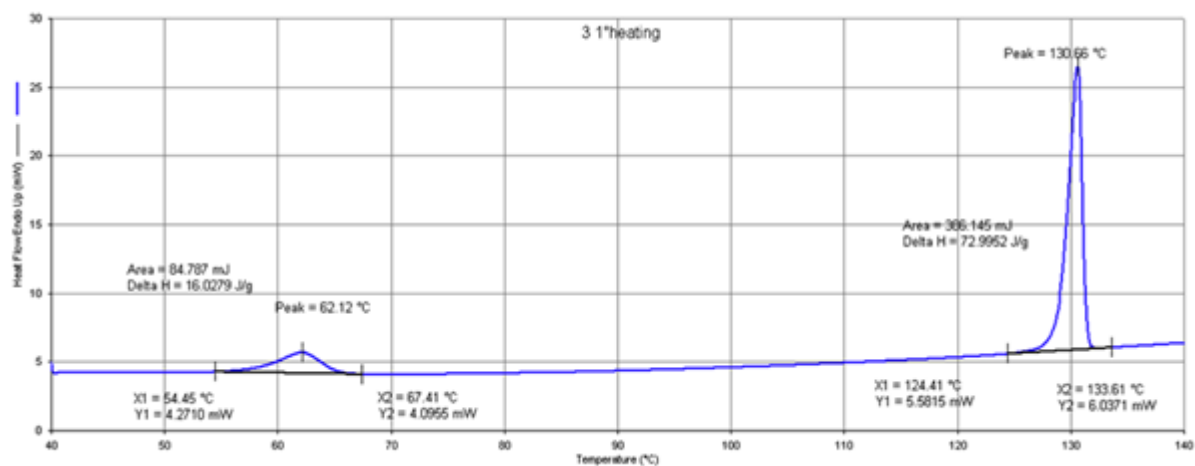
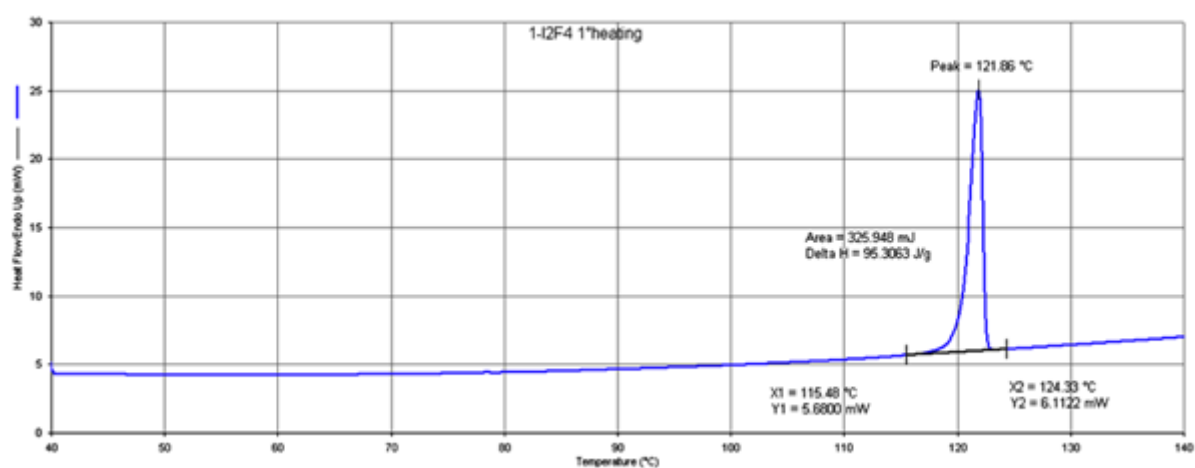
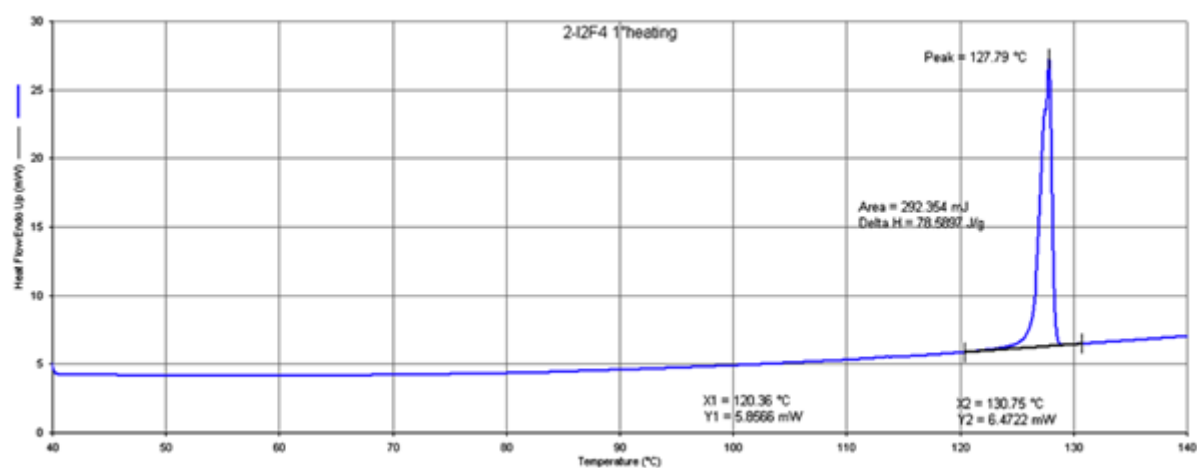
**Figure B.22.** DSC trace of the compound **1**.

Figure B.23. DSC trace of the compound **2**.Figure B.24. DSC trace of the compound **3_{solv}**.Figure B.25. DSC trace of the compound **1₂·12F4**.Figure B.26. DSC trace of the compound **2₂·12F4**.

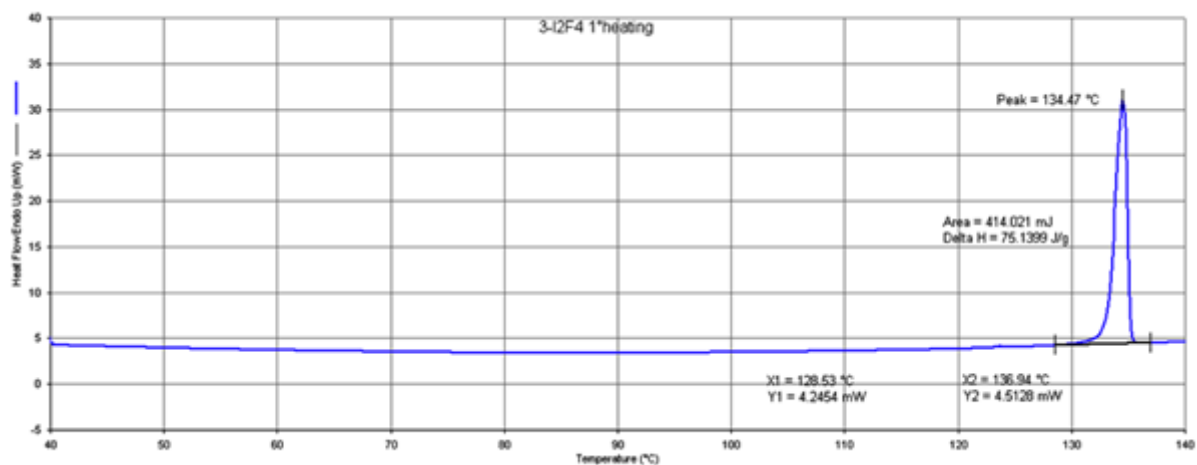


Figure B.27. DSC trace of the compound $3_2 \cdot I_2F_4$.

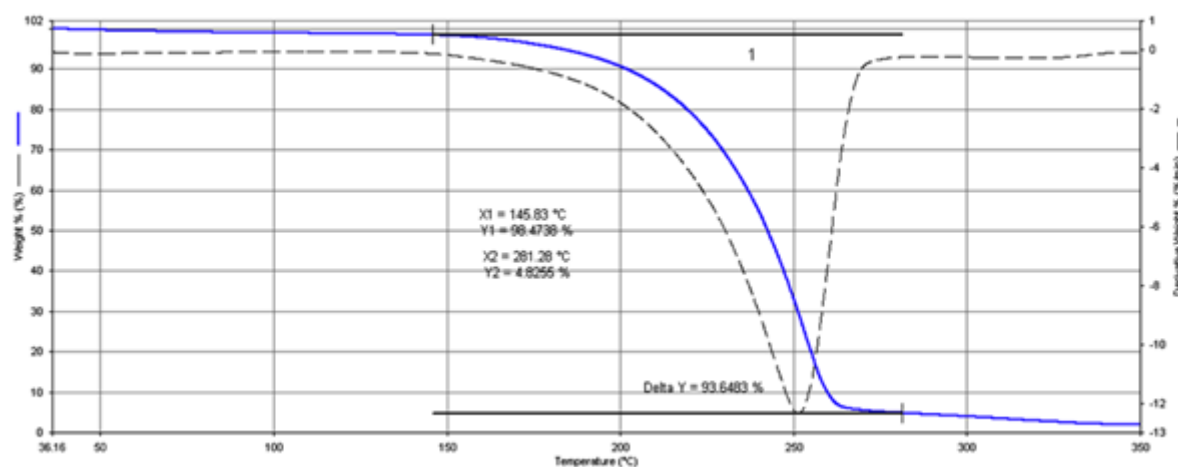


Figure B.2. TGA trace of the compound **1**.

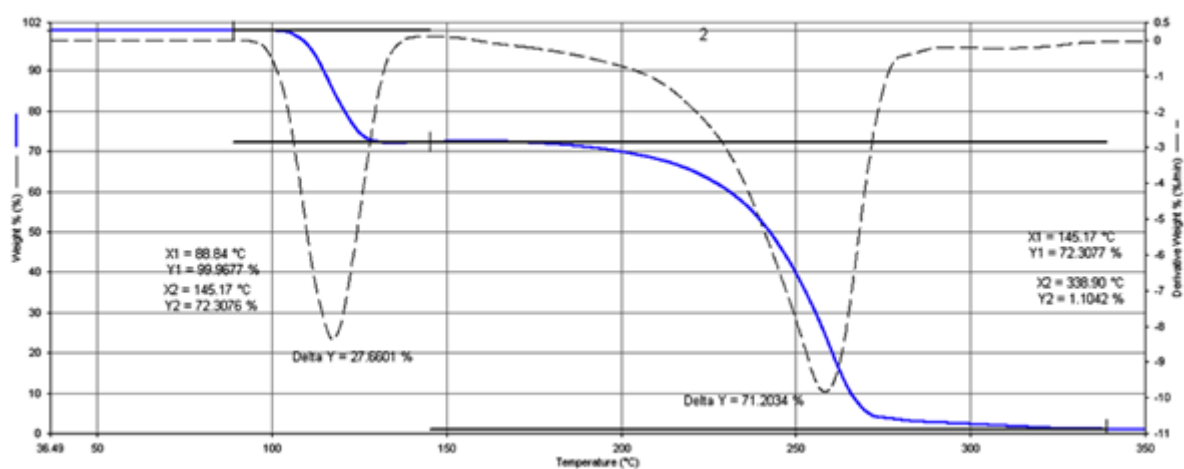


Figure B.29. TGA trace of the compound **2**.

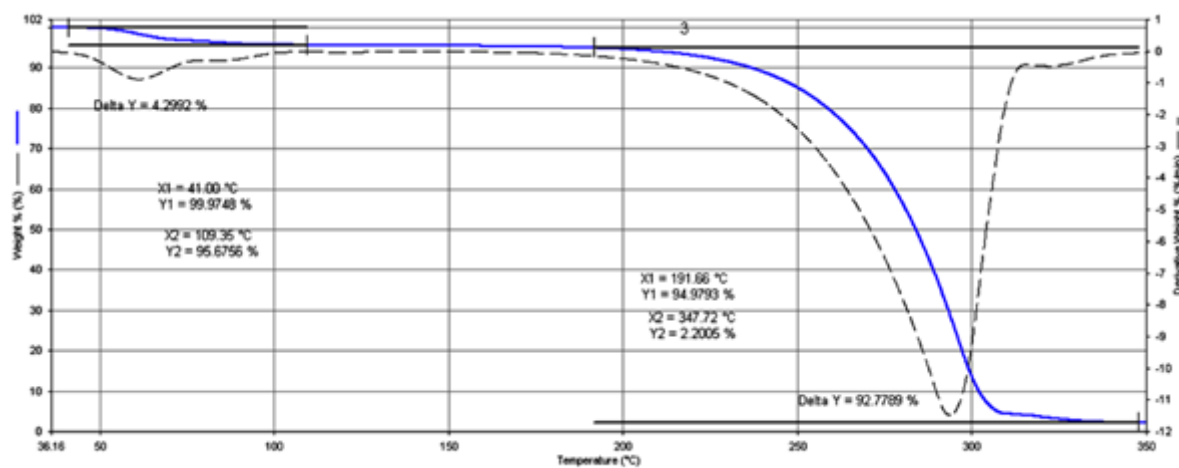


Figure B.30. TGA trace of the compound 3_{solv} .

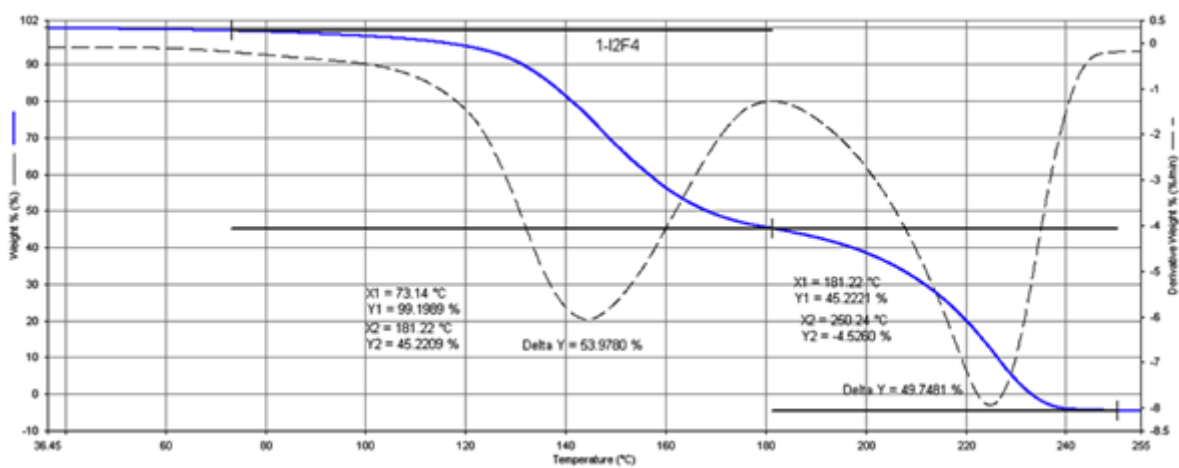


Figure B.31. TGA trace of the compound $1_2 \cdot \text{I2F4}$.

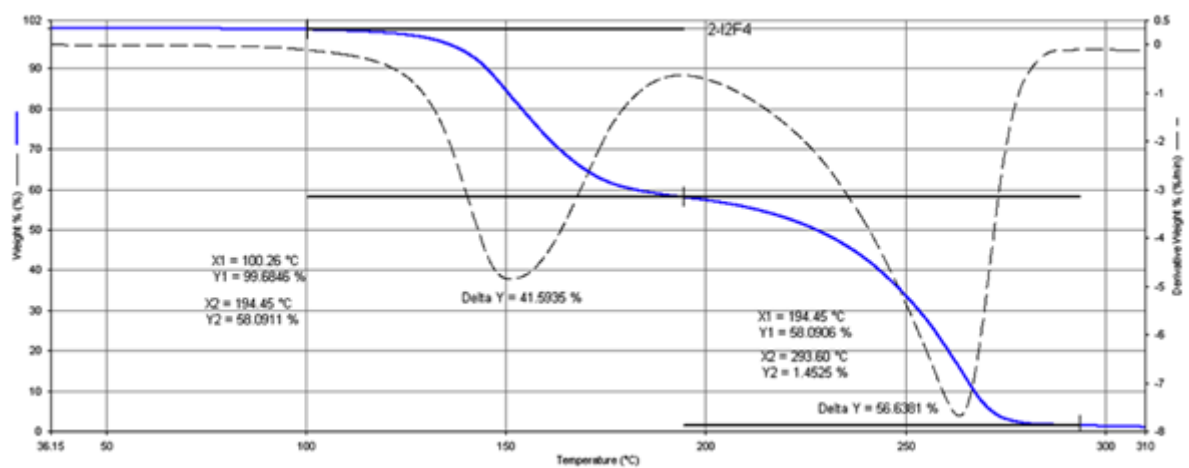
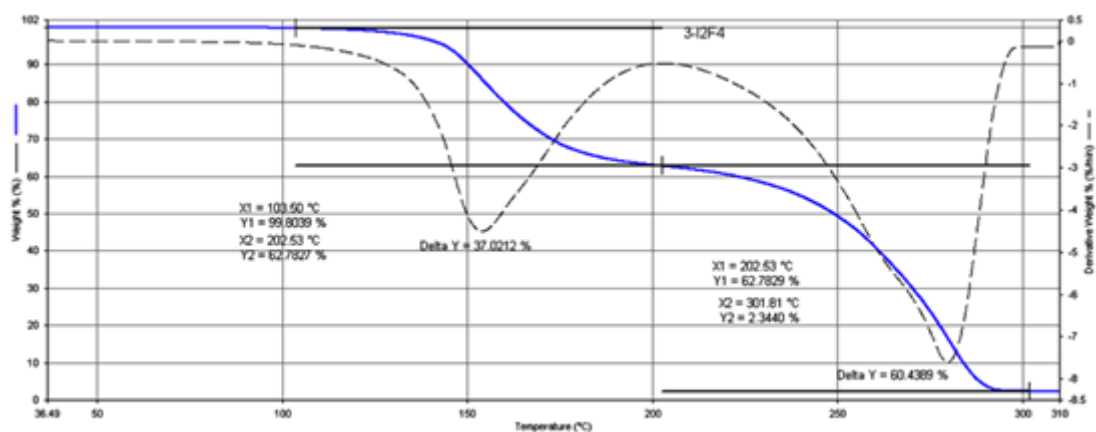
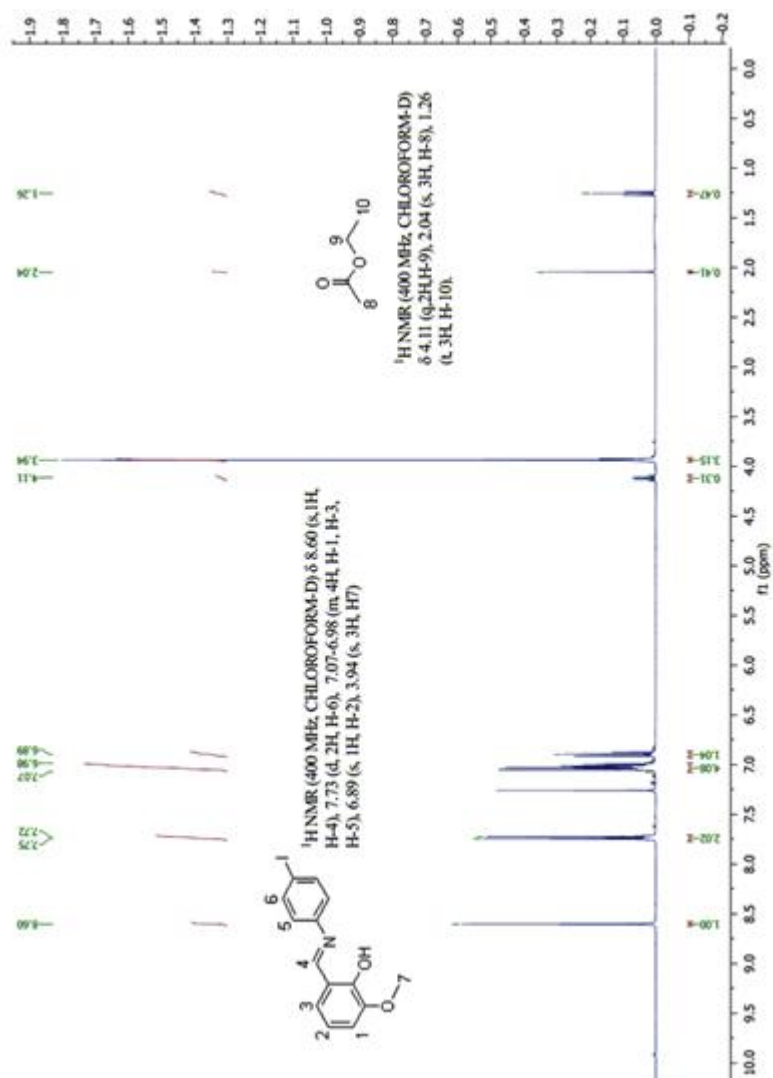


Figure B.32. TGA trace of the compound $2_2 \cdot \text{I2F4}$.

Figure B.33. TGA trace of the compound $3 \cdot I2F4$.Figure B.34. ¹H NMR spectrum of 3_{solv} .